NORTHWESTERN UNIVERSITY

Plasmon-Enhanced Light-Matter Interaction in Hybrid Nanostructures

A DISSERTATION

SUBMITTED TO THE GRADUATE SCHOOL
IN PARTIAL FULFILLMENT OF THE REQUIREMENTS

for the degree

DOCTOR OF PHILOSOPHY

Field of Chemistry

By
Yue Wu

EVANSTON, ILLINOIS

December 2021

Abstract

Plasmon-Enhanced Light-Matter Interaction in Hybrid Nanostructures

Yue Wu

Plasmonic nanoparticles have very large absorption cross sections and can concentrate the local density of photon states on the nano scale. When they are coupled to molecules or semiconductor nanocrystals and form different hybrid nanostructures, various light-matter interaction processes can be significantly enhanced or manipulated, including optical responses like fluorescence and Raman scattering, photochemical reactions, energy transfer processes, etc. In this dissertation, several different plasmonic hybrid nanostructures were studied to explore in detail the plasmonic effect in various light-matter interaction processes, which can lead to potential novel applications in spectroscopy, photochemistry, and quantum optics.

Chapter 1 provides an introduction and theory background to the projects in this thesis. In Chapter 2 we studied a plasmon-driven electron transfer reaction between gold nanoparticles and electron acceptor molecules, monitored by surface-enhanced Raman spectroscopy (SERS). We demonstrate that the hot electrons generated by plasmon decay from both the interband and intraband transitions in gold nanoparticles can trigger the electron transfer reaction through an indirect electron transfer mechanism. Chapter 3 describes a local-environment-engineering strategy of coating semiconductor nanocrystals with a plasmonic nanoshell structure to suppress spectral diffusion at the single particle level. The main mechanism is the Purcell enhancement of radiative decay rate of the semiconductor nanocrystals. In Chapter 4, a strongly coupled hybrid

system composed of silver nanoprisms and a dye J-aggregates is constructed. The surface-enhanced Raman excitation spectroscopy not only reveals the plasmonic/molecular characteristics of the two hybrid polariton states, but also indicates the existence of a large manifold of dark states in the strong coupling regime.

Acknowledgements

When I look back to my five-year PhD study, lots of unforgettable moments flashed back in my memory. I feel very lucky that I have interacted with so many talented and enthusiastic people, and I am really thankful for all the help and support during my graduate school.

First, I would like to thank all my three advisors: Professor Emily Weiss, Professor George Schatz, and Professor Richard Van Duyne. Rick, thank you for leading me into the research field of optical spectroscopy although I have very little related research experience when I just came to Northwestern. You were always an inspiring advisor, encouraging us to try different new ideas in the laser lab with your full support. I also feel so grateful for your effort to build up such lively group environment: beer hour every Friday afternoon, March Madness Bracket, group gatherings, small chats with you in the office or lab, etc., which made me thrilled to enjoy the lab work every day. I will always miss you and thank you for all the things you have done for us. George, I really admire your broad knowledge and precise intuition in chemistry and physics. Every time I talk to you about the problems I met in my theory or experiment research, you can always give me not only useful advice to solve current problems but also deeper insights for possible new research ideas. Emily, thank you for bringing me to your group at the end of my third year in graduate school. From you I learned a lot about efficient management of research projects, the leadership in collaboration work, logic writing skills to present my research. I am really impressed by your enthusiasm in science and the open mind to new research directions. To me, you are not only an excellent advisor giving me all the guidance I need in time, but also a perfect model for me to follow as a scientist.

Next, I want to thank my committee: Professor Tamar Seideman and Professor Lin Chen. They both have given me useful advice not just on specific research projects, but more on approaches of doing research in general. I also want to thank Professor Teri Odom and Dr. Toru Shiozaki who served on my qualification exam committee, helping me to adjust my ways of doing research in the early stage of my PhD study.

Now it's time to for all the colleagues I have worked with in all the three groups. I'd like to thank my mentors in Van Duyne lab, Dr. Mike McAnally, and Dr. Tyler Ueltschi. They both taught me lots of knowledge about all the aspects of optical spectroscopy, from the theoretical description to the experimental details. I want to thank Dr. Muwen Yang from Van Duyne group (also my undergraduate classmate) for all the discussion on our projects and the help in the lab. I also have to thank Dr. Shawn Zhao in Weiss lab. It wouldn't be that fun to search for single particles and single photon emission if I didn't work with you together in the dark microscope room. Special thanks to Dr. Mike Mattei and Professor Yinsheng Guo for the fun Euchre game on Friday beer hours. Thank Dr. Nolan Wong for all the delicious food and your consolation when I was frustrated. Lots of thanks to Professor Kevin Kohlstedt for helping me to solve all kind of issues I met when using various quantum chemistry codes. I also want to thank Dr. Rafael Lopez for all the help with the optics and lasers in the microscope room. I realize it could be an endless list if I go through every group member, but I do want to thank every one of you, not only the discussion or help in the research work, but also all the chats, warm words, and useful suggestions in the daily life, which really enlighten my PhD journey in these five years.

Outside the lab, I would like to thank my friends I met at Northwestern: Dr. Yuanning Feng, Wenjie Zhou, Haochuan Mao, Dr. Su Chen, Xiaoyu Cheng, Ruiheng Wu, etc. I will always remember the weekend nights we spent together, drinking, playing card games, and most importantly, chatting about our wildest dreams and any interesting things happening all over the world.

Finally, I want to say thank you to my family. Mom and Dad, thank you for supporting my dream of pursuing PhD in the United States. No matter how hard the situation I meet, you always open your arms to me and provide me the most solid support. I could not have achieved anything without you.

There is an old Chinese proverb: “There is no permanent banquet in the world”. To me, although my PhD study does come to an end, I will always treasure every person I met and every moment I experience during this journey. Again, thank you all for your help during my PhD and making me a better person.

List of Abbreviations

ALD	Atomic layer deposition
APD	Avalanche photodiode
APTMS	(3-Aminopropyl) trimethyloxysilane
AuNP	gold nanoparticles
BEM	Boundary element method
CCD	Charge coupled device
CdS	Cadmium sulfide
CdSe	Cadmium selenide
CI	Configuration Interaction
CT	Charge transfer
CV	Cyclic voltammetry
CW	Continuous wave
DFT	Density functional theory
DMF	Dimethylformamide
EBL	Electron-beam lithography
EC	Electrochemical
EF	Enhancement factor
EM	Electromagnetic
ES	Excited state
eV	electron volt
GGA	Generalized gradient approximation

HOMO	Highest occupied molecular orbital
JC	Jaynes-Cumming
LSPR	Localized surface plasmon resonance
LUMO	Lowest unoccupied molecular orbital
MC	Merocyanine
nm	nanometer
NPOM	nanoparticle-on-mirror
PCBM	[6,6]-phenyl-C_{61}-butyric acid methyl ester
PC-RET	Plasmon-coupled resonance energy transfer
PL	Photoluminescence
PLE	Photoluminescence excitation
ps	picosecond
PVP	Polyvinylpyrrolidone
QD	Quantum dot
QY	Quantum yield
SD	Spectral diffusion
SERS	Surface-enhanced Raman scattering
SiO_2	Silicon dioxide
SNR	Signal-to-noise ratio
SPI	Spiropyran
TC	Tavis-Cumming
TCSPC	time-correlated single photon counting
TDBC	(5, 5’,6,6’-tetrachloro-di-(4-sulfobutyl) benzimidazolocarbocyanine)
TDPA	Tetradecylphosphonic acid

TEOS	Tetraethyl orthosilicate
TLS	Two-level system
TMDC	Transition metal dichalcogenides
TRPL	Time-resolved photoluminescence
UV	Ultraviolet
WS-SERES	wavelength-scanned surface-enhanced Raman excitation spectroscopy

Table of Contents

Abstract ... 3

Acknowledgements ... 5

List of Abbreviations ... 8

Table of Contents ... 11

List of Figures ... 14

List of Tables ... 18

List of Schemes ... 19

Chapter 1: Introduction ... 20

1.1 Chapter Summary ... 21

1.2 Basic Description of Surface Plasmon ... 21

1.3 Plasmonic Enhancement in Raman Scattering Process ... 22

1.4 Plasmon-Exciton Coupling ... 24

1.4.1 Jaynes-Cumming Model ... 26

1.4.2 Weak Coupling Regime ... 29

1.4.3 Strong Coupling Regime ... 35

1.5 plasmon-Driven Hot Carrier Photochemistry ... 38

1.5.1 Plasmon Decay Process ... 38

1.5.2 Proposed Mechanisms of Plasmon-Driven Chemical Reactions ... 39

1.5.3 Examples of Plasmon-Driven Chemical Reactions ... 41

1.6 Thesis Overview ... 42

Chapter 2: SERS study of plasmon-driven hot electron transfer between gold nanoparticles and PCBM ... 44

2.1 Chapter Summary ... 45

2.2 Introduction ... 45

2.3 Results and Discussion ... 47

2.3.1 Preparation of AuNP-PCBM Composite and the Extinction Spectra ... 47

2.3.2 CW Two-color SERS Experiments on AuNP-PCBM Composite ... 48

2.3.3 Electronic Structure of PCBM Adsorbed on Au Surface ... 51

2.3.4 Confirming the Correlation between PCBM 1458 cm^{-1} Raman Peak Shift and Electron Transfer Events using DFT and EC-SERS ... 52

2.3.5 Excitation Wavelength Dependence of the Electron Transfer Process 54
2.3.6 Stokes and Anti-Stokes SERS for Nanoscale Thermometry 57
2.4 Experimental Methods 59
2.4.1 AuNP/PCBM Composite Preparation 59
2.4.2 CW Pump Probe SERS Experiments 59
2.4.3 EC-SERS Experiments 60
2.4.4 Theoretical Calculations 61
2.5 Chapter Conclusion 61
2.6 Supporting Information 63
2.6.1 Degradation of PCBM under High Pump Laser Power 63
2.6.2 The Derivation of the Kinetic Model for Pump Power Experiment 63
2.6.3 PCBM Full Cyclic Voltammetry (CV) 65
2.6.4 DFT Simulations of the PCBM-Au_{20} System 65
Chapter 3: Reduced Spectral Diffusion of Single Quantum Dot Emission with Plasmonic Nanoshell Structure 67
3.1 Chapter Summary 68
3.2 Introduction 68
3.3 Results and Discussion 70
3.3.1 Synthesis of QD/silica/gold core/spacer/shell Particles 70
3.3.2 UV-vis and PL Characterization 73
3.3.3 Single Particle Characterization on the Microscope 73
3.3.4 Reduced Blinking of QD/silica/Au Particles 75
3.3.5 The PL Spectra Time Traces for Monitoring Spectral Diffusion 76
3.3.6 Purcell Factor Estimated by Emission Lifetime Measurements 78
3.4 Experiment Methods 80
3.4.1 The Synthesis Procedure of QD/silica/Au Hybrid Nanoparticles 80
3.4.2 Homebuilt Confocal Microscope for Single Particle Measurements 82
3.4.3 Emission Lifetime Measurements 83
3.5 Chapter Conclusion 83
3.6 Supporting Information 84
3.6.1 Some Notes on the Colloidal Synthesis of QD/silica/Au particles. 84
3.6.2 Electrodynamics Simulation of Plasmonic Shell Structure 85
3.6.3 Pretreatment of Glass Coverslip to Achieve Better Particle Dispersion 87

Chapter 4: Probing the Hybrid States of a Plasmon-Molecule Strongly Coupled System with Raman Excitation Spectroscopy 89
  4.1 Chapter Summary 90
  4.2 Introduction 90
  4.3 Results and Discussion 93
    4.3.1 Colloidal Synthesis of Silver Nanoprisms 93
    4.3.2 TDBC J-aggregates 95
    4.3.3 Rabi Splitting of Silver Nanoprism/TDBC J-aggregates 96
    4.3.4 SERS Spectra of TDBC J-aggregates 98
    4.3.5 Raman Excitation Spectra of Silver Nanoprism/TDBC J-aggregates 99
  4.4 Experimental Methods 102
    4.4.1 Synthesis Procedure of Silver Nanoprisms 102
    4.4.2 Wavelength-Scanned Raman Excitation Spectroscopy 103
  4.5 Chapter Conclusion 103
  4.6 Supporting Information 104
    4.6.1 The Surface Coverage of TDBC J-aggregates on Silver Nanoprisms 104
    4.6.2 The Detailed Procedure to Generate Raman Excitation Profile 105
    4.6.3 Silver Nanoprism/TDBC J-aggregates Strong Coupling System on Single Particle Level 107
References 108
Appendix A: Blinking and Spectral Diffusion of single CdSe Nanoplatelets at Room Temperature 122
Appendix B: Electronic Structure Calculations of Various Metal-Molecule Complexes 137
Appendix C: Original Research Proposal 142

List of Figures

Figure 1.1. (**a**) The scheme showing the oscillation of free electrons in metal nanoparticles that generate localized surface plasmon and lead to enhanced local electromagnetic field. (**b**) Finite-difference time-domain (FDTD) calculation of local electric field enhancement of a bowtie structure. Adapted from Ref (4). Copyright 2009 Nature Publishing group. 22

Figure 2.1. The extinction spectra of gold nanoparticle colloid in water (red curve) and gold nanoparticle aggregates with PCBM in DMF. CW 532 nm and 785 nm lasers were used as pump and probe respectively in the experiments. 48

Figure 2.2. (**a**)(**b**) PCBM SER spectra as a function of time with 532 nm CW pump laser excitation (a) and 785 nm CW probe laser only (b). The acquisition time of each frame was 2 seconds. The power of the probe laser was 100 μW. (**c**) PCBM SER spectra under different pump laser power. The power of the probe laser was 100 μW. The orange dashed line is at 1458 cm^{-1} to guide the view. (**d**) Pump power dependence of the peak shift of the 1458 cm^{-1} pentagonal pinch mode. The data was fitted with Eq 2.2, shown as the black curve. 50

Figure 2.3. (**a**) Simulation model for the DFT band structure calculation for PCBM on an Au (111) surface. Color code: C, gray; O red; H, white; Au, yellow. (**b**) Calculated projected density of states of PCBM and gold. The Fermi level of the system is at -2.81 eV. The grey strips in the figure show the HOMO and LUMO position of PCBM. 52

Figure 2.4. (**a**) Cyclic voltammetry of 2 mmol/L PCBM in *o*-dichlorobenzene/acetonitrile (5:1 by volume) with 0.1 mol/L $TBAPF_6$ at 100 mV/s under N_2 environment. 5 mmol/L Ferrocene (Fc) was added as an internal standard, shown as * in the CV. (**b**) Zoomed-in SER spectra of PCBM around the pentagonal pinch mode under different potentials. * is the normal Raman peak of *o*-dichlorobenzene. The black dashed line is at 1458 cm^{-1} to guide the eye. (**c**) Relationship between the frequency shift of the PCBM pentagonal pinch mode and the applied potential. 54

Figure 2.5. (**a**) Pump wavelength dependence of the plasmon-driven electron transfer process. The gray curve is the extinction spectrum of gold nanoparticle colloid with PCBM. The pump and probe laser power were kept at 200 μW and 300 μW, respectively. Simplified energy diagrams for

hot electron transfer with pump photon energy (**b**) below and (**c**) above the interband transition threshold. 57

Figure 2.6. (**a**) Stokes and anti-stokes side of PCBM SER spectrum with 750 μW 785 nm laser on the sample. The anti-stokes side is enlarged 40 times for a clearer view. (**b**) The effective vibrational temperature of the pentagonal pinch mode under different pump laser power (up to 300 μW) and wavelength. The power of 785 nm probe laser was kept at 750 μW. 58

Figure 2.7. CW pump-probe SERS setup. In excitation wavelength dependence experiments, the pump laser is switched to a tunable laser system. 60

Figure 2.8. Photodegraded PCBM SER spectrum under 450 μW 532 nm pump laser. 63

Figure 2.9. Full cyclic voltammetry of 2 mmol/L PCBM in *o*-dichlorobenzene/acetonitrile (5:1 by volume) with 0.1mol/L $TBAPF_6$ at 100 mV/s. 65

Figure 2.10. DFT calculation of PCBM with Au_{20} cluster. The HOMO-LUMO transition shows clear charge-transfer character. 66

Figure 3.1. The detailed synthesis scheme of QD/silica/Au core/spacer/shell nanoparticles and the TEM images of each step: (**a**) CdSe/3CdS QDs; (**b**) QD/silica; (**c**) QD/silica/Au_{seed}; (**d**) QD/silica/Au. 71

Figure 3.2. The TEM images of QD/silica particles with different added TEOS volume at the beginning of the silica shell growth: (**a**) 60 μL; (**b**) 300 μL. The averaged particle sizes are 28 nm (**a**) and 42 nm (**b**), respectively. 72

Figure 3.3. The solution-phase absorption (**a**) and PL (**b**) spectra of QD (black curves) and QD/silica/Au (red curves). 73

Figure 3.4. The single particle measurements of CdSe/3CdS QDs under room temperature. (**a**) The PL scan image of QDs in a 15*15 μm^2 region. (**b**) A finer PL scan of the red box region in (**a**). (**c**) The PL intensity time trace of single QD. (**d**) The second-order correlation function $g^{(2)}$ measurement of the same QD in (**c**). The laser power is 150 nW. 74

Figure 3.5. The Blinking behavior comparison between single QD (top trace, black) and single QD/silica/Au (bottom trace, red). The bin time for each trace is 10 ms. 75

Figure 3.6. The PL spectra time traces of single QD (**a**) and QD/silica/Au particle (**b**). The acquisition time for each frame is 2 s and the laser power is 150 nW. 76

Figure 3.7. PL peaks shift time traces for single QD (black) and QD/silica/Au (red). 77

Figure 3.8. Comparison of the averaged peak shift per frame (**a**) and 10% maximum amplitude interval of the peak shift per frame (**b**) between different species of particles: QD, QD/silica, QD/silica/Au. The acquisition time of each PL spectra frame is 2 s. 78

Figure 3.9. The emission lifetime measurements of the three kinds of particles: QD (black), QD/silica (red) and QD/silica/Au (blue). 79

Figure 3.10. The QD/silica aggregates without several cycles of sonification and centrifugation. 84

Figure 3.11. TEM images of gold shell growth with (**a**) and without (**b**) PVP. 85

Figure 3.12. BEM simulation results for plasmonic nanoshell structure. (**a**) the simulated extinction spectrum of a geometry parameter pair of $r_2 = 20$ nm and $r_3 = 10$ nm. (**b**) The electric field distribution with the same geometry parameter as (**a**). (**c**)-(**d**) The plasmon resonance of gold (**c**) and silver (**d**) nanoshell with different r_2 and r_3. 87

Figure 3.13. The SEM images of the QD/silica/gold particles on the surface with no pre-treatment (**a**) and treated with $NH_3 \cdot H_2O$ and H_2O_2 (**b**). 88

Figure 4.1. (**a**) Photograph of Ag nanoprisms with different sizes. (**b**) TEM image of Ag nanoprisms with LSPR around 600 nm. The edge length is about 50 nm. (**c**) Normalized Extinction spectra of a series of Ag nanoprisms with different sizes. 94

Figure 4.2. The TDBC absorption spectra. Black line is 10 μM aqueous TDBC solution with KCl salt. Red line is bare 10 μM aqueous TDBC solution. The inset is the molecule structure of TDBC monomer. 95

Figure 4.3. Extinction spectra showing Rabi splitting under three different coupling situations. (**a**) LSPR higher than molecular resonance. (**b**) LSPR near molecular resonance. (**c**) LSPR lower than molecular resonance. For each spectrum, grey line is the original LSPR, red line is TDBC J-aggregates absorption, blue line is the extinction of the strongly coupled system. All the spectra are normalized for better comparison. 96

Figure 4.4. The anti-crossing behavior of the two hybrid bands formed in silver nanoprism/TDBC J-aggregates strongly coupled system with different-size silver nanoprisms. The red and black dots are the splitting band energy extracted from the extinction spectra. The red and black curves are the fitting curve with eqn. 4.3. 97

Figure 4.5. SERS spectra of TDBC J-aggregates on silver nanoprisms under three different situations ($E_p>E_m$; $E_p\sim E_m$; $E_p<E_m$) at the excitation wavelength of 558 nm. E_p is the plasmon mode energy, and E_m is the J-band energy of TDBC J-aggregates. 98

Figure 4.6. Raman excitation profiles for three situations: (**a**) $E_p>E_m$ (**b**) $E_p\sim E_m$ (**c**) $E_p<E_m$. E_p is the plasmon mode energy, and E_m is the J-band energy of TDBC J-aggregates. Black dash line is the peak position of original TDBC J-band. 100

Figure 4.7. (**a**) The extinction spectrum of mixed silver nanoprism/TDBC J-aggregates with free floating TDBC J-aggregates in the solution. The red box region is the absorption of the dye. (**b**) The Rabi splitting energies of a series of silver nanoprism/TDBC J-aggregates with different added volume of TDBC J-aggregates... 104

Figure 4.8. The SERS spectrum of TDBC J-aggregates at the excitation wavelength of 558 nm. The red curve is the Lorentzian fit of the peak after the background subtraction. 106

Figure 4.9. The correlated single-particle dark field scattering(**a**) and SERS(**b**) of silver nanoprism/TDBC J-aggregates. 107

List of Tables

Table 2.1. DFT Vibrational Frequency Calculation of Different C_{60} Species 53
Table 3.1. The spectral diffusion behavior and emission lifetime of QD, QD/silica and QD/silica/Au 80

List of Schemes

Scheme 1.1. Scheme of different coupling regime between plasmon (represented by cavity) and exciton (represented by a two-level system): (**a**) Enhanced spontaneous emission rate in weak coupling regime. (**b**) Fast Rabi oscillation (coherent energy transfer between plasmon and exciton) in strong coupling regime. 25

Scheme 1.2. The anti-crossing behavior of the upper and lower polariton states. The Rabi splitting Ω_R is defined as 2g (coupling strength) at the resonance condition. 28

Scheme 1.3. Schematic illustration of nonradiative decay pathways of surface plasmon. After the plasmon generation (**a**), it quickly decayed into non-thermal distributed energetic electron-hole pairs through Landau damping (**b**). Then the hot carriers decay into Fermi-Dirac distribution by various scattering process in the structure (**c**). Finally, most of the energy is relaxed as heat and exchange with the local environment (**d**)........ 38

Scheme 1.4. Two main proposed mechanisms for plasmon-induced hot electron transfer at the metal/molecule interface: (**a**) indirect electron transfer; (**b**) direct electron transfer........ 39

Scheme 3.1. The core/spacer/shell geometry input for the electrodynamics simulation: r_1 is the QD core radius and is set to be 2 nm. r_2 is the silica thickness and r_3 is the shell thickness. The plane wave excitation is used in the simulation. 86

Scheme 4.1. The simplified energy mixing diagram for plasmon-molecule strong coupling according to JC model. The three plots represent three different situations of relative energies between plasmon mode and the molecules. 91

Scheme 4.2. The scheme of Tavis-Cumming model describing N emitters strongly coupled with one plasmon mode. 92

Scheme 4.3. The basic setup for wavelength-scanned Raman excitation spectroscopy experiments. 103

Chapter 1: Introduction

1.1 Chapter Summary

Surface plasmons generated in metal nanostructures can significantly enhance the local electromagnetic field at the surfaces of these nanostructures, which offers the possibility of remarkably manipulating the light-matter interaction on the nano-scale. In this chapter, I will first briefly introduce the fundamental concept of a plasmon, and then discuss the general description of plasmon excitation in various light-matter interaction process: 1) plasmonic enhancement in Raman scattering (section 1.3); 2) plasmon-exciton coupling, from weak coupling to strong coupling regimes (section 1.4); 3) plasmon-driven energetic carrier photochemistry (section 1.5). These concepts and topics will be explored more in detail in various research projects introduced in the following chapters through this thesis.

1.2 Basic Description of Surface Plasmon

Metal materials, like gold and silver, usually have a negative real and small positive imaginary dielectric constant. When this happens, they can support strong surface plasmon resonance excitation. From the perspective of classical electrodynamics, the surface plasmon is a coherent oscillation of conduction-band electrons at the material interface, shown as **Figure 1.1a**. Unlike bulk or film samples, the plasmon generated at the surface of metal nanostructures is more localized instead of propagating in certain directions, so such plasmon resonance is referred to as localized surface plasmon resonance (LSPR).[1] The oscillation of free electrons can remarkably enhance the local electromagnetic (EM) field near the surface of metal nanostructures (**Figure 1.1b**).[2-4] The EM field enhancement is strongly dependent on details of the structure, and usually

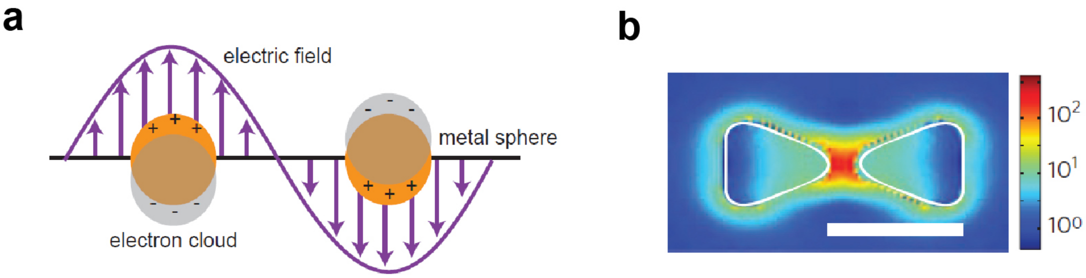

Figure 1.1. (**a**) The scheme showing the oscillation of free electrons in metal nanoparticles that generate localized surface plasmon and lead to enhanced local electromagnetic field. (**b**) Finite-difference time-domain (FDTD) calculation of local electric field enhancement of a bowtie structure. Adapted from Ref (4). Copyright 2009 Nature Publishing group.

the enhancement is significantly larger at "hot spots" (for example the gap of a bowtie structure).[4-7]

In recent years, researchers have also been developing the quantum mechanical description of plasmons, especially in small metal clusters. With time-dependent density functional theory (TD-DFT)[8-9] and Configuration Interaction (CI)[10-11] methods, plasmonic states are described as the collective combination of electron-hole excitations in metal clusters which contribute additively to the transition dipole moment. The dominant transitions are usually sp to sp intraband transitions for plasmonic states.[12]

1.3 Plasmonic Enhancement in Raman Scattering Process

When the electromagnetic radiation is scattered by atoms or molecules, it induces a dipole moment $\boldsymbol{\mu}^{\mathrm{ind}}$, which is related to the incident electric field $\boldsymbol{E}$ in a first-order approximation by:

$$\boldsymbol{\mu}^{ind} = \alpha \cdot \boldsymbol{E} \qquad (1.1)$$

where α is the polarizability tensor of the atom or molecule. Plasmonic nanostructures enhance the local electric field through LSPR excitation as discussed in section 1.2, so as eqn 1.1 shows, they are also able to enhance the optical scattering process. The most well-established spectroscopic technique developed under such principles is surface-enhanced Raman scattering (SERS), first discovered in 1977.[13-15] With rich chemical information from the molecular vibrational modes and the tremendous enhancement factor (EF) up to 10^8 compared to normal Raman scattering (NRS) signals[7, 16-17], SERS has served as one of the most sensitive analytical methods for molecule detection and analysis, and has been widely applied in single-molecule detection[18-21], biosensing[22-25], surface chemistry[26-29] and ultrafast molecular dynamics[30-32].

The enhancement mechanism of SERS has been a long-standing debate in the community. There are two main mechanisms, electromagnetic mechanism (EM) and chemical enhancement effect (CHEM), contributing to the total plasmonic enhancement factor of the Raman signal. The EM of SERS comes from the enhanced local electric field $\boldsymbol{E}$ from LSPR excitation of metal nanostructures. Since the Raman scattering involves both incident and scattered electric fields, in early theoretical modelling of SERS people usually estimate the SERS EM enhancement factor to be E^4 enhancement, as shown in eqn 1.2:[33]

$$EF = \frac{|\boldsymbol{E}_{in}|^2 |\boldsymbol{E}_{out}|^2}{|\boldsymbol{E}_0|^4} \qquad (1.2)$$

The CHEM effect represents the change of the molecular polarizability α due to the direct bonding between the molecules and the metal nanostructures.

In recent years, significant effort has been made theoretically and experimentally for quantifying the contribution for each mechanism in SERS. By conducting wavelength-scanned surface-enhanced Raman excitation spectroscopy (WS-SERES) and studying the distance-dependence SERS intensities achieved by atomic layer deposition (ALD), people confirmed that the EM is the dominant effect for enhanced Raman signals.[17, 34-35] The electromagnetic EF can be up to 10^8 and E^4 enhancement is a good approximation for EM contribution. The CHEM effect is mainly through charge-transfer character of the molecule-metal complex, which leads to an increase in polarizability.[36-37] Experiments and theory have determined a maximum of $\sim 10^3$ enhancement for the CHEM effect.[38-39]

SERS itself is a good example of plasmon-enhanced light-matter interaction. In later chapters (Chapter 2 and Chapter 4), it is also used as the analytical tool to explore different plasmon-molecule coupled systems.

1.4 Plasmon-Exciton Coupling

When excited atoms, molecules or semiconductor material are in close vicinity to plasmonic nanostructures, plasmon-exciton coupling can lead to novel optical properties of the hybrid system compared to the two separate components. Since plasmonic nanostructures can concentrate light on the nano-scale, just as optical cavities do on the micro-scale, in literature people usually treat the plasmonic nanostructure as an effective “cavity” structure when discussing plasmon-exciton coupling and many concepts from cavity electrodynamics can also be applied in plasmon-exciton coupling.[40] Different coupling strength results in different coupling behaviors, varying from the enhanced spontaneous emission rate due to the Purcell effect (weak coupling), to the coherent Rabi energy oscillation between plasmon and exciton (strong coupling), as shown in **Scheme 1.1**. The coupling strength is mainly dependent on the spectral overlap between the plasmonic mode and the exciton energy, and the local electric field generated by the plasmon resonance and felt by the exciton in the coupled system. Both factors are highly correlated with the geometries of the plasmonic nanostructures (size, shape, “hot spot” position, etc.). With the significant advances in

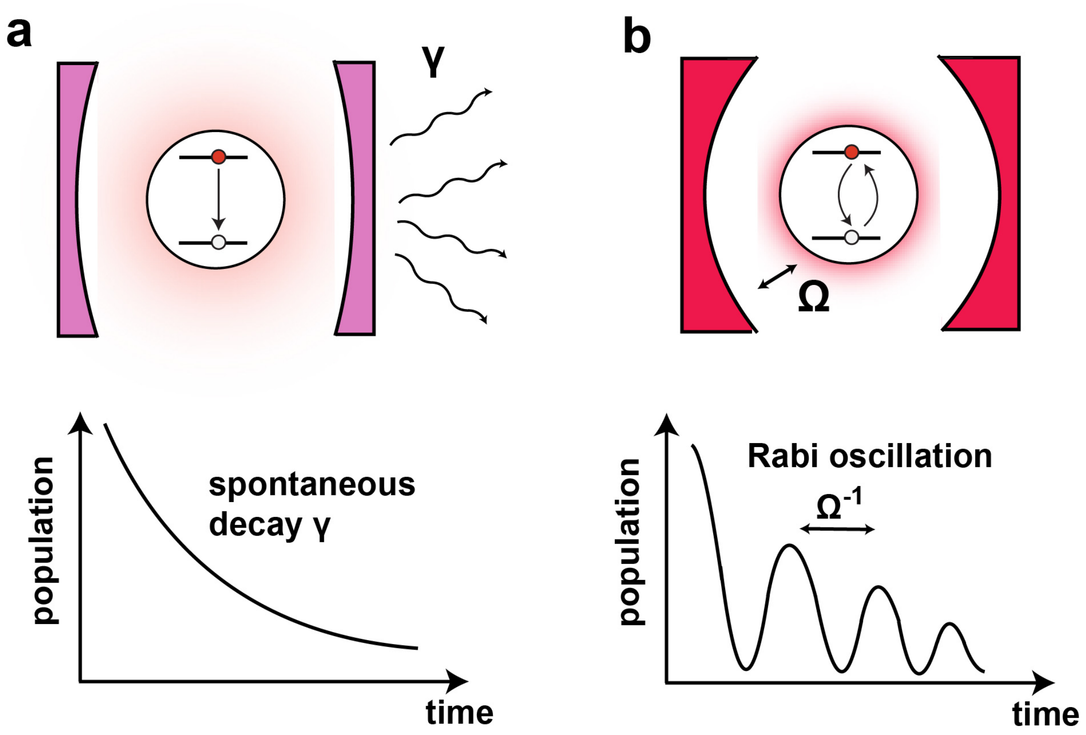

Scheme 1.1. Scheme of different coupling regime between plasmon (represented by cavity) and exciton (represented by a two-level system): (**a**) Enhanced spontaneous emission rate in weak coupling regime. (**b**) Fast Rabi oscillation (coherent energy transfer between plasmon and exciton) in strong coupling regime.

nanofabrication and synthesis techniques in recent years, researchers can more precisely design and control sophisticated plasmonic nanostructures, which makes plasmonic nanostructures a promising platform to fabricate plasmon-exciton hybrid system with different coupling strength.[41-44] In this section, I will first discuss the Jaynes-Cumming (JC) model for describing plasmon-exciton coupling and briefly derive the criteria to define different plasmon-exciton coupling regimes based on this theoretical model. Then examples involving the material design, properties, and applications of the two main coupling regimes, weak coupling and strong coupling, will be discussed.

1.4.1 Jaynes-Cumming Model

The Jaynes-Cumming (JC) Model, also known as the two coupled oscillator model, theoretically describes the hybrid system composed of a bright two-level system (TLS) interacting with a single cavity mode. In the JC model, the total Hamiltonian is written as:[45]

$$\hat{H}_{JC} = \hbar\omega_c a^\dagger a + \hbar\omega_s \sigma^\dagger \sigma - \hbar g(a^\dagger \sigma + a\sigma^\dagger) \qquad (1.3)$$

where ω_c is the cavity mode frequency, $a/a^\dagger$ is the cavity photon annihilation/creation operator, ω_s is the energy of the two-level system, $\sigma/\sigma^\dagger$ is the TLS exciton annihilation/creation operator, g is coupling strength. The coupling strength g can be expressed as:[46]

$$g = \frac{\boldsymbol{\mu} \cdot \boldsymbol{E}}{\hbar} = \left(\frac{1}{4\epsilon_0\epsilon_r}\frac{e^2 f}{mV_c}\right)^{1/2} \qquad (1.4)$$

where $\boldsymbol{\mu}$ is the transition dipole moment of the exciton, $\boldsymbol{E}$ is the local electric field the exciton feels in the cavity. ϵ_0 and ϵ_r represent the vacuum and relative permittivity, respectively. e is the free charge, f is the exciton oscillation strength, m is the free electron mass, and V_c is the effective cavity volume. From eqn 1.4 we can see that the coupling strength g is proportional to $(f/V_c)^{1/2}$, which clearly shows the contribution from exciton (oscillation strength f) and cavity (V_c): The larger the oscillation strength of the transition dipole moment (exciton side) and the smaller the effective cavity mode is (cavity side), the stronger the coupling strength g between the two components is. Plasmonic nanostructures have the advantage of small effective cavity volumes because they are known to concentrate light on nano scale, as discussed in previous sections. The effective cavity volume of plasmonic nanostructures is not easily determined from the geometry as dielectric optical cavities, so V_c is usually defined with electric field density:[47]

$$V_c = \frac{\int \epsilon_r |\boldsymbol{E}|^2 d\boldsymbol{r}^3}{\max\left(\epsilon_r |\boldsymbol{E}|^2\right)} \qquad (1.5)$$

The JC Hamiltonian has two eigenstates. Since the two eigenstates are the ground and excited state mixed with photon states in the cavity, they are usually denoted as the upper polariton state $|P+\rangle$ and lower polariton state $|P-\rangle$,[48] given as:

$$|P+\rangle = \cos(\theta_{JC})\,|g,1\rangle - \sin(\theta_{JC})\,|e,0\rangle;$$

$$|P-\rangle = \sin(\theta_{JC})\,|g,1\rangle + \cos(\theta_{JC})\,|e,0\rangle \quad (1.6)$$

$$\theta_{JC} = \frac{1}{2}\tan^{-1}[2g/(\omega_c - \omega_s)] \quad (1.7)$$

where $|g,1\rangle$ denotes the state composed of the exciton ground state and one photon state in the cavity, while $|e,0\rangle$ denotes the state composed of the exciton excited state and zero photon state in the cavity. θ_{JC} determines the contribution ratio of the polariton states from the exciton and the cavity photon state, which depend on the coupling strength g and the energy detuning between cavity photon and the exciton $\omega_c - \omega_s$.

By solving for the eigenstates of the JC Hamiltonian, the eigenvalues, which are the energies of the two eigenstates, can also be solved simultaneously:

$$\omega^{P+,P-} = \frac{\omega_c + \omega_s}{2} \pm \frac{1}{2}\sqrt{4g^2 + (\omega_c - \omega_s)^2} \quad (1.8)$$

At the resonance condition $\omega_c = \omega_s$, $|P+\rangle$ and $|P-\rangle$ have the same frequency and are equally mixed by the exciton and cavity photon state, and the vacuum Rabi splitting $\hbar\Omega_R$ is defined as $\hbar\Omega_R = 2\hbar g$. **Scheme 1.2** shows more intuitively how the energies of the two polariton states change with the detuning $\omega_c - \omega_s$, which is also referred to as anti-crossing behavior.

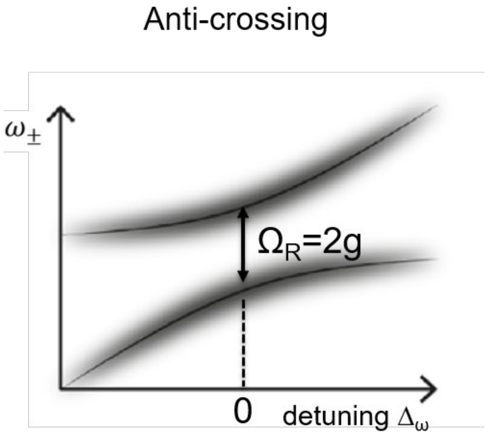

Scheme 1.2. The anti-crossing behavior of the upper and lower polariton states. The Rabi splitting Ω_R is defined as 2g (coupling strength) at the resonance condition.

Above we discussed exciton-cavity coupling in the JC model under the situation of no damping or loss processes in the system. Adding the damping processes of the exciton and the cavity, the Hamiltonian can be rewritten in the matrix format as:

$$\hat{H}_{JC,damping} = \begin{pmatrix} \omega_s - i\gamma_s & g \\ g & \omega_c - i\gamma_c \end{pmatrix} \quad (1.9)$$

Where γ_s and γ_c are the phenomenological decay rate of the exciton and the cavity, respectively. Similarly, diagonalization of the Hamiltonian $\hat{H}_{JC,damping}$ results in two hybrid eigenstates and the corresponding energies:

$$\omega^{P+,P-} = \frac{\omega_c + \omega_s}{2} - \frac{i}{2}(\gamma_s + \gamma_c) \pm \frac{1}{2}\sqrt{4g^2 + (\omega_c - \omega_s - i(\gamma_s - \gamma_c))^2} \quad (1.10)$$

As shown in eqn 1.10, the criteria for observing the energy splitting of upper and lower polariton state is first to make sure the splitting term $\sqrt{4g^2 + (\omega_c - \omega_s - i(\gamma_s - \gamma_c))^2}$ is real, which leads to:[49]

$$g > \frac{1}{2}|\gamma_s - \gamma_c| \quad (1.11)$$

However, as shown in **Scheme 1.2**, with the inclusion of damping processes for the exciton and the cavity, the energy splitting can only be spectrally resolved when the splitting energy is larger than the natural linewidth of the exciton and cavity mode (representing the damping process γ_s and γ_c, respectively). So another criteria is proposed as:

$$g > \frac{1}{2}|\gamma_s + \gamma_c| \quad (1.12)$$

When Eqn 1.11 and 1.12 are both reached, the energy splitting can be spectrally observed for the plasmon-exciton coupled system, which is defined as the strong coupling regime. If the two criteria are not met, it indicates that the system is in the weak coupling regime. In the experiments, it requires that clearly split peaks are observed in the optical spectrum (absorption, scattering or emission).

To summarize the plasmon-exciton coupling regime defined from the JC model, it mainly depends on the relationship of the coupling strength g and the damping rate of the system. In the weak coupling regime, the intrinsic wavefunctions of the plasmonic nanostructure and the exciton are not perturbed by each other. One of the main effects is that the spontaneous emission rate of the exciton is increased by the local electric field enhancement that arises from plasmon excitation, which is known as the Purcell effect. In the strong coupling regime, however, the plasmon and exciton coherently transfer excitation back and forth, so new normal modes known as polariton modes are generated.

1.4.2 Weak Coupling Regime

In this section we will mainly discuss how plasmon excitation alters emission properties of the exciton in the weak coupling regime. When the exciton couples to a radiative decay pathway, the electron and hole recombine and emit one photon. If this process happens close to plasmonic nanostructures and the plasmon-exciton coupling is still in the weak coupling regime, usually higher fluorescence intensity and faster emission rate would be observed, showing the influence of plasmonic nanostructures on both the excitation rate and decay rate.

As discussed before, the plasmonic nanostructures can serve as optical antennas or cavities to concentrate light in the region on the nano-scale, which shows strong local electric field enhancement. Since the excitation rate $\gamma_{exc} \propto |\boldsymbol{\mu} \cdot \boldsymbol{E}|^2$ ($\boldsymbol{\mu}$ is transition dipole moment, $\boldsymbol{E}$ is the local electric field), the strong local electric field enhancement by plasmonic nanostructure naturally leads to a higher excitation rate of the emitter. Anger et al. studied the fluorescence rate of a single dye molecule quantitatively as a function of its distance to a gold nanoparticle attached at the end of an optical fiber.[50] From the distance of 60 nm to around 5 nm, a significant increase in fluorescence signal was observed. At the distance of 5 nm the fluorescence intensity reached to the maximum and started to decrease at closer distance. The fluorescence quenching at closer Au nanoparticle-dye distance is due to the direct energy transfer between the gold nanoparticle and dye molecule and decrease the fluorescence quantum yield of the dye. Chen et al investigated the excitation enhancement effect more carefully using photoluminescence excitation (PLE) spectroscopy.[51] They attached silver nanoprisms on the CdSe/CdS/CdZnS/ZnS core/multi-shell quantum dot (QD) PMMA film as the plasmon-exciton coupled system. The PLE spectra closely followed the LSPR of the silver nanoprisms, demonstrating the contribution of excitation enhancement to the total fluorescence intensity enhancement. They also found a maximum excitation enhancement of ~10 for silver nanoprisms and ~3 for other metal nanoparticles.

Purcell first discovered in 1946 that the spontaneous transition rate of a nuclear magnetic moments could be enhanced when coupled to a resonance electrical circuit.[52] Later people also found this rule can generally applied to other spontaneous process affected by the local environment. For example, the spontaneous emission rate can be remarkably enhanced within some environment, like optical cavities, compared to the free space. These phenomena are referred to as the Purcell effect. The enhancement associated with the Purcell effect is called the Purcell factor. If we again treat plasmon nanostructures as an effective optical cavity, the quantitative description and physical meaning of the Purcell effect can be derived from Fermi's golden rule.[53]

From the first-order time-dependent perturbation theory (also known as Fermi's golden rule), the spontaneous emission rate from state *m* to state *k* into the solid angle $d\Omega$ can be written as:

$$dw_{em}(m \rightarrow k) = \frac{1}{\tau_{sp,free}} = \frac{2\pi}{\hbar}|U_{km}(-\boldsymbol{k})|^2 \rho(E_m - \hbar\omega) \quad (1.13)$$

The interaction term $|U_{km}(-\boldsymbol{k})|^2$ and the photon density of states $\rho(E_m - \hbar\omega)$ are expressed as:

$$|U_{km}(-\boldsymbol{k})|^2 = \frac{A_0^2\omega^2}{4c^2}|\boldsymbol{\mu}_{km} \cdot \boldsymbol{E}|^2 \quad (1.14)$$

$$\rho(E) = \frac{n^3 V}{(2\pi c)^2}\frac{\omega^2}{\hbar}d\Omega \quad (1.15)$$

And then we can get an expression for spontaneous emission rate in free space:

$$\frac{1}{\tau_{sp,free}} = \frac{n^3\omega^3}{3\pi c^3 \varepsilon \hbar}|\boldsymbol{\mu}_{km}|^2 \quad (1.16)$$

For the situation in the cavity, the photon density of states $\rho(E)$ is increased:

$$\rho(E) = \frac{2}{\pi\hbar\Delta\omega_c} \quad (1.17)$$

where $\Delta\omega_c$ denotes the linewidth of the cavity. Defining the cavity quality factor as $Q \stackrel{\text{def}}{=} \frac{\omega_c}{\Delta\omega_c}$ and using the definition of effective cavity volume (eqn 1.5), we can get the altered emission rate in the cavity as:

$$\frac{1}{\tau_{sp,c}} = \frac{2}{\hbar\varepsilon}|\boldsymbol{\mu}_{km}|^2\frac{Q}{V_{eff}} \qquad (1.18)$$

Then the Purcell factor *F* is defined as the ratio of emission rate with and without the cavity:

$$F = \frac{1}{\tau_{sp,c}}\Big/\frac{1}{\tau_{sp,free}} = \frac{3}{4\pi^2}\frac{Q(\lambda/n)^3}{V_{eff}} \qquad (1.19)$$

Since the Purcell factor is proportional to Q/V_{eff}, experimentally there are usually two design strategies to increase the spontaneous emission rate, which are coupling the emitter to the cavity with high quality factor Q or small cavity mode volume V_{eff}. In most of the cases, coupling to the plasmonic nanostructures (especially "hot spot" region) belongs to the latter strategy, which mainly utilizes the extremely small effective cavity volume of the plasmonic nanostructures.

The Purcell factor can be estimated experimentally by excited state lifetimes using time-resolved photoluminescence (TR-PL) measurements. TR-PL utilizes the technique of time-correlated single photon counting (TCSPC) based on the principle of repetitive, precise time registration of single photon in the fluorescence signal usually with single-photon avalanche diode and correlation electronics.[54] Munechika et al. examined the radiative decay rate of CdSe QDs in absence of excitation enhancement with a single silver nanoparticle using TR-PL and theory.[55] They found about ~4-fold decrease in the emission lifetime, and that the ratio of radiative decay rate to nonradiative decay rate is proportional to the silver nanoparticle scattering efficiency.

To achieve maximized spontaneous emission rate, lots of effort has been paid to material design, especially optimization on various metal nanostructures. In the simplest cases, gold or silver nanoparticles with different shapes are used to enhance the emission rate. Yuan et al used a single gold nanorod to enhance the fluorescence of single crystal violet dye molecule in the solution.[56] They observed an up to ~1100 times fluorescence intensity increase compared to a single dye molecule only in the solution. Ge et al. fabricated the hybrid plasmonic nano-emitter with single gold nanocube as plasmonic optical antenna and CdSe QD as emitter.[57] They applied a two-photon radical polymerization fabrication method to control the emitter attached to the specific corner of the nanocube, which makes the hybrid structure anisotropic. They not only observed ~24 times decrease in the emission lifetime, but also found different emission states corresponding polarization-sensitive nanoscale overlap between local electric field and the emitter distribution.

Since "hot spot" structures usually have higher local electric field enhancement compared to metal nanoparticles, various kind of structures with nanogap have been studied to enhance the emission of the emitter. One of the most typical "hot spot" structures is nanoparticle dimers. Kinkhabwala et al constructed gold bowtie structures with electron-beam lithography (EBL) nanofabrication method and observed an enhancement of the single dye molecule fluorescence intensity of ~1340 when the dye molecule is located in the nanogap of the bowtie structure.[4] Besides the EBL nanofabrication method, Zhang et al used a DNA-based self assembly method to probe a single quantum dot in the DNA origami structure linked by two gold nanoparticles at the two ends.[58] This self assembly method can precisely control the relative geometry position of quantum dots and the gold nanoparticles in the hybrid cluster. The researchers not only observed the plasmon enhanced fluorescence and shortened lifetime, but also demonstrated that the emission of the designed cluster is polarized and is governed by the geometry detail of the gold nanoparticles and the quantum dots. Another kind of "hot spot" structure is composed of a nanoparticle and a metal film, which is also referred to as nanoparticle-on-mirror (NPOM) structure. The fabrication process of NPOM is relatively easier than the dimer structure but with less precise control. Hoang et al. examined the emission properties of single quantum dot in the NPOM structure, constructed by a silver nanocube and a gold film.[59] The cavity volume, or the distance between the silver nanocube and gold film can be controlled by the dielectric PMMA spacer film. They found that this NPOM can produce 540-fold decrease in emission lifetime and 1900-fold increase in fluorescence intensity compared to single quantum dot. Other kinds of nanogap structures following the design of dielectric resonators or cavities, like gold bullseye resonators,[60] multiple gold nanorods arranged in a U-shape,[61] a hexagonal array of nanoholes in a gold film,[62] a plasmonic nanoshell,[63-64] etc., have also been applied in plasmon-exciton coupling structure to achieve higher emission rate.

Above we discussed the situation that only one type of exciton coupled with plasmon. When a pair of energy donor and acceptor is coupled to plasmon, the energy transfer rate can also be enhanced, which is denoted as plasmon-coupled resonance energy transfer (PC-RET). Zhang et al. studied the distance-dependence of the energy transfer between donor and acceptor quantum dot films sandwiching a layer of gold nanoparticles.[65] They found efficient energy transfer rate was still observed when the distance is at 20 nm. Anderson et al. utilized DNA origami self assembly technique to fabricate and precisely control the hybrid structure composed of gold nanoparticle, donor and acceptor molecules, which makes it possible to study PC-RET on single molecule and single particle level.[66] Theoretical work have also been done on this topic. Ding, Hsu et al. derived a classical electrodynamics expression for PC-RET rate W_{ET} (shown as eqn 1.20):[67-68]

$$W_{ET} = \frac{9c^4 W_D^r}{8\pi} \int d\omega \frac{\sigma(\omega) I(\omega)}{\omega^4} \left| \frac{\mathbf{e_A} \cdot \boldsymbol{E}^D(r_A, E)}{p_{ex}(E)} \right|^2 \qquad (1.20)$$

Eqn 1.20 express the PC-RET rate associated with the spectral overlap between donor absorption $\sigma(\omega)$ and acceptor emission $I(\omega)$, and a coupling factor $\left|\frac{\mathbf{e_A}\cdot\boldsymbol{E}^D(r_A,E)}{p_{ex}(E)}\right|^2$ ($\mathbf{e_A}$ represents the acceptor transition dipole direction, $\boldsymbol{E}^D$ represents the electric field). This classical expression decomposes the problem of calculating the PC-RET rate to solving the electric field of the system instead of using dyadic Green's functions. Jeong et al. further improved the theoretical model for PC-RET so that detailed geometrical factors, like the direction of the donor/acceptor dipoles, can be included in the model.[69]

1.4.3 Strong Coupling Regime

As discussed in section 1.4.1, the main criteria for the plasmon-exciton coupling system to be in the strong coupling regime is $g > \frac{1}{2}|\gamma_s + \gamma_c|$. The coupling strength g for the situation of single-exciton coupling is expressed in eqn 1.4: $g = \frac{\boldsymbol{\mu}\cdot\boldsymbol{E}}{\hbar} = \left(\frac{1}{4\epsilon_0\epsilon_r}\frac{e^2 f}{mV_c}\right)^{1/2}$, and it is not hard to generalize into the situation of multiple excitons (represented by the number N) coupling: $g = \sqrt{N}\frac{\boldsymbol{\mu}\cdot\boldsymbol{E}}{\hbar} \propto \sqrt{N}(f/V_c)^{1/2}$.

Considering the expression for the coupling strength g, the most straightforward method is to increase the number of excitons N involved in the hybrid system.[70] However, increasing the number of excitons can also bring in a large number of dark states,[48] which could make the system too complicated. The main effort in material design towards plasmon-exciton strong coupling has focused on: 1) using the exciton with a high transition dipole oscillation strength f; 2) engineering the plasmonic nanostructures to achieve a smaller mode volume V_c or higher quality.

On the exciton side, various strong emitters have been used to achieve the strong coupling regime. One large category is organic dye molecules,[71-72] especially dye J-aggregates.[73-75] Compared to the dye monomers, the absorption and emission of J-aggregates are red-shifted and have much narrower linewidth, which indicates a much stronger oscillator strength. Semiconductor nanocrystals are another popular candidate used in achieving the strong coupling regime, like semiconductor quantum dots[76-77] and transition metal dichalcogenides (TMDC) 2D nanomaterials[78-79]. The small size of QDs leads to discrete energy levels as a result of the quantum confinement effect, and its band-edge absorption and emission can be easily tuned by controlling the size or shelling multiple layers during the colloidal synthesis. The monolayer or few-layer of 2D materials usually have large transition dipole moments, and their atomically flat surface can be easily engineered to couple with various plasmonic nanostructures. Furthermore, semiconductor materials have higher photostability compared to organic dye molecules, which also makes them good candidates for fabricating plasmon-exciton strong coupling hybrid system.

For the plasmon side, although bare metal nanoparticles are also used to strongly couple with excitons, the more common choice is still nanogap or “hot spot” nanostructures like dimers or NPOM structures since they have significantly smaller effective cavity mode volume.[76, 80-81]

Dynamic control of the plasmon-exciton strong coupling system has also been achieved, mainly by using photochromic dye molecules. Schwartz et al. coupled photochromic spiropyran (SPI) molecules with a silver film and demonstrated reversible switching between weak and strong coupling regime with all-optical control.[82] SPI molecules themselves are not very emissive, but they can go through ring-opening reaction under UV light (reverse back under visible light) and form merocyanine (MC) dye molecules which have strong oscillation strength, which can be strongly coupled to the silver film. This photo-switch strategy to reversibly control weak and strong coupling has also been proven in other plasmonic nanostructures.[83-84] Besides using optical control, Kato et al. achieved active control of strong coupling states between dye molecules and gold nanostructures with electrochemical control.[85] In this work, the coverage of HITC dye molecules on gold surface can be reversibly tuned by the electrochemical potential so that different coupling strengths were achieved.

The plasmon-exciton strong coupling can generate two hybrid states, and their spatial coherence and temporal response have been further studied to explore the intrinsic properties of strong coupling regime. Guebrou et al. demonstrated long-range spatial coherence of the polariton states in the organic dye J-aggregates/silver strongly-coupled hybrid system with Young-type interferometric experiments.[86] Two slits separated by several micrometers were placed at the intermediate image plane on the emission path of J-aggregates/silver film sample on the microscope, and the interference patterns were captured on the CCD camera, while there was no interference fringes observed for a J-aggregates film or other weak coupling system. The results clearly demonstrated the spatial coherence of the hybrid states generated from strongly coupled plasmon-exciton system, and the spatial coherence length can be on the order of few micrometers. Similar interferometric experiments on different plasmon-exciton strongly coupled system have been reported and showed similar results.[87-88] For the temporal response, Vasa et al. observed real-time Rabi-oscillation with time period of tens of femtoseconds using pump-probe spectroscopy.[89] The long spatial coherence length and fast real-time Rabi-oscillation response make the plasmon-exciton strongly coupled system the unique building blocks in novel optic devices on the nano scale.

1.5 plasmon-Driven Hot Carrier Photochemistry

1.5.1 Plasmon Decay Process

In the classical physical picture, the plasmon is a collective oscillation of free electrons in metal nanostructures when illuminated by light. Unlike semiconductor nanocrystals, photoluminescence is very inefficient for metal nanoparticles. Gittins et al found that the photoluminescence efficiency for optically excited spherical gold nanoparticles is 10^{-6}.[90] Instead the main plasmon decay pathway is to nonradiatively create energetic hot carriers (electrons and holes) via Landau damping, as shown in Scheme **1.3b**.[91] Ultrafast spectroscopies and theory work have demonstrated that the initial hot carrier distribution is non-thermal, but is more a combination of a thermal-like peak near Fermi level and a relatively flat distribution up to the excitation energy.[92-93] Then these energetic carriers immediately redistribute their energy into Fermi-Dirac distribution due to electron-electron scattering and electron-phonon scattering process in the nanostructure. Time-resolved

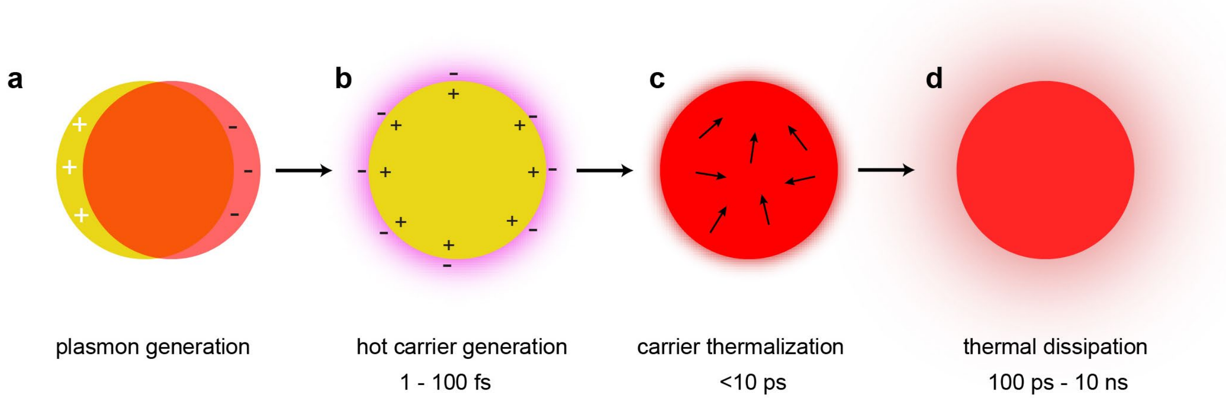

Scheme 1.3. Schematic illustration of nonradiative decay pathways of surface plasmon. After the plasmon generation (**a**), it quickly decayed into non-thermal distributed energetic electron-hole pairs through Landau damping (**b**). Then the hot carriers decay into Fermi-Dirac distribution by various scattering process in the structure (**c**). Finally, most of the energy is relaxed as heat and exchange with the local environment (**d**).

reflectivity measurements, as well as ab initio calculations, have suggested that the total relaxation time of hot carriers into a thermal distribution is on the order of hundreds of femtoseconds to several picoseconds, which is also dependent on many factors like material, size, local environment, etc.[94-95] Finally after the electron-phonon scattering process, most of the energy is transferred to the local environment and dissipated as heat.

1.5.2 Proposed Mechanisms of Plasmon-Driven Chemical Reactions

During the plasmon decay process, the generated energetic electron-hole pair can be utilized to trigger chemical reactions at metal/molecule interfaces. There have been mainly two types of mechanisms proposed in the literature to explain the plasmon-driven hot carrier transfer from metal nanostructures to the nearby reactant molecules: indirect carrier transfer and direct carrier transfer (illustrated in **Scheme 1.4**). **Scheme 1.4** only plotted the situation considering electron transfer. The hole transfer process is also similar, and we will just discuss electron transfer in this section for convenience. First both mechanisms require the lowest unoccupied molecular orbital (LUMO) of the reactant molecule to have overlap with the hot electron energy distribution generated from

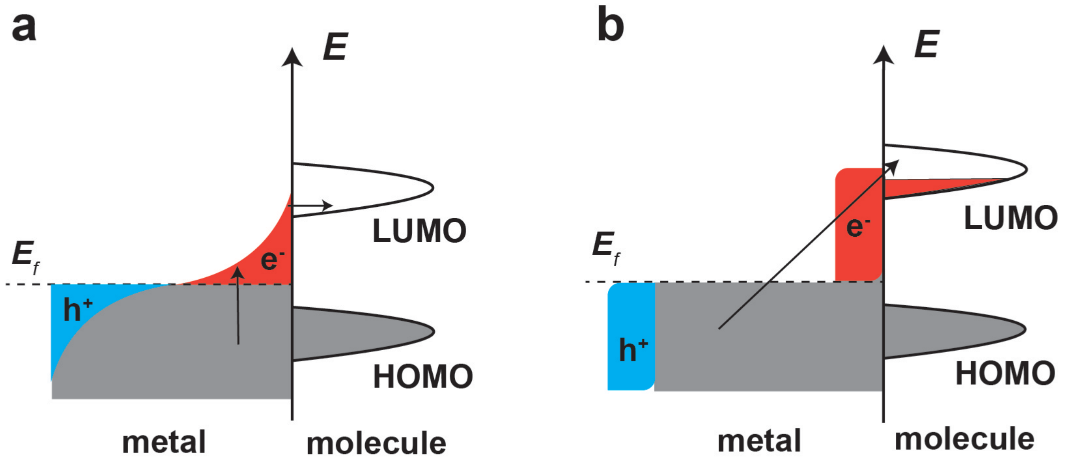

Scheme 1.4. Two main proposed mechanisms for plasmon-induced hot electron transfer at the metal/molecule interface: (**a**) indirect electron transfer; (**b**) direct electron transfer.

plasmon decay so that the electron transfer rate is sufficient enough for the reaction. The indirect electron transfer mechanism assumes that the hot electrons first are generated in the metal nanostructure and quickly go through a thermalization process, and then sequentially some of the hot electrons transfer to the LUMO of the nearby molecules, similar to the situation of energetic carriers crossing the Schottky barrier at semiconductor interfaces. It is expected that higher incident photon energy can result in higher indirect electron transfer rate, since more high-energy electrons can be generated with higher excitation energy. For direct electron transfer mechanism, however, it assumes that the nearby molecules and the metal nanostructures form hybridized charge-transfer (CT) states. During the plasmon decay process, the generated hot electrons directly transit into the hybridized states and trigger the subsequent chemical reactions. Compared to the indirect electron transfer mechanism, the direct electron transfer mechanism has the additional requirement that the reactant molecules need to be chemically absorbed to metal surface and form hybridized states. Since direct electron transfer happens during Landau damping of the plasmon, it should have higher electron transfer efficiency and lower energy loss.[96] Furthermore, the direct electron transfer rate should have an excitation wavelength dependence related to the detailed energy levels of the hybridized CT states instead of monotonous increase with excitation photon energy as in the indirect electron transfer mechanism.

Another minor but possible mechanism is local heating mechanism. Basically, this utilizes the generated heat at the end of plasmon decay to trigger chemical reactions, which is an ensemble effect and not as efficient as the two carrier transfer mechanisms discussed above. Bora et al. reported that the apparent quantum yield of the photocatalytic degradation of methylene blue is six times higher under resonant excitation condition on the gold-nanoparticle-coated zinc oxide nanorods, at which the surface temperature reached to 300ºC, than bare zinc oxide nanorods.[97] However, Keller et al. utilized ultrafast surface-enhanced Raman thermometry technique to demonstrate that the change of the effective temperature the reactant molecules feel at a single gold nanoparticle dimer nanogap is less than 100 K, which proves that the local heating effect is not the main mechanism for plasmon-driven photoreactions.[32]

1.5.3 Examples of Plasmon-Driven Chemical Reactions

In this section some of the plasmon-driven photochemical reactions following either indirect or direct carrier transfer mechanism will be introduced.

Small molecules dissociation has been a large category of chemical reactions studied in the field of plasmon-driven photochemistry. For example, researchers have intensively studied on the elementary H_2 dissociation reactions on gold nanoparticles or gold-semiconductor interfaces.[98-100] With isotope gas analysis methods, the H_2 dissociation is explained by the indirect electron transfer mechanism: the thermalized hot electrons generated in gold nanoparticles transfer to the antibonding orbital of H_2 when H_2 approaches the Au surface and form negatively charged species $H_2^{\delta-}$. Then the unstable $H_2^{\delta-}$ quickly transfers the charge back to Au and remains in the anti-bonding excited state with a stretched H-H bond, which finally leads to H_2 dissociation. In recent studies, the strategy of using bimetallic nanoparticles (one serves as optical antenna and generates a plasmon, the other serves as the catalytic site) have been applied to study ammonia dissociation.[101]

Plasmon-driven photochemistry can also be applied to organic reactions. Boerigter et al. examined the transformation of methylene blue chemisorbed on silver nanocubes with surface-enhanced Raman spectroscopy and found charge-transfer features when selectively illuminated by the resonant excitation wavelength 785 nm.[102] It further confirms that the reactant molecules needs to be chemically bonded to the metal surface for the direct carrier transfer mechanism, but chemisorption is not the sufficient condition for direct carrier transfer to happen. Researchers also found other organic reactions with chemisorbed reactants in plasmon-induced reactions follow the indirect carrier transfer mechanism, like 4-nitrothiophenol (4-NTP) reduction,[103] 4-NTP dimerization,[104] Suzuki coupling reaction,[105] etc.

1.6 Thesis Overview

This thesis focuses on exploring the plasmon effect on light-matter interactions in the hybrid nanostructures composed of plasmon/molecule or plasmon/semiconductor interfaces. It is important to understand the role of the plasmon in different coupling situations, and this can pave the pathway to rational design of plasmonic nanostructures in the application of optical nanodevices, photochemistry, etc.

Chapter 2 describes the study of a plasmon-driven electron transfer reaction between gold nanoparticles and electron acceptor molecule PCBM with surface-enhanced Raman spectroscopy, not only demonstrating the contribution of both intraband and interband transitions in gold nanoparticles to the electron transfer process, but also showing SERS as a powerful analytical technique to monitor reactions happening on the nano scale. Chapter 3 explores a novel hybrid core/spacer/shell nanostructure of QD/silica/gold achieved by a colloidal synthesis method. The gold nanoshell structure is proven to be an effective cavity limiting the spectral diffusion behavior of single quantum dot under room temperature conditions, mainly through the Purcell effect. Chapter 4 focuses on Raman excitation profile study of a plasmon-exciton strongly coupled system composed of silver nanoprisms and TDBC J-aggregates. The excitation wavelength dependence of this plasmon-exciton strongly coupled system reveals the generation of dark states besides the two hybrid polariton states and the contribution of the dark states to Raman signals.

Chapter 2: SERS study of plasmon-driven hot electron transfer between gold nanoparticles and PCBM

Adapted from:

Wu, Y.; Yang, M.; Ueltschi, T. W.; Mosquera, M. A.; Chen, Z.; Schatz, G. C.; Van Duyne, R. P., *The Journal of Physical Chemistry C* **2019,** *123* (49), 29908-29915.

2.1 Chapter Summary

Plasmonic nanostructures have been widely used in photochemical reactions to enhance reaction rates, decrease energy barriers, or change reaction pathways, but the detailed mechanisms of these plasmon-driven processes have not been well understood. This chapter describes the application of continuous-wave (CW) pump-probe surface-enhanced spectroscopy (SERS) method to systematically investigate the plasmon-driven hot electron transfer mechanism between gold nanoparticles and [6,6]-phenyl-C_{61}-butyric acid methyl ester (PCBM). The Raman peak shift of the PCBM pentagonal pinch mode was used as an indicator of the electron transfer process, which is verified using electrochemical SERS (EC-SERS) and density functional theory (DFT) calculations. Using wavelength-scanned pump-probe SERS and DFT calculations, we found that hot electrons generated from both intraband and interband transitions can transfer from gold nanoparticles to PCBM through the indirect electron transfer mechanism. Photothermal effects do not play a significant role in the process, as demonstrated by an effective vibrational temperature calculated using the anti-Stokes/Stokes Raman intensity ratio. These experiments in combination with DFT calculations not only clarify the detailed reaction mechanism, but also provide more insight into rules for designing rational reaction pathways for plasmon-driven chemistry.

2.2 Introduction

The interaction between photons and gold or silver metal nanoparticles can generate collective oscillation of conduction electrons referred as to localized surface plasmon resonance (LSPR).[106] This excitation significantly enhances the incident and scattered electromagnetic fields near the surface of metal nanoparticles, leading to the important application of surface-enhanced Raman spectroscopy (SERS).[13, 107] Furthermore, during the nonradiative decay of plasmons, energetic ("hot") carriers with a non-equilibrium energy distribution are generated within the plasmonic nanoparticles. These hot electrons and holes transfer to nearby semiconductors or molecules on the femtosecond timescale[108-109] and subsequently induce chemical reactions, a process referred to as plasmon-driven chemistry, which offers the possibility of improving quantum yields and finding new reaction pathways.[98, 105, 110-113]

Despite the extensive applications of plasmonic nanostructures in photochemistry, the detailed mechanism of plasmon-driven chemistry is still under debate.[32, 101-102, 114-121] First, hot carriers can be generated through both intraband and interband transitions, depending on excitation energy.[122] Ultrafast spectroscopy experiments and theoretical calculations show that the two transition processes lead to significantly different hot carrier distributions, but the contributions of intraband and interband transitions to hot-carrier chemistry remains unclear.[123-125] Second, different mechanisms have been proposed for the hot carrier transfer process, including hot carrier injection across the metal-molecule interface into orbitals of the reactants (indirect carrier transfer mechanism) and direct transfer of hot carriers into the hybridized orbitals formed by the plasmonic nanostructure and adsorbed molecules (direct carrier transfer mechanism).[108, 116, 121, 126-127] Furthermore, The roles of local heating and optical pumping effects have also been discussed in plasmon-driven chemistry.[128-130]

In this chapter, we explore the detailed mechanisms of plasmon-driven hot electron transfer between gold nanoparticles (AuNP) and the fullerene derivative PCBM ([6,6]-phenyl-C_{61}-butyric acid methyl ester) using SERS and density functional theory (DFT). Here PCBM is chosen as a good electron acceptor for its high electron affinity, which makes PCBM together with gold nanoparticles a good model system to study plasmon-driven electron transfer. In the experiments, one continuous-wave (CW) pump laser excites the plasmon resonance in the gold nanoparticles, and the anion species are detected by SER signals probed by the other CW laser. This similar setup has also been used in previous plasmon-driven chemistry studies, showing significant sensitivity to transient species (negative ions, isomerized neutrals) in plasmon-driven chemical processes.[131-133] The pump power and wavelength dependence of this plasmon-driven electron transfer process was systematically explored, indicating that both interband and intraband transitions contribute to hot electron generation at different excitation frequencies, following the indirect electron transfer mechanism. In addition, SERS thermometry measurements excluded the influence of photothermal effects in this experiment.

2.3 Results and Discussion

2.3.1 Preparation of AuNP-PCBM Composite and the Extinction Spectra

The gold nanoparticle aggregates with PCBM were prepared by solution mixing and stabilized with Polyvinylpyrrolidone (PVP) coating (details can be seen in Experimental Methods, section ***2.4.1***). The extinction spectrum of gold nanoparticles aggregates with PCBM in DMF (**Figure 2.1**) reveals two plasmon resonances in the gold nanoparticle colloid after aggregation. The resonance at 539 nm corresponds to the LSPR of the Au monomer. The broad feature around 750 nm mainly involves multicore (dimer, trimer, etc.) resonances, indicative of the formation of hot spots. This peak assignment is confirmed by the comparison of extinction spectra of gold nanoparticles before and after aggregation. The monomer plasmon resonance (around 539 nm) did not change before and after the aggregation (**Figure 2.1**), showing that the gold nanoparticles were not over-aggregated.

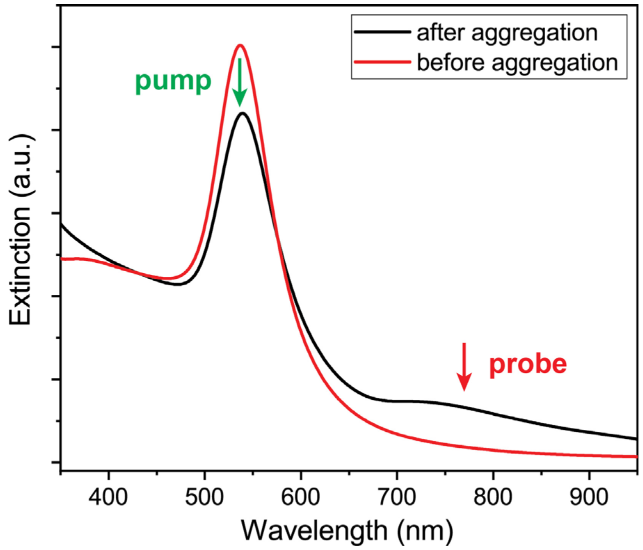

Figure 2.1. The extinction spectra of gold nanoparticle colloid in water (red curve) and gold nanoparticle aggregates with PCBM in DMF. CW 532 nm and 785 nm lasers were used as pump and probe respectively in the experiments.

2.3.2 CW Two-color SERS Experiments on AuNP-PCBM Composite

The gold nanoparticles were photoexcited by a 532 nm laser which is resonant with the monomer plasmon resonance. Meanwhile, SER signals of PCBM in hot spots were probed by a 785 nm laser, which is resonant with multicore plasmons ("hot spots"). For the analysis of SER spectra, we focused on the peak shift of the PCBM pentagonal pinch mode (classified as $A_g(2)$ mode) at 1458 cm^{-1},[134-136] because this vibrational mode has a strong Raman intensity and is very sensitive to the electron density of the molecule, with about a 6 cm^{-1} frequency shift towards lower wavenumber for each electron added to the ring.[136-137] **Figure 2.2a** shows a continuous collection of pump-probe SER spectra (waterfall plot). Each frame was acquired for 2 seconds with a 100 μW 785 nm probe laser. At frame number 30, the 150 μW 532 nm pump laser was unblocked to excite hot electrons in the Au nanoparticles. A 6 cm^{-1} frequency shift of the $A_g(2)$ mode appears in the same frame, indicating that the timescale of this plasmon-driven electron transfer process is at least within seconds. The control experiment was performed to confirm that the peak shift of PCBM pentagonal pinch mode is not affected by the 785 nm probe laser. Figure 2.2b shows a time trace of PCBM SER spectra under 785 nm probe laser illumination. There was no peak shift or linewidth change with 785 nm probe laser only on the gold nanoparticle/PCBM samples. Thus, it demonstrates that 785 nm laser is a good SERS probe for the gold nanoparticle aggregates with PCBM molecules.

The pump power dependence of the peak shift of the PCBM pentagonal pinch Raman mode was further explored. As shown in **Figure 2.2c**, the peak shift of this mode increases with the higher power of the pump laser, indicating that more plasmon-driven hot electron transfer events occur between excited gold nanoparticles and PCBM molecules. At even higher pump laser power, (450 μW in **Figure 2.8** in Supporting Information section), the PCBM $A_g(2)$ Raman mode experienced a significant intensity decrease and much larger peak broadening, with other peaks appearing in the SER spectrum. All these features indicate that PCBM molecules in the hot spot were photodegraded when pump laser power is too high.

Figure 2.2d summarizes the trend, showing the peak shift versus pump power: the peak shift increases faster for lower power, and slows down at higher power. The highest pump power in the figure was 375 μW and each SER spectrum was checked to avoid the situation of photodegradation as mentioned above. This sublinear behavior can be explained using a simple kinetic model. Consider the electron transfer reaction:

$$\mathrm{PCBM} + e^{-} \underset{k_{-1}}{\overset{k_1}{\rightleftharpoons}} \mathrm{PCBM}^{-}$$

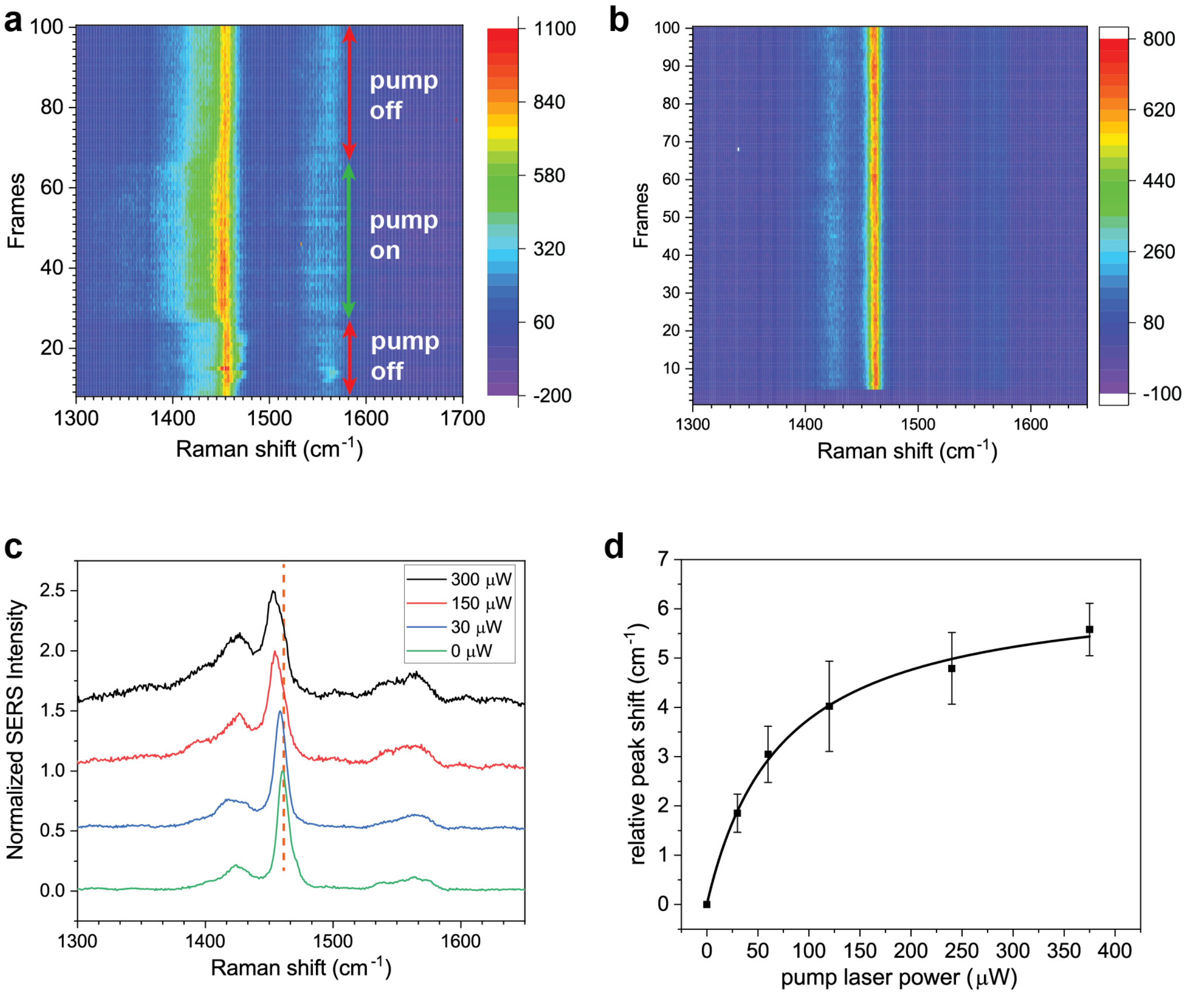

Figure 2.2. (**a**)(**b**) PCBM SER spectra as a function of time with 532 nm CW pump laser excitation (a) and 785 nm CW probe laser only (b). The acquisition time of each frame was 2 seconds. The power of the probe laser was 100 μW. (**c**) PCBM SER spectra under different pump laser power. The power of the probe laser was 100 μW. The orange dashed line is at 1458 cm^{-1} to guide the view. (**d**) Pump power dependence of the peak shift of the 1458 cm^{-1} pentagonal pinch mode. The data was fitted with Eq 2.2, shown as the black curve.

where k_1 and k_{-1} are the rate of PCBM accepting one electron and PCBM$^-$ losing one electron, respectively. Here we assume the number of photogenerated electrons e$^-$ is proportional to the pump laser intensity I_L. Similar to the Langmuir adsorption model, the ratio θ of the concentration of PCBM anions [PCBM^{-}] and the concentration of all the PCBM molecules [PCBM]$_0$ in the hot spot can be derived based on the steady state approximation (detailed derivations are in the Supporting Information section 2.6.2):

$$\theta = \frac{[\mathrm{PCBM}^{-}]}{[\mathrm{PCBM}]_0} = \frac{K'_{\mathrm{eq}} I_{\mathrm{L}}}{1 + K'_{\mathrm{eq}} I_{\mathrm{L}}} \qquad (2.1)$$

Here K'_{eq} is a constant proportional to the equilibrium constant $\frac{k_1}{k_{-1}}$. Assuming the relative peak shift of the pentagonal pinch mode $\Delta\omega$ is proportional to the ratio θ:

$$\Delta\omega = \Delta\omega_{\max}\theta = \Delta\omega_{\max} \frac{K'_{\mathrm{eq}} I_{\mathrm{L}}}{1 + K'_{\mathrm{eq}} I_{\mathrm{L}}} \qquad (2.2)$$

Here $\Delta\omega_{\max}$ is the maximum peak shift for plasmon-driven PCBM reduction under 532 nm pump laser illumination. Eq 2.2 shows a sublinear relationship between θ and pump laser power I_{L}. Furthermore, by fitting the data points in Figure 2d, $\Delta\omega_{\max}$ is 6.5 cm^{-1}, which is very close to the vibrational mode calculations for the PCBM anion (**Table 2.1**). This simple kinetic model also demonstrates that the peak shift of the PCBM 1458 cm^{-1} Raman mode is a good indicator of the amount of generated PCBM anions.

2.3.3 Electronic Structure of PCBM Adsorbed on Au Surface

To understand the electronic states involved in the system, the electronic structure of PCBM adsorbed on an Au (111) surface was calculated using DFT with the Siesta code (details seen in Methods), with the adsorption geometry shown in **Figure 2.3a**. We model the Au surface using a periodic 4-layer slab and neglect the effect of single adatoms on the surface. As shown in **Figure 2.3b**, the Fermi level of the system is at -2.81 eV. The HOMO and LUMO of PCBM are at -4.19 eV and -2.61 eV, respectively. The LUMO of PCBM is only 0.2 eV above the Fermi level, indicating that the energy barrier for the generated hot electrons to transfer to PCBM is small. The present DFT calculation provides a qualitative picture of the energy alignment of the PCBM molecule adsorbed on the surface. Because DFT calculations with GGAs tend to underestimate the separation between energy levels, the LUMO of the PCBM molecule may be located above the Fermi level by an amount of energy slightly higher than 0.2 eV. DFT calculations on a PCBM/Au_{20} cluster model of the adsorbate structure also show clear charge-transfer character (Supporting Information section, **Figure 2.10**). These theoretical calculations demonstrate that the PCBM/AuNP system is a good model system for studying the plasmon-driven electron transfer process.

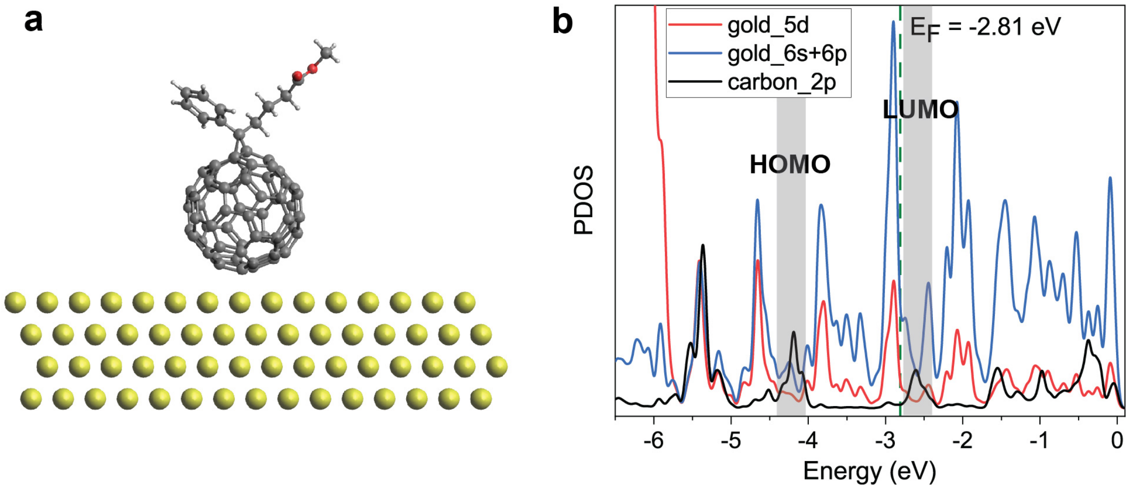

Figure 2.3. (**a**) Simulation model for the DFT band structure calculation for PCBM on an Au (111) surface. Color code: C, gray; O red; H, white; Au, yellow. (**b**) Calculated projected density of states of PCBM and gold. The Fermi level of the system is at -2.81 eV. The grey strips in the figure show the HOMO and LUMO position of PCBM.

2.3.4 Confirming the Correlation between PCBM 1458 cm^{-1} Raman Peak Shift and Electron Transfer Events using DFT and EC-SERS

In this section, an open-shell vibrational mode calculation using DFT (**Table 2.1**) and electrochemical SERS (EC-SERS) measurements (**Figure 2.4**) were conducted to further confirm the correlation between the peak shift in the Raman spectrum and the electron transfer process. To save computational cost, only the fullerene structure was optimized in the vibrational mode calculations. As shown in **Table 2.1**, calculations using the B3LYP functional demonstrates that the $A_g(2)$ mode of the C_{60} cation shifts to higher frequency by 5.6 cm^{-1}, and it shifts to lower frequency by 7.6 cm^{-1} and 17.2 cm^{-1} when C_{60} accepts one and two electrons, respectively. Calculations with the exchange-correlation functional BP86 show similar results.

Table 2.1. DFT Vibrational Frequency Calculation of Different C_{60} Species

Species	**Raman mode (cm^{-1})**		**Peak shift (cm^{-1})**	
	B3LYP	BP86	B3LYP	BP86
C_{60}^{+}	1501.4	-	+5.6	-
C_{60}	1495.8	1468.7	0	0
C_{60}^{-}	1488.2	1461.2	-7.6	-6.5
C_{60}^{2-}	1478.6	1452.0	-17.2	-16.7

In EC-SERS experiments, cyclic voltammetry of PCBM was first examined under oxygen-free conditions in the potential range -2.4 V to 1.4 V *vs*. Fc/Fc^{+} (**Figure 2.4a**, **Figure 2.9**). In the negative potential region, there are three reversible redox peaks, indicating one-electron, two-electron, and three-electron reduction products, respectively.[138-139] An irreversible oxidation peak appears from 0.9 V to 1.2 V *vs*. Fc/Fc^{+} (Supporting Information section, **Figure 2.9**), showing that PCBM is hard to oxidize into cations.[138-140] Then EC-SERS measurements for PCBM were performed in a custom-designed electrochemical cell with a gold film-over-nanospheres (FON) plasmonic substrate as the working electrode. A selected series of PCBM SER spectra under different applied potentials are shown in **Figure 2.4b**. The onset of the peak shift of the $A_g(2)$

mode appears at around -0.8 V *vs*. Fc/Fc$^+$, right before the first reduction potential. As more negative potentials were applied, larger peak shifts towards the lower frequency were observed, consistent with the theoretical calculations and CW pump-probe SERS experiment results. Note that under around -1.5 V *vs*. Fc/Fc$^+$, the PCBM SER signal starts to decrease due to its desorption from the electrode surface. **Figure 2.4c** shows more clearly the threshold at -0.8 V *vs*. Fc/Fc$^+$ and the increasing peak shift of the $A_g(2)$ Raman mode with applied potential. The vibrational mode calculations and EC-SERS experiments demonstrate that as more PCBM molecules accept electrons there is a larger Raman peak shift of the pentagonal pinch mode.

2.3.5 Excitation Wavelength Dependence of the Electron Transfer Process

To further understand the mechanism of plasmon-driven hot electron transfer between gold nanoparticles and PCBM, the excitation photon energy dependence of this electron transfer process was explored with wavelength-scanned CW pump-probe SERS. The CW pump laser was tuned from 426 nm to 620 nm and the probe wavelength was held at 785 nm. Each PCBM SER spectrum

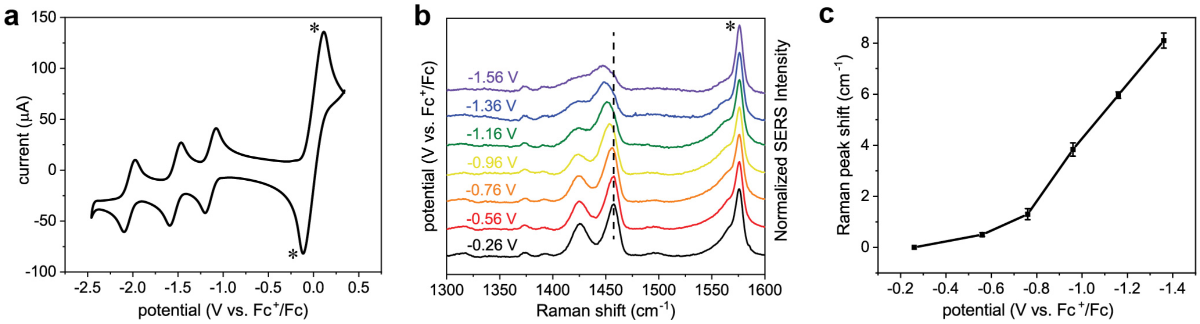

Figure 2.4. (**a**) Cyclic voltammetry of 2 mmol/L PCBM in *o*-dichlorobenzene/acetonitrile (5:1 by volume) with 0.1 mol/L $TBAPF_6$ at 100 mV/s under N_2 environment. 5 mmol/L Ferrocene (Fc) was added as an internal standard, shown as * in the CV. (**b**) Zoomed-in SER spectra of PCBM around the pentagonal pinch mode under different potentials. * is the normal Raman peak of *o*-dichlorobenzene. The black dashed line is at 1458 cm^{-1} to guide the eye. (**c**) Relationship between the frequency shift of the PCBM pentagonal pinch mode and the applied potential.

was examined to have relatively strong Raman signals without photodegradation features to decrease the fitting uncertainty. The pump laser power at the sample was 200 μW under each wavelength. The action spectrum of this plasmon-driven electron transfer reaction is shown in **Figure 2.5a**, where the $A_g(2)$ Raman peak shift is plotted against the wavelength of the pump laser. The extinction spectrum of the gold nanoparticles is overlaid for easy comparison. Previous literature demonstrates that 2.38 eV (520 nm) is the interband transition (5d to 6sp) energy threshold of gold.[141] In the region where the pump wavelength is longer than 520 nm, the gold d band edge can be broadened into this region and contribute to the hot electron transfer, but most of the hot electrons transferred to PCBM originate from the sp intraband transitions in the gold nanoparticles (**Figure 2.5b**). The action spectrum in this region follows the localized surface plasmon resonance of gold nanoparticle monomer, demonstrating the plasmonic enhancement effect on this electron transfer process. At a pump wavelength around 520 nm, a significant increase in the $A_g(2)$ Raman mode frequency shift appears in the action spectrum, indicating the significant contribution from interband transitions (d band to sp band) in addition to intraband transitions. When the excitation photon energy is higher than 2.38 eV, since the d band covers a much narrower energy range than the diffuse sp band (**Figure 2.5b**), most of the hot electrons generated from interband transition are expected to have minimal energy above the Fermi level E_F with simultaneous production of energetic holes deep in the d band.[122] This asymmetric carrier distribution in the gold nanoparticles usually favors hot hole transfer, but in the action spectrum (**Figure 2.5a**) the Raman peak shift still increases with higher excitation energy, indicating hot electron transfer still dominates the process (**Figure 2.5c**). This can be explained by the relative position of the band structure of gold with respect to the HOMO and LUMO of PCBM. According to the electronic structure calculation (**Figure 2.3**), the LUMO of PCBM is only about 0.2 eV above the Fermi level, so PCBM can still accept electrons generated from the interband transition. Meanwhile, the highest gold d band is at -3.80 eV, which is still above the HOMO of PCBM (-4.61 eV), making hole transfer unfavorable. Furthermore, as shown in previous literature and electrochemical experiments, PCBM is hard to be oxidized,[138] indicating that even if some of the hot holes can be transferred to the HOMO of PCBM, they cannot be stabilized and would immediately transfer back to the gold nanoparticles.

In addition to the contribution of intraband and interband transitions, the mechanism of plasmon-driven electron transfer can also be discussed based on the energy dependence of the action spectrum (**Figure 2.5a**). The two main proposed mechanisms in the literature are indirect electron transfer and direct electron transfer. For indirect electron transfer, the hot electrons are first generated either from plasmon decay or interband transition, and then incoherently transfer to the LUMO of nearby molecules. As a result, the probability of electron transfer heavily depends on the transition density within the band structure of the gold nanoparticles. This generally increases with higher excitation energy but it locally peaks at the LSPR energy. Direct electron transfer requires the formation of hybridized surface states between the nanoparticles and the adsorbed molecules, such that the anions are produced by photoexcitation of these states. This suggests that direct hot electron transfer should have a peaked dependence on excitation energy, with the peak occurring at the energy of the hybridized state. In **Figure 2.5a**, the general trend in the action spectrum is that the plasmon-driven hot electron probability increases with the excitation energy. In the energy region of the localized surface plasmon resonance, the action spectrum follows the monomer plasmon resonance of the gold nanoparticles. We also did not observe any other peaks indicating the existence of hybrid states. This implies that the indirect electron transfer pathway dominates the electron transfer process between gold nanoparticles and PCBM.

2.3.6 Stokes and Anti-Stokes SERS for Nanoscale Thermometry

Another advantage of SERS is that the temperature of the molecular vibrational mode can be directly derived from the ratio ρ of anti-Stokes (aS) and Stokes (S) SER intensity.[142] The contribution to ρ is governed by eq 3 based on the Boltzmann distribution[143]:

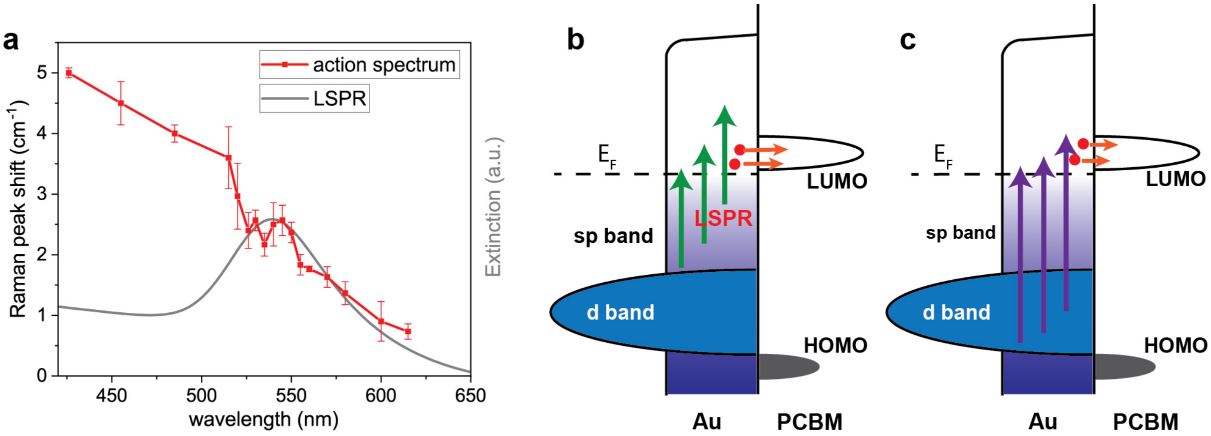

Figure 2.5. (**a**) Pump wavelength dependence of the plasmon-driven electron transfer process. The gray curve is the extinction spectrum of gold nanoparticle colloid with PCBM. The pump and probe laser power were kept at 200 μW and 300 μW, respectively. Simplified energy diagrams for hot electron transfer with pump photon energy (**b**) below and (**c**) above the interband transition threshold.

$$\rho = \frac{I_{AS}}{I_S} = \left(\frac{\omega_L+\omega_{vib}}{\omega_L-\omega_{vib}}\right)^4 \exp\left(-\frac{\hbar\omega_{vib}}{k_B T_{eff}}\right) \quad (3)$$

Here ω_L is the laser frequency, ω_{vib} represents the frequency of the vibrational mode, k_B denotes the Boltzmann constant, and T_{eff} is the effective temperature of the vibrational mode. The pre-exponential factor $\left(\frac{\omega_L+\omega_{vib}}{\omega_L-\omega_{vib}}\right)^4$ describes the intrinsic wavelength dependence of Raman scattering.

We measured the anti-Stokes and Stokes SER spectra of PCBM under different pump wavelength and power. The samples were the same gold nanoparticle aggregates with PCBM molecules used in CW pump-probe SERS experiments. **Figure 2.6a** shows a typical full PCBM SER spectrum. Note that the anti-Stokes side is enlarged 40 times for a clearer view. The effective vibrational temperatures of the PCBM pentagonal pinch mode under different conditions were calculated using eq 2.3. **Figure 2.6b** shows the calculated vibrational temperature under different conditions. Increasing pump laser power does not have a significant effect on the vibrational temperature, which was in the range of 300-350 K. It demonstrates that there is no significant photothermal effect during this electron transfer process.

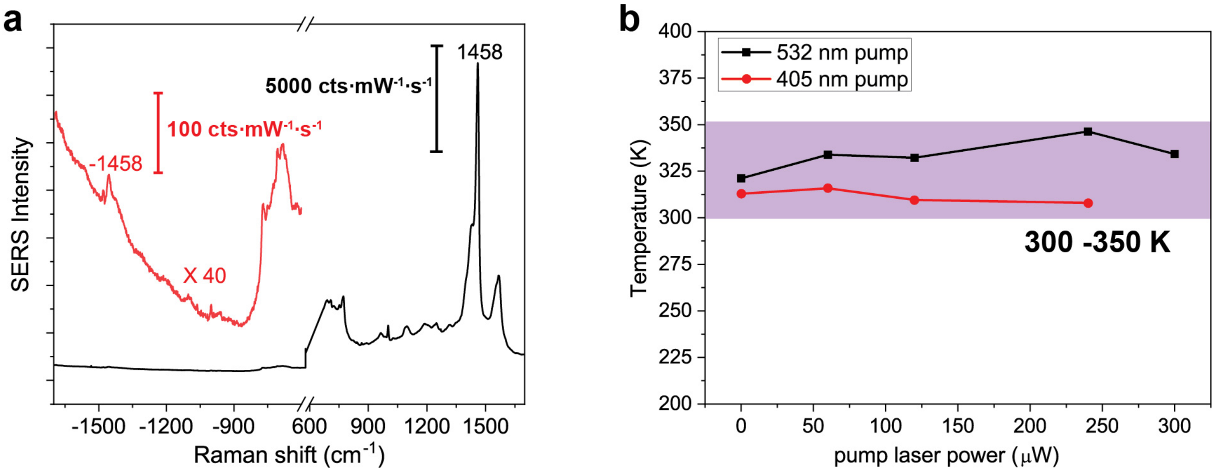

Figure 2.6. (**a**) Stokes and anti-stokes side of PCBM SER spectrum with 750 μW 785 nm laser on the sample. The anti-stokes side is enlarged 40 times for a clearer view. (**b**) The effective vibrational temperature of the pentagonal pinch mode under different pump laser power (up to 300 μW) and wavelength. The power of 785 nm probe laser was kept at 750 μW.

2.4 Experimental Methods

2.4.1 AuNP/PCBM Composite Preparation

The gold nanoparticle aggregates with PCBM molecules were prepared according to a previously published procedure with slight modifications.[144] The 60 nm gold nanoparticle colloids (STA Technologies Inc., Albuquerque, NM) were first centrifuged and redispersed into dimethylformamide (DMF). Then 2 mL gold nanoparticle colloids were aggregated upon adding 40 μL 1 mmol/L PCBM DMF solution. 200 μL Polyvinylpyrrolidone (PVP) DMF solution (10% by weight) was added to stabilize the aggregated gold nanoparticles.

Microscope glass coverslips (VMR International, No.1, 25 mm in diameter) were treated with piranha (3:1 H_2SO_4:30%H_2O_2) for about 30 min followed by thorough rinsing with Milli-Q water (18.2 $M\Omega\cdot cm^{-1}$). The aggregated colloids functionalized with PCBM in nanogaps were drop cast and dried on the pre-cleaned glass coverslip.

2.4.2 CW Pump Probe SERS Experiments

The sample was irradiated with two spatially overlapped, collinear laser beams in an epi-illumination microscope setup (Nikon Ti-U) through a Nikon microscope 40× objective (NA = 0.60). The two laser beams were 532 nm CW laser (Spectra-Physics, Santa Clara, CA) and 785 nm CW laser (Renishaw Inc.). The 532 nm laser worked as a pump laser to excite plasmon within gold nanoparticles, and the 785 nm laser was used to generate SER signals. SER signals were collected by the PIXIS 400 CCD camera mounted on a Spectra Pro 2500i spectrometer (Princeton Instruments, Trenton, NJ) with a 600 gr/mm grating (Blaze wavelength = 750 nm).

In pump wavelength dependence experiments, instead of using the 532 nm CW laser, a tunable CW laser system (M squared, Glasgow, UK) was used as the pump. The laser system covers a broad spectral range (305 – 1000 nm) with super fine spectral resolution (0.0001 nm). The pump laser power was kept at 200 μW. At each pump wavelength, the pump laser power was examined before and after the microscope for the calibration of transmission efficiency at different wavelength to ensure the pump laser power was the same at the sample.

2.4.3 EC-SERS Experiments

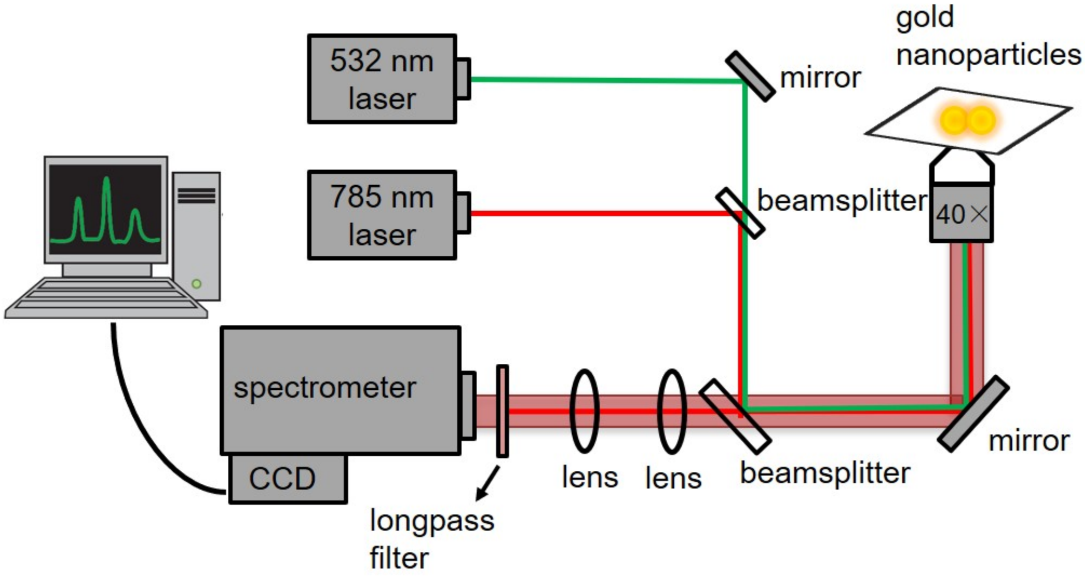

Figure 2.7. CW pump-probe SERS setup. In excitation wavelength dependence experiments, the pump laser is switched to a tunable laser system.

The electrochemical cyclic voltammetry (CV) of PCBM (2 mmol/L) was conducted on a potentiostat (CH Instruments Inc.) in a 0.1 mol/L tetrabutylammonium hexafluorophosphate (Bu_4NPF_6) *o*-dichlorobenzene/acetonitrile (5:1 by volume) solution, with 5 mM ferrocene (Fc) as the internal standard. The scan rate was 100 mV/s. The Au film-over-nanospheres (FON) plasmonic substrate was fabricated as working electrode.[16] The Au FON substrate was rinsed in PCBM solution for about 5 min and assembled in a self-designed electrochemical cell filled with 0.1 mol/L Bu_4NPF_6 *o*-dichlorobenzene/acetonitrile (5:1) solution. Pt wire and Ag wire were counter electrode and reference electrode, respectively. The potential was controlled by an EC301 potentiostat (Stanford Research System, Sunnyvale, CA). A 633 nm HeNe laser (Voltex, Inc.) was used to detect PCBM SER signals on Au FON substrate under different potentials.

2.4.4 Theoretical Calculations

Electronic structure calculations for PCBM adsorbed on a four-layer gold slab were performed with DFT using the exchange-correlation functional PBE within the program SIESTA (Spanish Initiative for Electronic Simulations with Thousands of Atoms, version 4.1-b4).[145] In the structure optimization we froze the coordinates of the Au slab. The basis set DZP was employed for all atoms but Au, which was modeled with SZP. The energy cut-off for the atomic basis set generation is the standard value, 20 Ry, whereas the plane-wave mesh cut-off value is 300 Ry, which makes "eggbox" effects negligible. The density-matrix tolerance for each self-consistent calculation was 10^{-5}. The force tolerance for the structural relaxation was 0.05 eV/Å. To generate the projected density of states (PDOS) plot we used a smearing factor of 0.05 eV and the DZP basis set for all atoms.

Vibrational mode and Raman calculations for fullerene and different ion species were performed using the NWChem program.[146] The BP86 exchange-correlation functional and the TZVP basis set were used. The B3LYP functional with the 6-311G* basis set were also applied for comparison.

2.5 Chapter Conclusion

In conclusion, the plasmon-driven hot electron transfer reaction between gold nanoparticles and PCBM was systematically studied using CW pump-probe SERS. The action spectrum of the hot electron transfer shows that both intraband and interband transitions in the gold nanoparticles generate hot electrons, which then reduces PCBM into anions, predominantly through the indirect electron transfer pathway. Furthermore, the anti-Stokes/Stokes Raman intensity ratio of PCBM under different conditions shows that photothermal effect is not significant in this plasmon-driven electron transfer reaction. DFT calculations reveal the detailed energy diagram of the system, especially the relative energy level position of the plasmonic metal band structure and molecular orbitals of PCBM, supporting the mechanism concluded in the experiments.

These findings show that CW pump-probe SERS in combination with DFT are powerful tools for studying the mechanism of plasmon-driven chemical reactions. More importantly, they also provide critical information on the design rules of plasmon-driven chemistry: the band structure of the plasmonic nanostructures needs to be well engineered with respect to the molecular orbitals of the reactants to control the reaction pathways. For example, if the LUMO of the molecule is close to the Fermi level and the HOMO is below the d band of the metal (like the gold nanoparticle and PCBM case), the hot hole transfer pathway is suppressed but hot electron transfer can still happen if the excitation photon energy is above the interband transition threshold. Additionally, the excitation photon energy can be rationally tuned not only to maximize the reaction efficiency, but also to selectively excite intraband or interband transitions in the plasmonic nanostructures, which can lead to different reaction pathways. All these rules can be applied in the future design of plasmon-driven chemical reactions, which can further improve the yield and selectivity of photochemistry on the nanoscale.

2.6 Supporting Information

2.6.1 Degradation of PCBM under High Pump Laser Power

When the pump laser power is too high, PCBM molecules in the gold nanoparticles “hot spots” can go through photodegradation. The SER spectrum of photodamaged PCBM has the feature of significantly decreased Raman signal, large peak broadening and the rising of new peaks. **Figure 2.8** shows a typical PCBM SER spectrum when pump laser is too high.

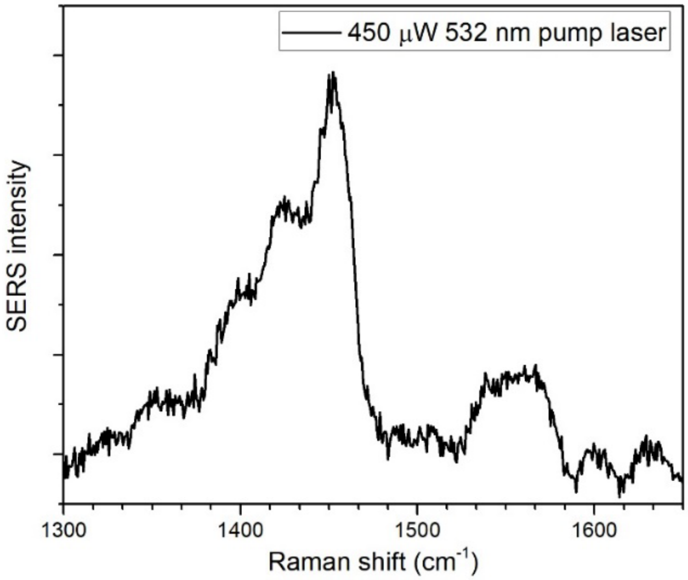

Figure 2.8. Photodegraded PCBM SER spectrum under 450 μW 532 nm pump laser.

2.6.2 The Derivation of the Kinetic Model for Pump Power Experiment

Considering the elementary electron transfer reaction:

$$\mathrm{PCBM} + e^{-} \underset{k_{-1}}{\overset{k_1}{\rightleftharpoons}} \mathrm{PCBM}^{-}$$

The concentration change rate of $PCBM^{-}$ can be expressed as follows:

$$\frac{d[PCBM^{-}]}{dt} = k_1[PCBM][e^{-}] - k_{-1}[PCBM^{-}] \quad (1)$$

Here we assume the total PCBM concentration in gold nanoparticle hot spots is constant: $[PCBM]+[PCBM^{-}]=[PCBM]_0$. The concentration of photogenerated electrons e^{-} is proportional to the photon flux, namely the pump laser intensity I_L:

$$[e^{-}] \propto n\hbar v \propto I_L$$

n is the number of photons. Based on the steady state approximation $\frac{d[PCBM^{-}]}{dt}=0$, eq 1 can be rewritten as follows with the ratio θ:

$$\theta = \frac{[PCBM^{-}]}{[PCBM]_0} = \frac{\frac{k_1}{k_{-1}}[e^{-}]}{1+\frac{k_1}{k_{-1}}[e^{-}]} = \frac{K'_{eq}I_L}{1+K'_{eq}I_L}$$

2.6.3 PCBM Full Cyclic Voltammetry (CV)

Figure 2.9 shows the full CV of PCBM in the range of -2.4 V to 1.4 V *vs*. Fc/Fc$^+$. At the positive potential side there is an irreversible oxidation peak, indicating that the PCBM cation is not very stable.

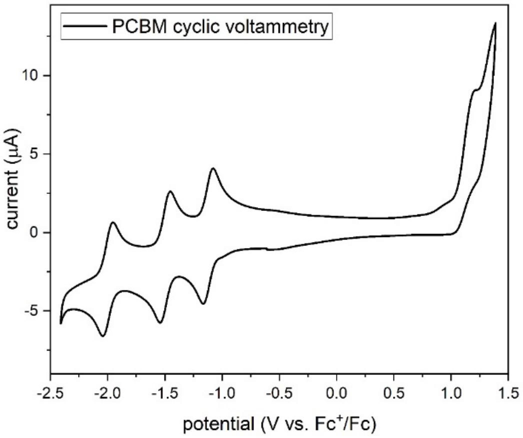

Figure 2.9. Full cyclic voltammetry of 2 mmol/L PCBM in *o*-dichlorobenzene/acetonitrile (5:1 by volume) with 0.1mol/L TBAPF$_6$ at 100 mV/s.

2.6.4 DFT Simulations of the PCBM-Au$_{20}$ System

Electronic structure calculations for PCBM interacting with a Au$_{20}$ cluster were performed using the Amsterdam Density Functional (ADF) program.[147] The basis set TZP and exchange-correlation functional BP86 were used. The zero-order regular approximation was used to include the relativistic effect for the calculations. Lowest 30 allowed excitation transitions were calculated. The lowest singlet transition at 1.04 eV, HOMO to LUMO, is plotted in **Figure 2.10**, showing clear charge-transfer character (from gold to PCBM).

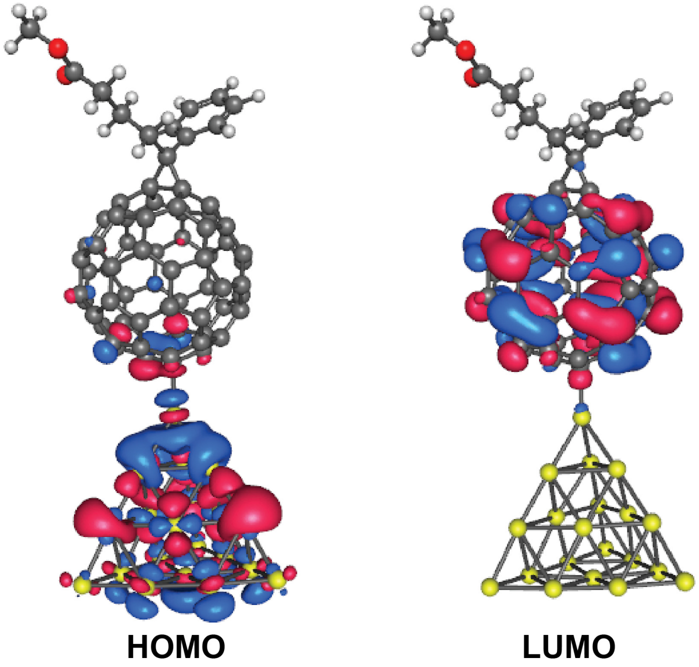

Figure 2.10. DFT calculation of PCBM with Au_{20} cluster. The HOMO-LUMO transition shows clear charge-transfer character.

Chapter 3: Reduced Spectral Diffusion of Single Quantum Dot Emission with Plasmonic Nanoshell Structure

3.1 Chapter Summary

The instability of single quantum dot emission (blinking and spectral diffusion) has been a major blockade for their application in the quantum optics. In this chapter, a core/spacer/shell hybrid structure of QD/silica/gold has been fabricated to reduce the spectral diffusion behavior of the single QD core at room temperature. The hybrid structure was synthesized with a layer-by-layer colloidal shelling method. The typical single particle size is about 50 nm and can be tuned by the thickness of the SiO_2 spacer layer. The band-edge emission of the core quantum dot was tuned by multilayer CdS shelling to overlap with the plasmonic mode of the gold nanoshell.

Real-time series of photoluminescence (PL) spectra of three kinds of single particles, QD, QD/silica, and QD/silica/gold, were collected at room temperature to examine the spectral diffusion behavior. From the comparison a clear reduction in spectral diffusion was observed. By measuring the emission lifetime with a time-correlated single photon counting (TCSPC) method, we propose that the spectral diffusion reduction is caused by Purcell enhancement from the plasmonic nanoshell structure to the QD exciton radiative recombination rate which suppresses the charging effect on the QD surface. These experiments demonstrated that plasmon-exciton coupling on the single particle level can be an effective strategy to improve the emission stability of semiconductor nanocrystals, which can be utilized in the application of quantum optics.

3.2 Introduction

Colloidal semiconductor quantum dots (QD) have been widely applied in various optical devices due to their tunable electronic structures and photostability, such as light emitting diodes (LED),[148-149] photovoltaics,[150-151] lasers,[152] etc. They have also been proposed to be promising candidates for scalable and color-tunable single photon emitters in quantum optics.[153-155] However, a single quantum dot often shows unstable emission, which limits their application as high-quality single photon emitters. The common emission instability phenomena are emission intermittency (also known as "blinking") and spectral diffusion (SD).[156-158]

Spectral diffusion is the stochastic dynamic shifting of the emitted photon energy. It is generally accepted that electric charging causes the spectral diffusion behavior of single nanocrystal emitter. Empedocles et al. studied the spectral diffusion of single CdSe/ZnS quantum dot emission under an external modulating electric field with electro-optical spectroscopic methods.[159] They found correlation between spectral diffusion and fluctuations of the electric field in the local environment of the emitter. Although the exact physical picture of the surface charge affecting the QD spectral line is still under debate due to the complicated interface between the crystal surface atom and the organic ligands of the QD, local environment engineering, like surface passivation by coating with multiple semiconductor layers[160] or changing the surface ligand[161], has been a popular strategy to achieve brighter and more stable emission.

Coupling plasmonic nanostructures with semiconductor nanocrystal emitters like CdSe QDs is also a widely used strategy to improve the emission properties of the QDs by modifying the local environment of the emitter. The plasmonic nanostructures can not only significantly concentrate the light in the local environment of QDs to increase light absorption, but also increase the radiative decay rate of the emitter through the Purcell effect (more details can be found in section 1.4.2). Recently people also found that plasmon-exciton coupling can also lead to reduced PL intermittency of single QD because the QD enhanced emission pathway by Purcell effect of the plasmonic nanostructure compete over the nonradiative Auger recombination pathways.[63] But so far there is no report about the effect of plasmon excitation on the spectral diffusion behavior of single QD.

Here in this chapter, a single CdSe QD is coupled with plasmonic nanoshell structure spaced with a silica layer and its spectral diffusion behavior is studied under room temperature. Through the consecutive PL spectra acquirements and time-resolved PL experiments, we proved that the spectral diffusion of the single QD core is reduced by the protection of silica layer and the Purcell effect of the plasmonic shell.

3.3 Results and Discussion

3.3.1 Synthesis of QD/silica/gold core/spacer/shell Particles

The gold shelled QD hybrid structure was synthesized following a colloidal layer-by-layer shelling procedure with some modifications (more details can be found in the Experiment Method section 3.4.1).[63, 162] As plotted in **Figure 3.1**, first CdSe/3CdS core/shell quantum dots were synthesized by a hot injection method.[163] After preparing the QD as the core, the QDs were encapsulated with a layer of silica by the "water-in-oil" reverse-emulsion method.[164] The QDs were transferred from hexane solution to aqueous phase and the original carboxylic acid ligands were exchanged by the silica precursor tetraethyl orthosilicate (TEOS). Then the mixture was stirred for 24 h. TEOS went through self-polymerization reaction into SiO_2 under basic conditions and grows a silica shell around the QDs. The silica shell thickness can be controlled by the added volume of TEOS, as demonstrated in **Figure 3.2**: Less initial TEOS leads to thinner silica shell.

From **Figure 3.1b** and **Figure 3.2** we can also see that most of the QD/silica core/shell nanoparticles have only one QD core at the center.

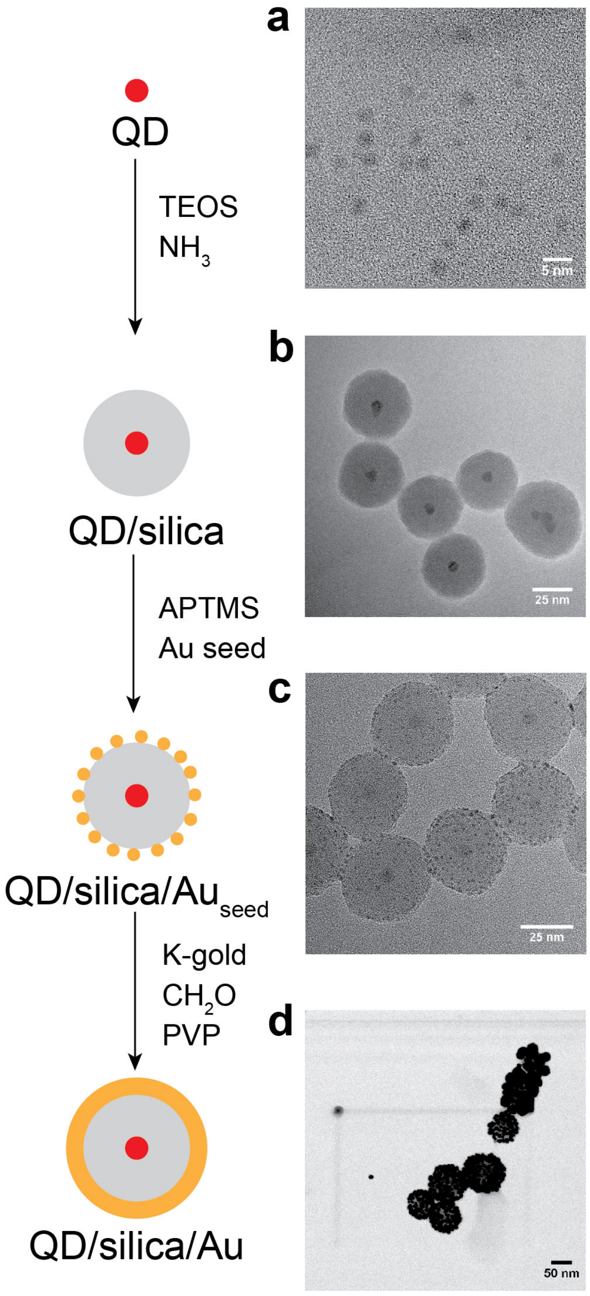

Figure 3.1. The detailed synthesis scheme of QD/silica/Au core/spacer/shell nanoparticles and the TEM images of each step: (**a**) CdSe/3CdS QDs; (**b**) QD/silica; (**c**) QD/silica/Au$_{\text{seed}}$; (**d**) QD/silica/Au.

Then the gold shell was coated on the silica surface with a seed-mediated growth method. Au seeds in aqueous solution were first synthesized by reducing the $HAuCl_4$ solution with freshly prepared $NaBH_4$ solution. By treating the QD/silica particles with (3-Aminopropyl) trimethyloxysilane (APTMS) at 65 ºC for 4 h, APTMS were attached to the surface of QD/silica particles and the amine group in APTMS binds to Au seeds when Au seeds were mixed with the QD/silica particle solution. We performed 5 cycles of centrifugation and Au seed mixing to maximize the Au seed coverage on the silica surface (shown in **Figure 3.1c**). The final step is to add QD/silica into the Au(III) solution. Gold nanoparticles were grown with the Au seeds as the nucleation center using formaldehyde as the reducing agent. Finally, the gold nanoparticles merged into a continuous gold nanoshell around the silica surface (**Figure 3.1d**). During the final step, polyvinylpyrrolidone (PVP) was added in the mixture to control the growth rate of the gold shell.

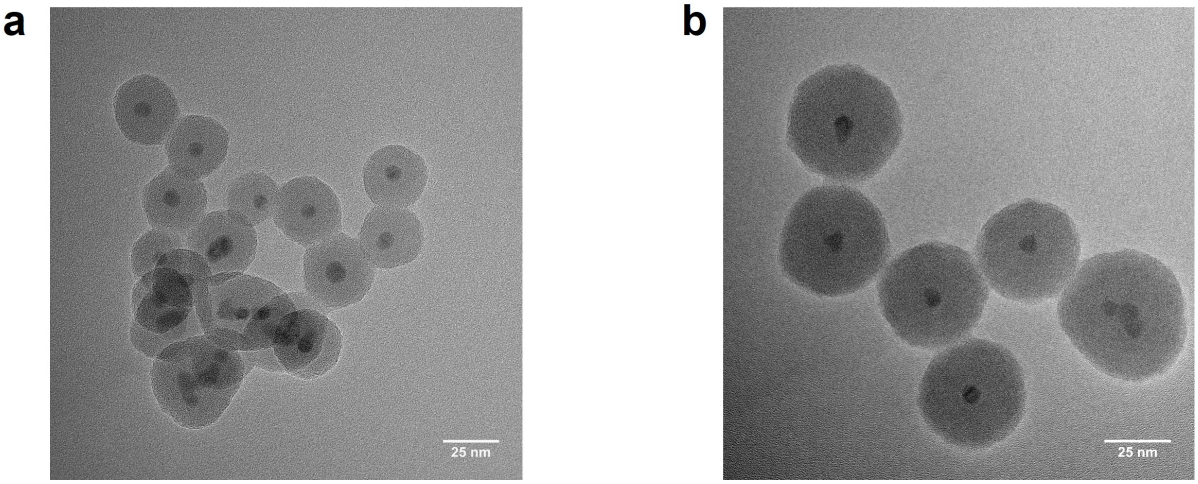

Figure 3.2. The TEM images of QD/silica particles with different added TEOS volume at the beginning of the silica shell growth: (**a**) 60 μL; (**b**) 300 μL. The averaged particle sizes are 28 nm (**a**) and 42 nm (**b**), respectively.

Without PVP the gold nanoparticles would grow too fast to form the shell structures (details in the Supporting Information section 3.6).

3.3.2 UV-vis and PL Characterization

The absorption and PL spectra of QD in hexane solution and QD/silica/Au in EtOH solution are presented in **Figure 3.3**. In the absorption spectra of QD/silica/Au EtOH solution (**Figure 3.3a**), the relatively broad feature is the plasmon resonance of the gold shell, which overlaps with the QD band-edge absorption. The solution PL spectra of QD and QD/silica/Au demonstrate that the silica and gold coating don't affect the PL peak position of QD core.

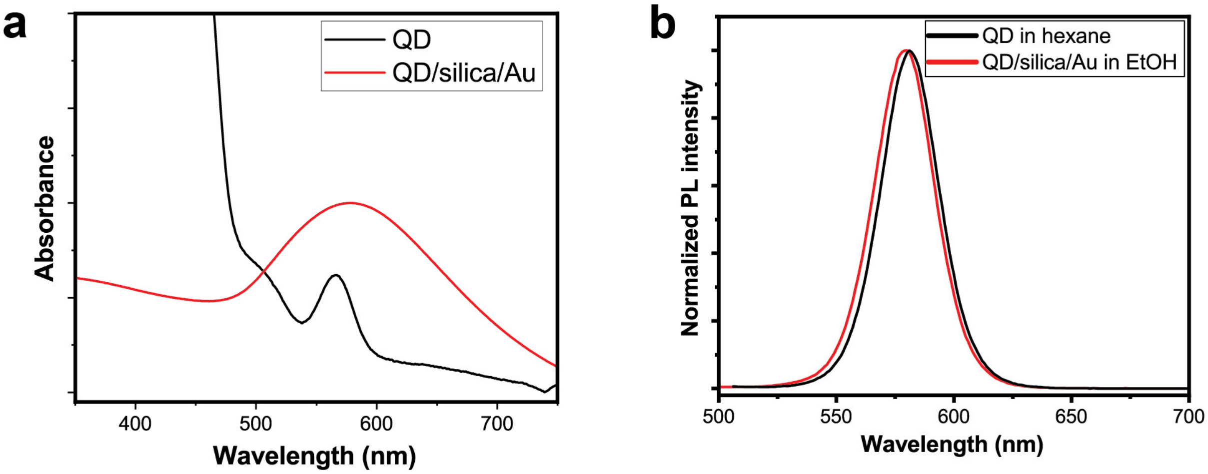

Figure 3.3. The solution-phase absorption (**a**) and PL (**b**) spectra of QD (black curves) and QD/silica/Au (red curves).

3.3.3 Single Particle Characterization on the Microscope

The prepared particle solution was diluted and drop cast on the glass coverslip for single particle measurements on a homebuilt microscope under room temperature. The glass coverslip was first cleaned with ammonia and hydrogen peroxide to make the surface more hydrophilic, which helps the particles disperse more homogeneously on the surface (details in the Supporting Information section 3.6).

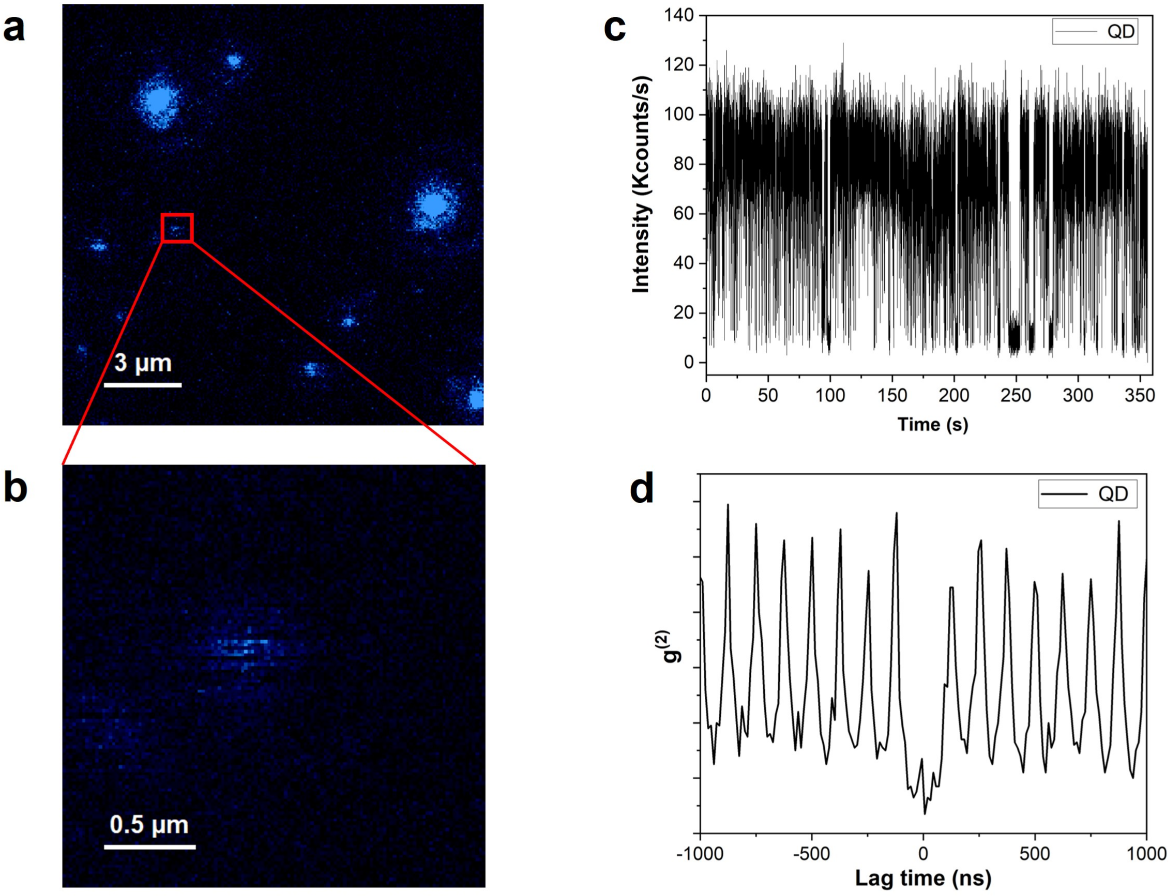

Figure 3.4. The single particle measurements of CdSe/3CdS QDs under room temperature. (**a**) The PL scan image of QDs in a 15*15 μm^2 region. (**b**) A finer PL scan of the red box region in (**a**). (**c**) The PL intensity time trace of single QD. (**d**) The second-order correlation function $g^{(2)}$ measurement of the same QD in (**c**). The laser power is 150 nW.

We first need to examine whether we are collecting the PL signal on the single particle level. **Figure 3.4** shows the PL scan images, PL time traces and the second-order correlation $g^{(2)}$ measurements for a single QD. In **Figure 3.4a**, the bright spot which is about 2 µm in size shows small aggregates of QDs. Only the dim spots which have the size around 0.5 µm (close to the diffraction limit) are single QDs (**Figure 3.4b**). **Figure 3.4c** shows the clear on/off blinking behavior of a single QD, and the corresponding $g^{(2)}$ plot on the same QD (**Figure 3.4d**) shows clear anti-bunching behavior, in which $g^{(2)}$ at lag time t=0 is close to zero. The emission intermittency and $g^{(2)}$ plot are clear evidences proving single QD was detected. Similar measurements were also done for QD/silica and QD/silica/Au particles

.

3.3.4 Reduced Blinking of QD/silica/Au Particles

As already shown in **Figure 3.4c**, single QD emission oscillates randomly between on and off states, which is a common phenomenon showing the instability of QD emission on single particle level. This blinking behavior still exists after silica coating (Supporting Information section 3.6),

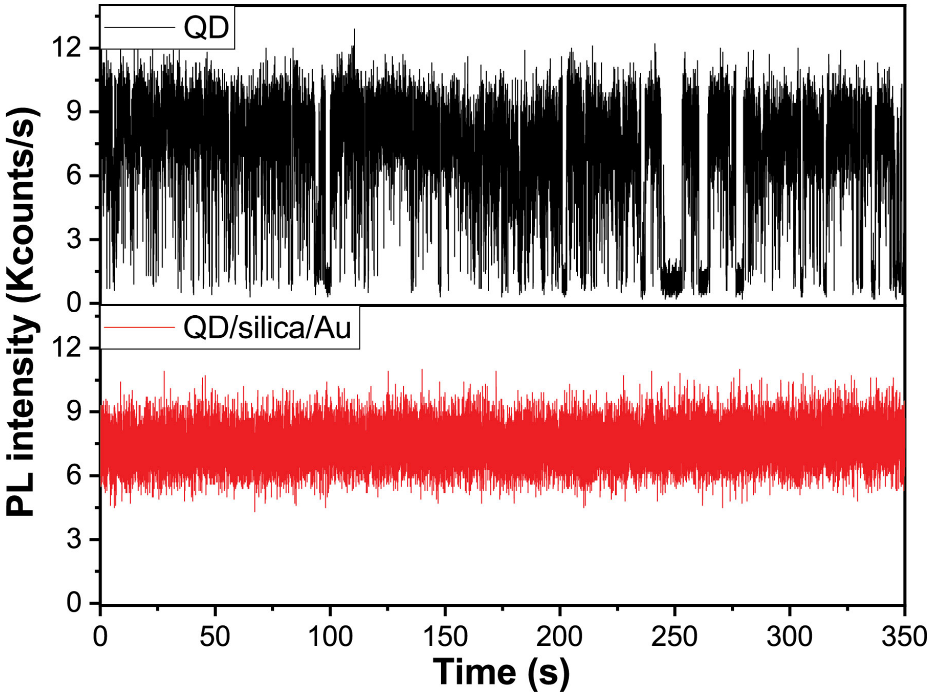

Figure 3.5. The Blinking behavior comparison between single QD (top trace, black) and single QD/silica/Au (bottom trace, red). The bin time for each trace is 10 ms.

but the QD/silica/Au particle significantly suppressed the emission intermittency, demonstrated in **Figure 3.5**.

3.3.5 The PL Spectra Time Traces for Monitoring Spectral Diffusion

The emission from QD and QD/silica/Au particles were directed into the spectrometer to collect real-time PL spectra time traces (**Figure 3.6**). 10 min consecutive acquisition was performed on each particle, and the acquisition time for each frame is 2 seconds to achieve the balance between the good signal-to-noise ratio (SNR) and fast data collection speed to monitor the spectral dynamics. As **Figure 3.6** shows, the PL peak of single QD clearly shifted randomly around the center emission energy (**Figure 3.6a**), while the PL spectra of single QD/silica/Au particle are much more stable in the frequency domain (**Figure 3.6b**).

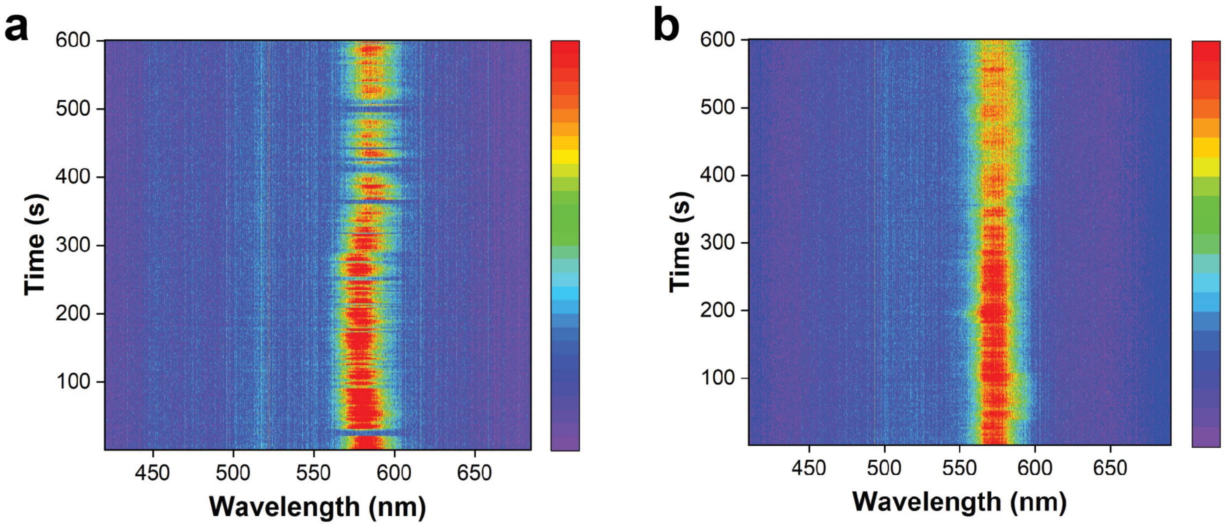

Figure 3.6. The PL spectra time traces of single QD (**a**) and QD/silica/Au particle (**b**). The acquisition time for each frame is 2 s and the laser power is 150 nW.

To quantitatively analyze the spectral diffusion data, each frame of the PL spectra traces (like **Figure 3.6**) was fitted with single Gaussian peak function and the real-time peak shifts relative to

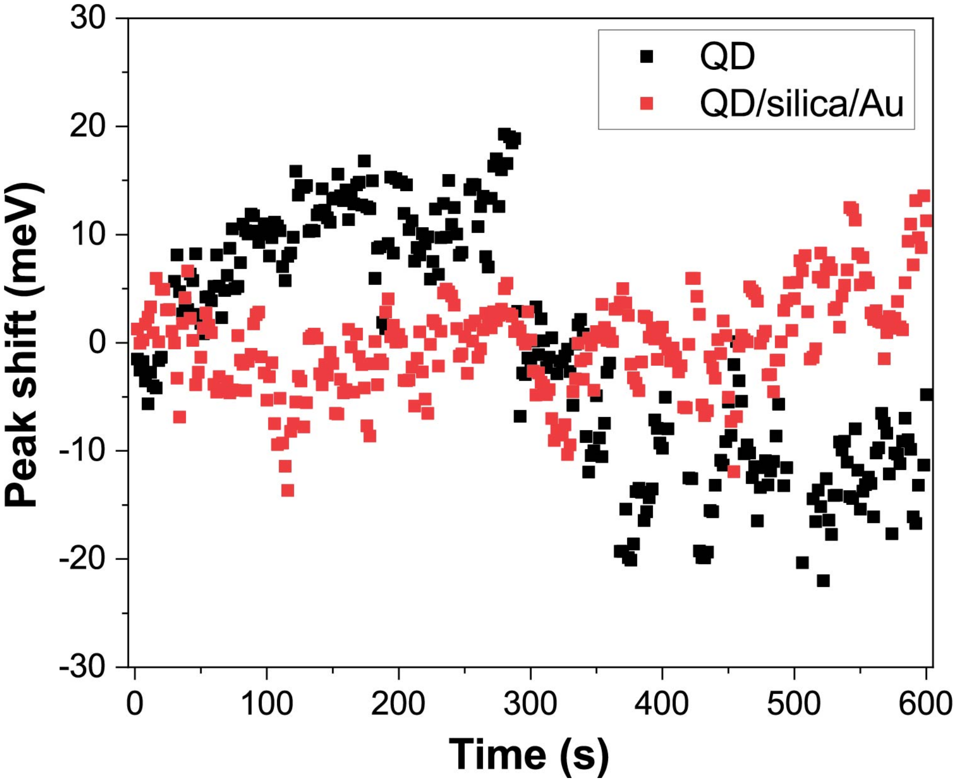

Figure 3.7. PL peaks shift time traces for single QD (black) and QD/silica/Au (red).

the center peak position were recorded for comparison (**Figure 3.7**). One thing needs to be noticed is since the single QD blinks during the acquisition, those frames in which QD were in the non-emissive state were eliminated by examining the SNR and the standard deviation of the fitting. In **Figure 3.7** we can clearly observe that the amplitude of QD random PL peak shift is larger than that QD/silica/Au particle.

To check the reliability of the observed spectral diffusion behavior, and more importantly, to explore the mechanism of SD suppression, similar PL time traces were collected on several different nanoparticles of each category, QD, QD/silica and QD/silica/Au, for comparison. After extracting out the real-time peak shift data by single Gaussian peak function fitting, averaged peak

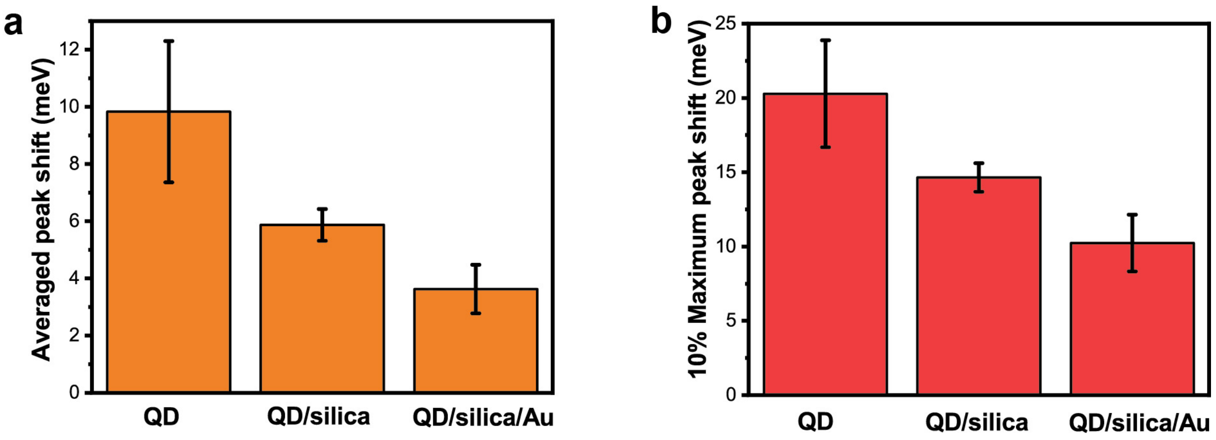

Figure 3.8. Comparison of the averaged peak shift per frame (**a**) and 10% maximum amplitude interval of the peak shift per frame (**b**) between different species of particles: QD, QD/silica, QD/silica/Au. The acquisition time of each PL spectra frame is 2 s.

shift per frame and the 10% maximum amplitude interval of the peak shift were calculated (**Figure 3.8**). The error bars were calculated over at least three particles.

As **Figure 3.8** shows, both the average peak shift and 10% maximum peak shift amplitude decrease in the order of QD, QD/silica and QD/silica/Au, clearly demonstrating suppression of spectral diffusion of a single QD by silica and gold shelling. Here we propose the mechanism of SD suppression is a cooperative effect by both silica and gold shell. The silica shell replacing the organic long-chain ligand passivates the surface of the QD to reduce the chances of free charges in the local environment directly affecting the QD. The plasmonic shell, on the other hand, enhances the emission rate of the QD through the Purcell effect to compete with the self-charging rate and other nonradiative decay rates.

3.3.6 Purcell Factor Estimated by Emission Lifetime Measurements

To confirm our assumptions about the contribution of the Purcell effect towards reducing the spectral diffusion of single QD, we measured the emission lifetime of different species of particles

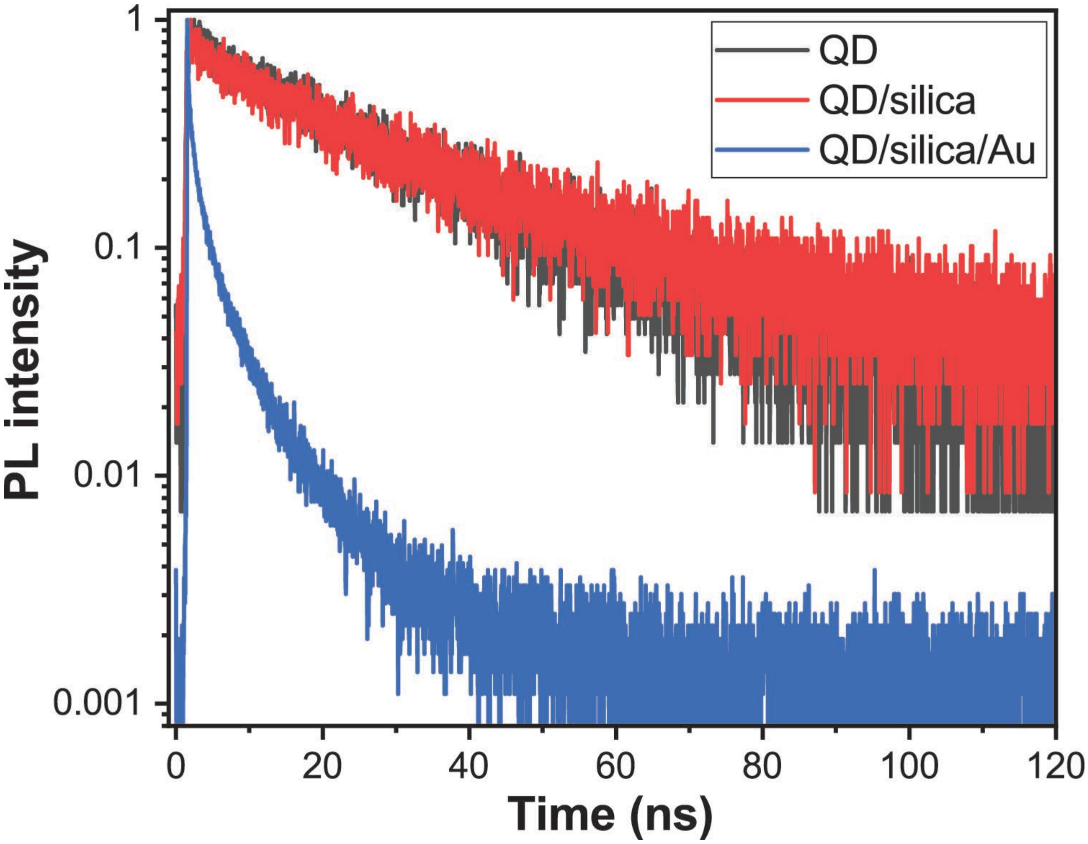

Figure 3.9. The emission lifetime measurements of the three kinds of particles: QD (black), QD/silica (red) and QD/silica/Au (blue).

to quantitatively estimate the Purcell factor of plasmonic nanoshell structure by time-resolved PL spectroscopy.

The time-resolved PL measurements were also conducted on single particles and repeated with at least three particles for each category to ensure reproducibility. **Figure 3.9** shows that the emission lifetimes of QD and QD/silica are similar, and the emission lifetime of the gold coated QD particle is significantly shorter than the other two. The Purcell factor can be roughly estimated by fitting the traces with one exponential decay and comparing the emission lifetime ratio between QD/silica/Au and QD. **Table 3.1** summarizes the single particle spectral diffusion results and the corresponding fitted emission lifetime. The Purcell factor of gold nanoshell structure is estimated to be about 10, which is close to the previous reports.[63]

Table 3.1. The spectral diffusion behavior and emission lifetime of QD, QD/silica and QD/silica/Au

Nanoparticles	Average peak shift (meV)	10% maximum peak shift amplitude (meV)	Emission lifetime τ (ns)
QD	9.8 ± 2.5	20.3 ± 3.6	22.2 ± 0.9
QD/silica	5.9 ± 0.6	14.7 ± 1.0	23.9 ± 2.1
QD/silica/Au	3.6 ± 0.8	10.2 ± 1.9	2.2 ± 0.6

3.4 Experiment Methods

3.4.1 The Synthesis Procedure of QD/silica/Au Hybrid Nanoparticles

1. Synthesis of CdSe/3CdS quantum dots. 2 mL 0.5 M Cd(oleate)$_2$ was mixed with 3 mL ODE in a 50 mL three-neck flask and was degassed under vacuum at 90 ºC for an hour. 1.5 mL 1 M TOPSe, 2 mL oleylamine and 0.4 g Tetradecylphosphonic acid (TDPA) was heated in a vial until the solution turned clear. The mixture was added in the three-neck flask when Cd(oleate)$_2$ ODE solution was heated to 240 ºC under Argon flow. The temperature was maintained at 210 ºC for 5 min. After cooling down to 85 ºC, 30 mL ethanol was added into the flask, and the mixture was centrifuged at 3500 rpm for 10 min. The precipitated pellet was resuspended in hexane and centrifuged at 3000 rpm for 5 min to remove excess TDPA. Then the QD solution was washed twice with ethanol and resuspended in hexane. 1 M TOPSe was prepared by dissolving selenium powder in TOP under stirring in a nitrogen glove box. To shell the CdSe core QDs, 0.1 M $Cd(oleate)_2$ ODE solution was prepared as cadmium precursor. The sulfur precursor was prepared by dissolving 32 mg sulfur into 10 mL ODE (0.1 M sulfur solution) under heating and stirring. 2 mL oleylamine, 4 mL ODE and 1.5 mL 90 μM CdSe core QD solution was added in a 50 mL three-neck flask. After being degassed at 80 °C under vacuum for an hour, the flask was backfilled with Argon flow and the temperature was increased to 230 °C. 0.28 mL 0.1 M $Cd(oleate)_2$ solution was injected dropwise into the flask while heating. After growing for 10 min, 0.28 mL 0.1 M sulfur solution was added, and the temperature was maintained for another 10 min. Then cadmium and sulfur solutions were injected dropwise successively at 10 min intervals with the volume of 0.46 mL, 0.65 mL, 0.87 mL, 1.13 mL. The last injection was done with cadmium precursor solution and reacted for 30 min. The CdSe/CdS QDs were washed with 90 mL ethanol twice and resuspended in hexane.

2. Silica shelling of QD core. The CdSe/3CdS QDs were shelled with silica using a reverse emulsion method. 300 μL CdSe/3CdS solution was added into the mixture of 5 mL cyclohexane, 0.9 mL TritonX-100 (poly(ethylene glycol) *p*-(1,1,3,3-tetramethylbutyl)-phenyl ether, C14H22O(C2H4O)*n* (*n* = 9-10)) and 0.9 mL hexanol. After stirring for 15 min, 0.2 mL water, 30 μL 30% NH_3 aqueous solution and 300 μL tetraethoxysilane (TEOS) were injected successively. The solution was further stirred for 24 h. 7 mL ethanol was then added to break the emulsion. After being centrifuged at 7000 rpm for 10 min, the precipitant was resuspended in ethanol. This washing procedure was repeated for two more cycles and the QD/silica particles were dispersed in ethanol.

3. Gold shelling of QD/silica particles. We first synthesized gold seed particles by dissolving 0.3425 g PVP in 19 mL water under stirring in a vial. 3.5 mL 25 mM $HAuCl_4$ solution was added into the vial, and 0.57 mL 20 mM $NaBH_4$ solution was then swiftly injected into the mixture. The color of the solution instantly changed from light yellow to dark brown. The mixture was stirred for 15 min, and the synthesized gold seed suspension was stored in dark for future use.

To decorate the $CdSe/CdS/SiO_2$ particles with Au seeds, we placed 5 mL of the particles in a 25 mL three neck flask. 200 μL APTMS was added in the flask, and the solution was stirred under 65 ^{o}C for 4 h. The solution was centrifuged at 8000 rpm for 10 min, and the precipitated particles were resuspended in ethanol. 4 mL prepared gold seed solution was then added into 1 mL functionalized QD/silica ethanol solution and stirred for 2 h. The mixture was centrifuged at 8500 rpm for 10 min and the precipitants were redissolved in gold seed solution. After five cycles of gold seed solution soaking, the resulted QD/silica/Au_{seed} was suspended in water and stored in dark.

We then formed the continuous Au shell on the particles by first adding 4.5 mL of 25 mM $HAuCl_4$ solution to 30 mL 1.8 mM K_2CO_3 solution to prepare K-gold growth solution. 30 μL QD/silica/Au seed solution was added in 3 mL K-gold growth solution, followed by the addition of 100 μL 0.35 wt.% PVP. After 5-min stirring, 30 μL formaldehyde solution (37 wt.% in water) was injected to grow the gold seeds on the particle surface by reducing Au^{3+} in the growth solution. After stirring for 1 h, the gold-shelled nanoparticles were separated by centrifugation at 8000 rpm for 10 min and dispersed in ethanol.

3.4.2 Homebuilt Confocal Microscope for Single Particle Measurements

A 70-ps pulsed laser running at 8 MHz and a central wavelength of 450 nm (LDH450-P-C-450B, PicoQuant) was collimated and focused through a pinhole to generate a transverse electromagnetic gaussian mode. The laser was directed to an immersion oil objective (100X, 1.3

NA, Zeiss) with a 490 nm long-pass dichroic mirror. The microscope is in inverted geometry and the laser pulse was focused into the sample from the bottom, which was mounted in a piezo scanning stage (PInano XYZ, P-545.3R8S). The back reflection of the laser collected by the oil-immersion objective was used to align the detection path towards the APDs and the spectrograph. The PL collected by the objective was passed through a 488 nm longpass filter,and sent either to a spectrograph (Shamrock SR-303i) equipped with a sCMOS camera (Zyla 4.2, Andor) or the Michaelson interferometer with 2 APDs (Micro-Photon-Devices PDM) at both outputs. One arm of the interferometer can be blocked to perform the Hanbury-Brown-Twiss experiment to get second order correlation function of the PL. For single particle localization, images of the samples were reconstructed with a commercial software (SymphoTime 64, PicoQuant).

3.4.3 Emission Lifetime Measurements

The same laser and homebuilt microscope, as described in the previous section 3.4.2, were used to conduct TCSPC measurements. The collected PL signal was directed to the Avalanche Photo Diode (APD, Micro-Photon-Devices PDM). The readout signal on APD and the sync signal of the laser pulse were correlated by the TCSPC module and picosecond event timer (Picoharp 300, PicoQuant). The sync channel sets each laser pulse as start time, and the other channel registers the photon arrival time relative to the start time set by the sync channel. Each TCSPC trace was recorded for 30 seconds.

3.5 Chapter Conclusion

To summarize, a structure containing a QD with a plasmonic nanoshell was synthesized to construct a hybrid plasmon-exciton coupling system. We observed a reduction in spectral diffusion behavior for a single QD exciton with the local environment engineered by the addition of silica and gold shell. The spectral diffusion suppression is attributed to two main factors, one is the silica coating passivating the QD surface and increasing the photostability, the other one is the Purcell enhancement effect from the plasmonic shell, which is demonstrated by time-resolved PL measurements.

This study proves that the plasmonic shelling strategy to achieve better emission properties is plausible for single semiconductor nanocrystals. This strategy also has a large parameter space to explore, like the plasmonic materials, thickness of the silica or plasmonic shell, etc., which opens the gates to achieve fine control of emission properties of single emitters with plasmonic nanostructures.

3.6 Supporting Information

3.6.1 Some Notes on the Colloidal Synthesis of QD/silica/Au particles.

1. Several cycles of long-time sonification and centrifugation are necessary for the silica coating step. After stirring for 24 hours for silica shell growth, some of the QD/silica particles are

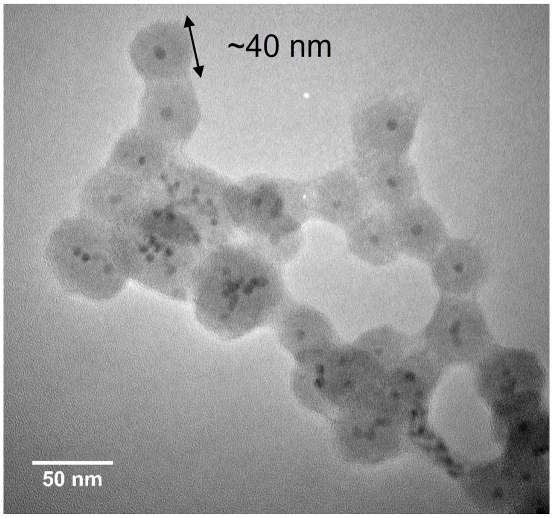

Figure 3.10. The QD/silica aggregates without several cycles of sonification and centrifugation.

stuck to each other and form large aggregates. Figure 3.10 shows a TEM image of the aggregates in solution without several rounds of sonification and centrifugation, which affects the next step of gold coating.

2. PVP can control the gold shell growth on silica surface in the final step. **Figure 3.11** shows the comparison between gold shelling with (**Figure 3.11a**) and without PVP (**Figure 3.11b**). Without PVP, gold growth is too fast and form clusters instead of merging into shell structure to cover the silica surface.

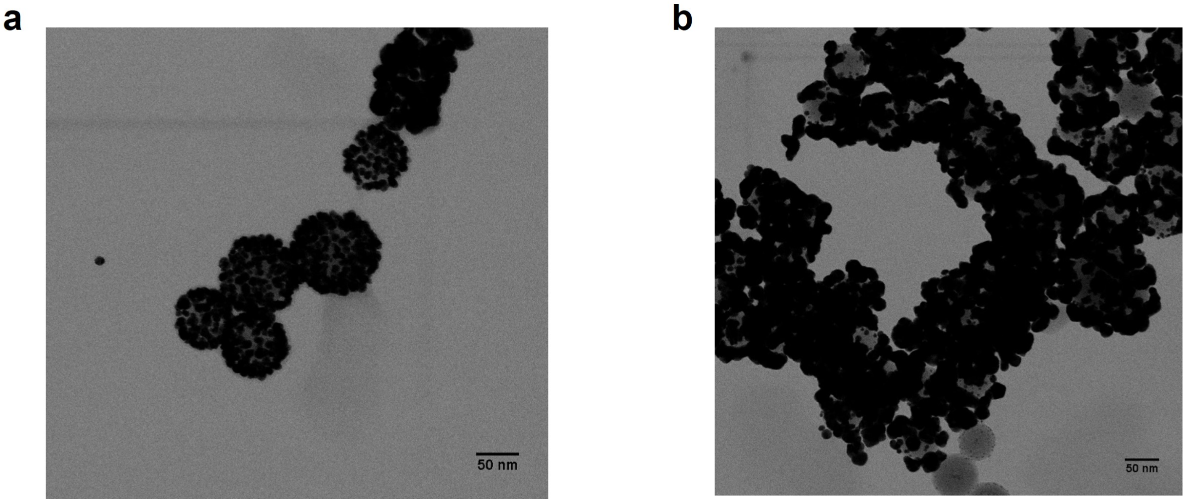

Figure 3.11. TEM images of gold shell growth with (**a**) and without (**b**) PVP.

3.6.2 Electrodynamics Simulation of Plasmonic Shell Structure

Classical electrodynamics simulations on plasmonic nanoshell were performed to predict the plasmon resonance of the structure with boundary element method (BEM).[165] The geometry input is a core/spacer/shell structure mimicking the QD/silica/gold structure in experiment, as plotted in **Scheme 3.1**. The main geometric parameter is the thickness of silica and gold shell, r_2 and r_3, respectively. **Figure 3.12a** and **Figure 3.12b** show the simulation results for one pair of parameter

r_2 = 20 nm and r_3 =10 nm. The plasmon resonance of such geometry is 586 nm and the local electric field is enhanced by about 10 times at the interface of QD.

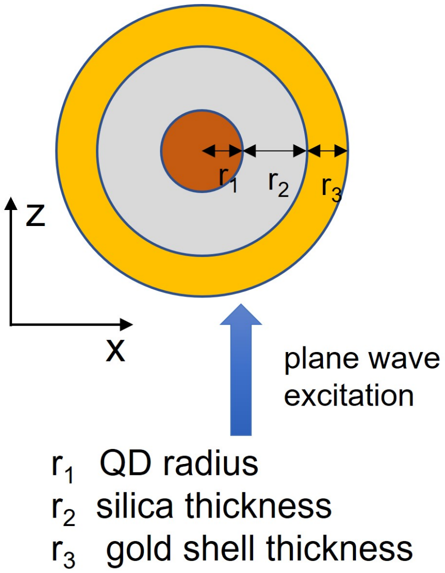

Scheme 3.1. The core/spacer/shell geometry input for the electrodynamics simulation: r_1 is the QD core radius and is set to be 2 nm. r_2 is the silica thickness and r_3 is the shell thickness. The plane wave excitation is used in the simulation.

Figure 3.12c and **Figure 3.12d** systematically plot the plasmon resonance of such plasmonic shell structures with various pairs of r_2 and r_3. The thicker the silica spacer and the thinner the plasmonic shell, the more red-shifted is the plasmonic resonance. Regarding the plasmonic material, the gold nanoshell (**Figure 3.12c**) covers the spectral range from 520 nm to infrared region, and silver nanoshell (**Figure 3.12d**) covers a broader range from 350 nm to infrared region. This is mainly related to the cut-off plasma frequency of bulk gold or silver material.

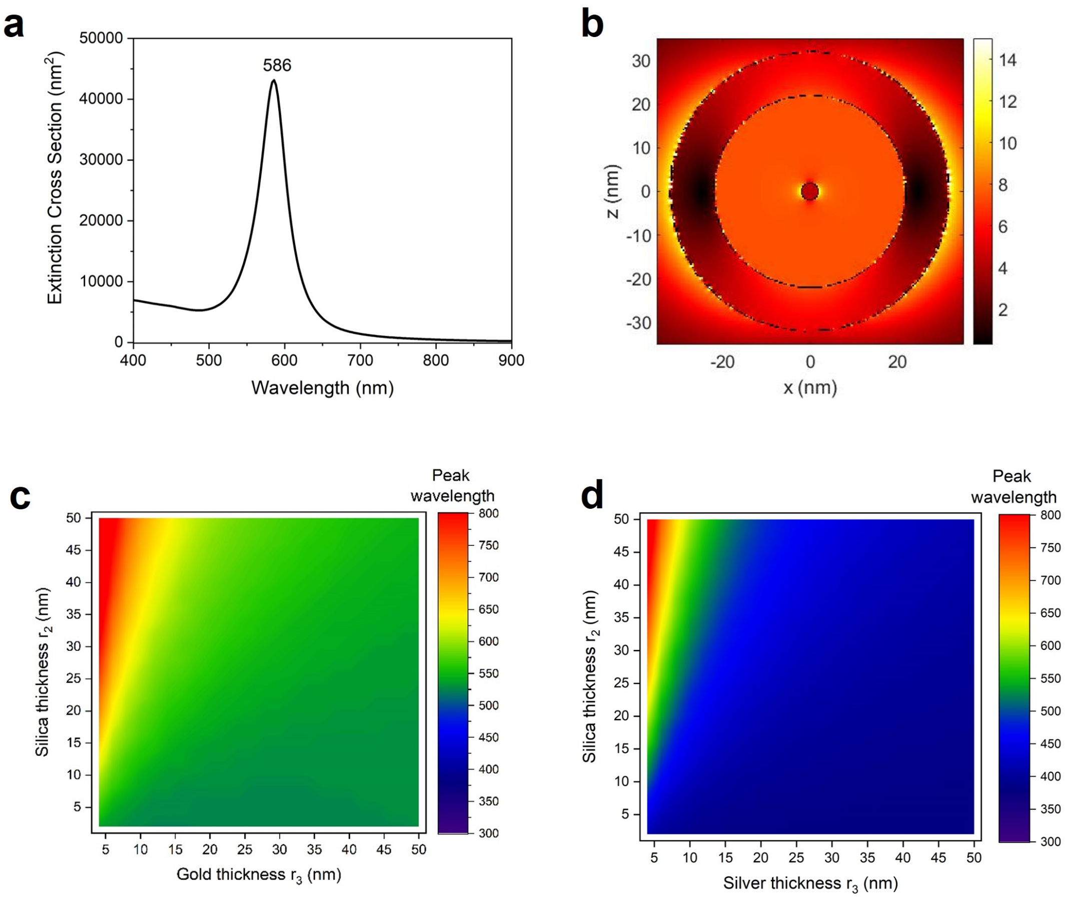

Figure 3.12. BEM simulation results for plasmonic nanoshell structure. (**a**) the simulated extinction spectrum of a geometry parameter pair of $r_2 = 20$ nm and $r_3 = 10$ nm. (**b**) The electric field distribution with the same geometry parameter as (**a**). (**c**)-(**d**) The plasmon resonance of gold (**c**) and silver (**d**) nanoshell with different r_2 and r_3.

3.6.3 Pretreatment of Glass Coverslip to Achieve Better Particle Dispersion

To perform single particle measurements through the microscope, the solution sample needs to be diluted and drop cast on the glass cover slip. Since the surface of an untreated glass cover slip is usually hydrophobic, the QD/silica/gold EtOH solution tends to form aggregates rather than disperse as single particles on the surface. By treating the glass cover slip in $NH_3 \cdot H_2O$ and H_2O_2 mixture for 60 min and rinsing with deionized water several times, the surface of glass cover slip becomes hydrophilic, and the QD/silica/gold particles prefer to disperse separately, which is more convenient to look for single particles on the microscope. Figure 3.13 shows the comparison of particle dispersion between the condition of no treatment and treatment.

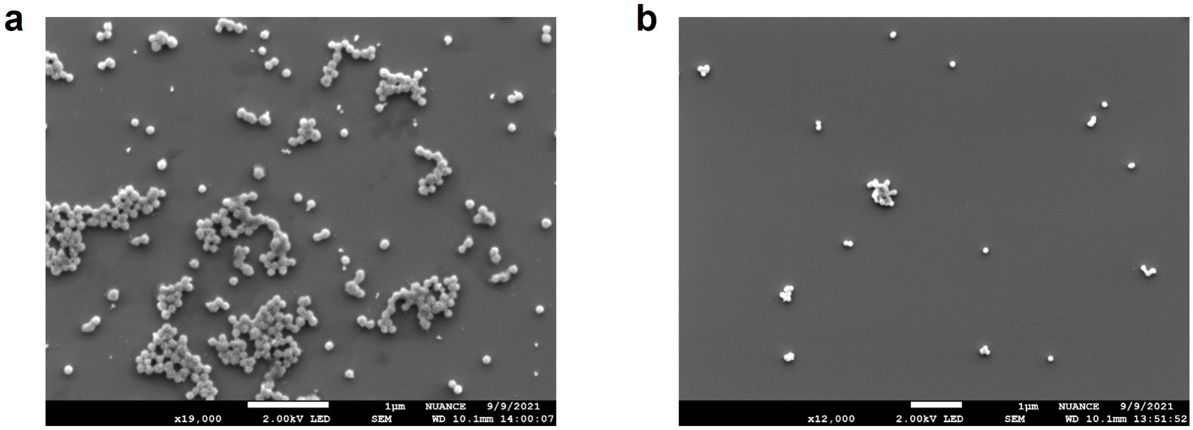

Figure 3.13. The SEM images of the QD/silica/gold particles on the surface with no pre-treatment (**a**) and treated with $NH_3 \cdot H_2O$ and H_2O_2 (**b**).

Chapter 4: Probing the Hybrid States of a Plasmon-Molecule Strongly Coupled System with Raman Excitation Spectroscopy

4.1 Chapter Summary

In this chapter, we conducted a detailed wavelength scanned surface enhanced Raman excitation spectroscopy (SERES) study on strongly coupled Ag nanoprism/TDBC J-aggregates system. Ag nanoprisms of different localized surface plasmon resonance (LSPR) relative to J-aggregates resonance were synthesized with a solution growth method. The TDBC J-aggregates were mixed with an Ag nanoprism solution and the strongly coupled system showed Rabi splitting and anti-crossing behavior in the far field extinction spectra. The wavelength scanned surface enhanced Raman excitation profiles of Ag nanoprism/TDBC J-aggregates were measured for a broad excitation wavelength range (515-640 nm) and high resolution (2 nm), and both molecular-like and plasmonic-like behaviors were observed in different strong coupling samples. Meanwhile, the SERES profiles of different samples always only show a one-peak structure and don't have clear correlation with their far field extinction spectra, which deviates from the predictions of the two coupled harmonic oscillator model. The lack of correlation between SERES profiles and extinction spectra suggests that the near field Raman response are more contributed by dark states of the hybrid system in the strong coupling regime.

4.2 Introduction

The strength of light-matter interaction can be greatly increased when photons and molecules are confined in a well-fabricated optical cavity. When the rate of coherent energy exchange between photons and molecules exceeds their individual spontaneous damping rate, the system is defined as being in the strong coupling regime (more quantitative description can be found in Chapter 1). In the strong coupling regime, two new hybrid eigenstates are generated by the mixing of cavity mode and molecular exciton, referred to as Rabi splitting.[166] To achieve strong coupling, people found that the cavity needs to have high quality factor, which is proportional to the confinement time of photons inside the cavity,[167-168] and small mode volume.[169-170] Traditional optical cavities have high quality factor but also relatively large cavity mode volume (on the order of μm^3), while plasmonic nanostructures are found to have extremely small mode volume (on the order of nm^3), so recently people have applied them as effective cavities to form plasmon-molecule strongly coupled systems.[80, 171-174] Besides fundamental interest in manipulating light-matter interaction on the nanoscale, the plasmon-molecule strong coupling can also lead to a lot of important applications like single-photon high speed switches,[89, 175] hybrid waveguides,[84] light-harvesting devices[176] and control of chemical reaction pathways.[177-178]

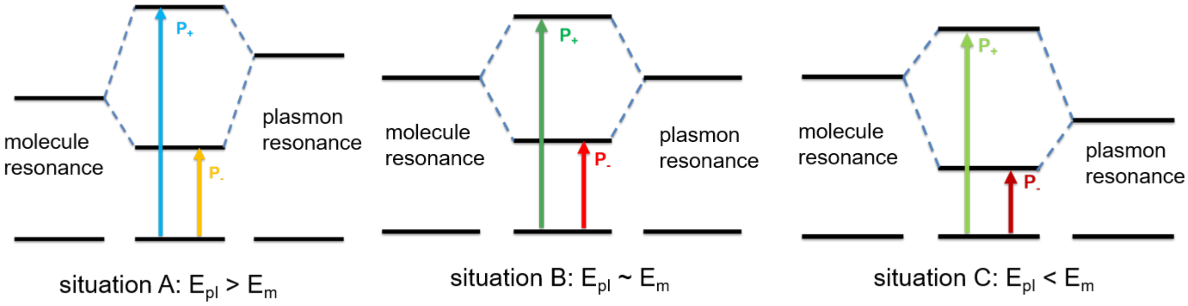

Scheme 4.1. The simplified energy mixing diagram for plasmon-molecule strong coupling according to JC model. The three plots represent three different situations of relative energies between plasmon mode and the molecules.

Although there has been extensive research on structure and material control of plasmon-molecule strong coupling, few experiments have been reported that studied the detailed dynamics of altered chemical reactions in the strong coupling regime. The first key step towards probing the dynamics is to understand the nature of the generated hybrid states. According to the Jaynes-

Cumming (JC) Model, the simplified energy mixing diagram (shown in **Scheme 4.1**) suggests that the two hybrid polariton states should both have plasmonic and molecular resonance components, with the ratio of the two components determined by plasmon energy relative to molecular excitation energy. However, until now there is no direct experimental evidence to prove or disprove this argument. Furthermore, in the situation of N identical excitons coupled with one plasmonic mode, the generalized JC model, also denoted as Tavis-Cumming (TC) model, predicts that the hybrid system will generate two bright polariton states and a degenerate manifold of N-1 dark states (shown in **Scheme 4.2**). The Tavis-Cumming Hamiltonian is written as:[70, 179]

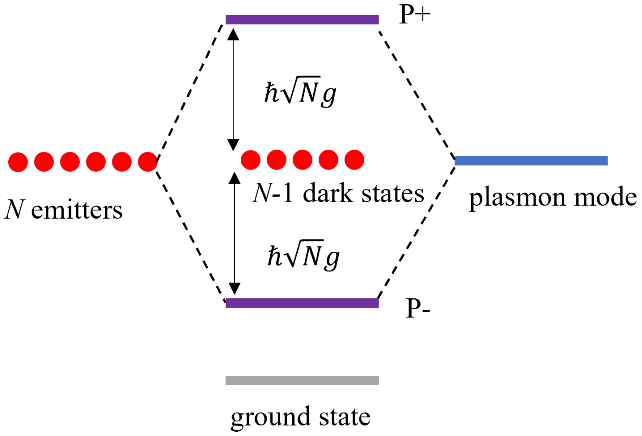

Scheme 4.2. The scheme of Tavis-Cumming model describing N emitters strongly coupled with one plasmon mode.

$$\hat{H}_{TC} = \hbar\omega_c a^\dagger a + \hbar\omega_s \sum_{i=1}^{N} \sigma_i^\dagger \sigma_i - \hbar g \sum_{i=1}^{N} \left(a^\dagger \sigma_i + a\sigma_i^\dagger\right) \quad (4.1)$$

N is the number of emitters involved in the system. The TC Hamiltonian can be rewritten in terms of bright and dark state operators, $\sigma_B = \frac{1}{\sqrt{N}} \sum_{i=1}^{N} \sigma_i$ and σ_D:

$$\hat{H}_{TC} = \hbar\omega_c a^\dagger a + \hbar\omega_s \sigma_B^\dagger \sigma_B - \hbar\sqrt{N}g\left(a^\dagger \sigma_B + a\sigma_B^\dagger\right) + \hbar\omega_s \sum_{i=1}^{N-1} \sigma_D^\dagger \sigma_D \quad (4.2)$$

which clearly shows the separate parts of hybrid polariton states and N-1 dark states. However, no experimental evidence has confirmed the effects of dark states to the system.

Here in this work, Raman excitation spectroscopy method is proposed to study the intrinsic plasmonic/molecular character of the hybrid bright polariton states, and the existence of the dark states generated in the plasmon-molecule strongly coupled system. Raman excitation spectroscopy is a spectroscopic method for tracking the relative Raman intensity of each Raman peak under different excitation wavelength, λ_{ex}. Studies have shown that the relative Raman intensity profiles I_{Raman} (λ_{ex}) have unique features for different Raman processes. For molecules where resonance Raman is important, the relative Raman intensity profiles have similar lineshape and peak position with the absorption spectrum of the resonant molecule.[180-181] For surface-enhanced Raman scattering (SERS) processes, the peak of the relative Raman intensity profile is blue shifted compared to the localized surface plasmon resonance (LSPR),[34, 182-183] and the shift is about half of the Raman frequency.[34] By examining the features of the relative Raman intensity profiles of the plasmon-molecule strongly coupled system, we can gain a clearer picture of the nature of the hybrid states.

4.3 Results and Discussion

4.3.1 Colloidal Synthesis of Silver Nanoprisms

Silver nanoprisms were synthesized following a two-step seed-induced growth method (details can be found in the section 4.4).[184] In the first step, $AgNO_3$ solution was reduced by a fresh $NaBH_4$ solution to produce a Ag(0) seed solution. The silver seeds were stabilized by trisodium citrate as the ligand. In the second step, the nanoprisms were synthesized by combining aqueous ascorbic acid and various amount of seed solution, followed by the slow addition of $AgNO_3$ solution at a uniform rate. At the end of the synthesis trisodium citrate was added to stabilize the Ag nanoprisms. By varying the amount of added seed solution, which effectively controls the number of nucleation centers in the growth solution, silver nanoprisms with different sizes were synthesized, shown in **Figure 4.1a**. **Figure 4.1c** shows the extinction spectra of a series of silver nanoprisms. The peaks represent the LSPR positions of different Ag nanoprisms, which cover a broad range from around 450 to 750 nm. **Figure 4.1b** shows the TEM image of the silver nanoprisms with the LSPR at around 600 nm. Most of them are triangle-shaped and have an edge length of around 50 nm. This seed-induced method offers an easy and reproducible way to synthesize silver nanoprisms with widely tunable LSPRs.

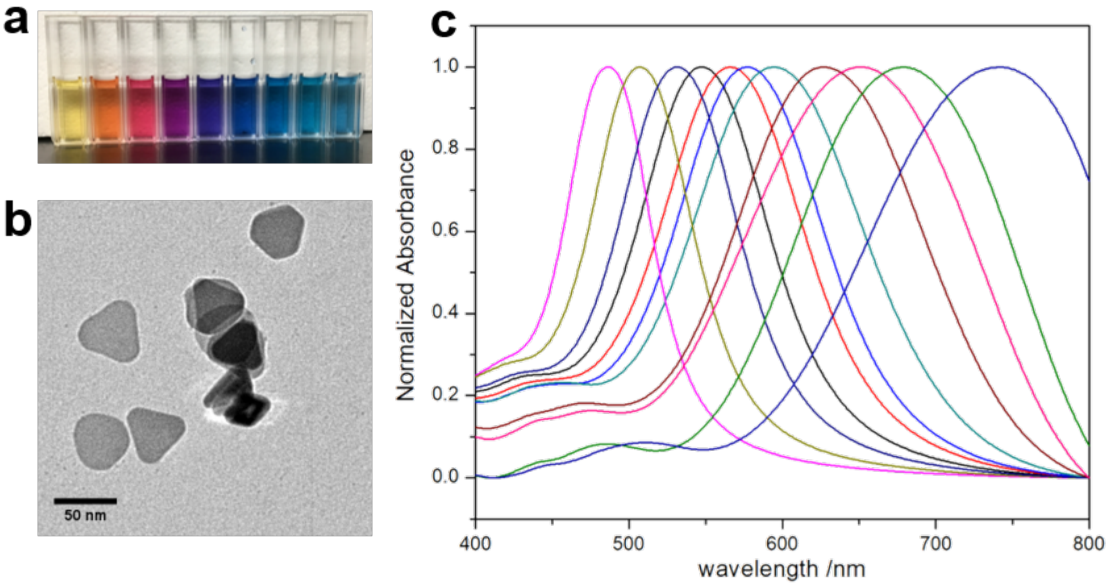

Figure 4.1. (**a**) Photograph of Ag nanoprisms with different sizes. (**b**) TEM image of Ag nanoprisms with LSPR around 600 nm. The edge length is about 50 nm. (**c**) Normalized Extinction spectra of a series of Ag nanoprisms with different sizes.

4.3.2 TDBC J-aggregates

For the molecule to couple with the silver nanoprisms, TDBC (5, 5’,6,6’-tetrachloro-di-(4-sulfobutyl) benzimidazolocarbocyanine) J-aggregates were chosen because they have a narrow and intense J-band absorption feature and can be absorbed on silver surface. The molecular structure is shown in the inset of **Figure 4.2**. The TDBC monomer itself is a water-soluble cyanine dye and forms J-aggregates in a 1 mM KCl solution. The two peaks at 483 nm and 514 nm in **Figure 4.2** correspond to its monomer absorption. The black line shows the absorption of TDBC solution with salt KCl. The monomer absorption features are greatly suppressed and a strong, sharp peak at 587 nm rises in the spectrum, which corresponds to its J-band absorption. This strong and sharp absorption peak indicates that the TDBC J band transition has a high oscillation strength which helps to achieve strong coupling with the silver nanoprisms.

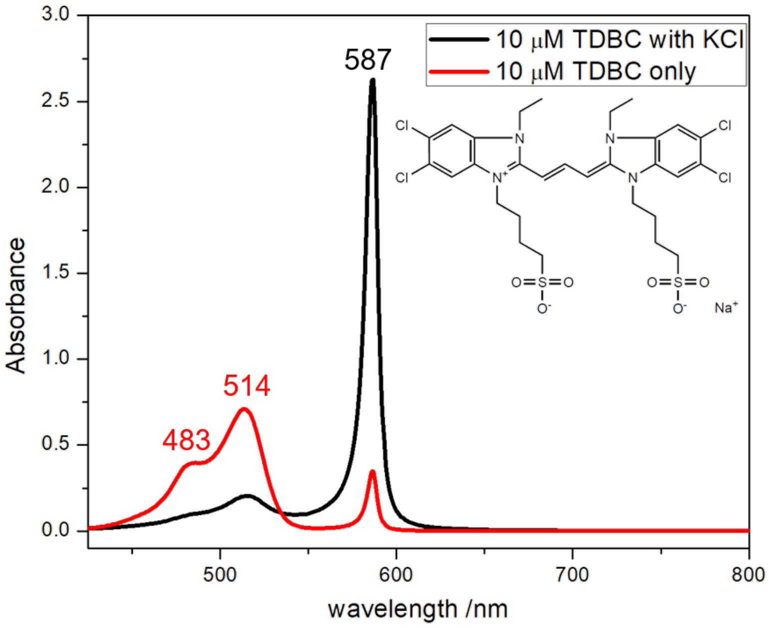

Figure 4.2. The TDBC absorption spectra. Black line is 10 μM aqueous TDBC solution with KCl salt. Red line is bare 10 μM aqueous TDBC solution. The inset is the molecule structure of TDBC monomer.

4.3.3 Rabi Splitting of Silver Nanoprism/TDBC J-aggregates

To form a strongly coupled Ag nanoprism/TDBC J-aggregates sample, 0.5 mL 0.1mM TDBC solution was added into 1 mL Ag nanoprism solution. The well mixed solution was centrifuged twice to remove excess TDBC dye molecules. Adding excess TDBC solution makes it valid to assume the surface coverage of TDBC J-aggregates on silver nanoprisms with different sizes are similar.

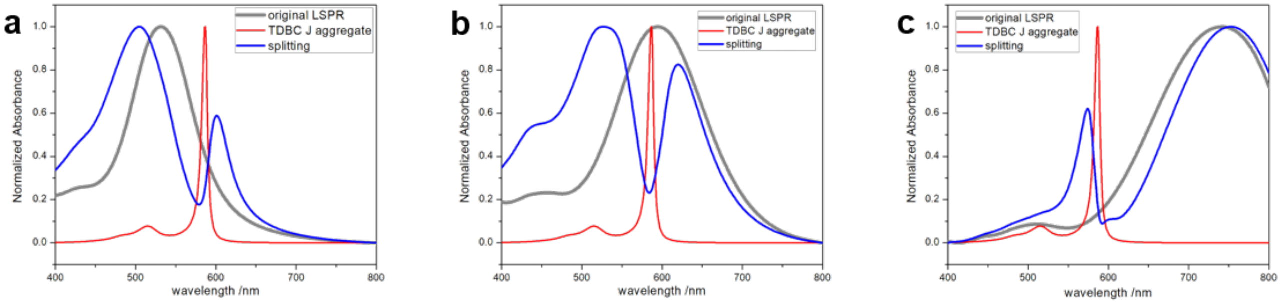

Figure 4.3. Extinction spectra showing Rabi splitting under three different coupling situations. (**a**) LSPR higher than molecular resonance. (**b**) LSPR near molecular resonance. (**c**) LSPR lower than molecular resonance. For each spectrum, grey line is the original LSPR, red line is TDBC J-aggregates absorption, blue line is the extinction of the strongly coupled system. All the spectra are normalized for better comparison.

Figure 4.3 shows the extinction spectra of three silver nanoprism/TDBC J-aggregates samples with silver nanoprisms of different sizes, thus different LSPRs. For example, **Figure 4.3a** shows a sample where the plasmon energy is higher than the TDBC J band energy. The original LSPR is around 532 nm and the J-band is at 587 nm. The extinction spectrum of the strong coupling sample shows clear Rabi splitting, with the upper hybrid band at 498 nm and lower hybrid band at 605 nm. By increasing the size of the Ag nanoprisms, the LSPR is tuned from higher than the J-band (**Figure 4.3a**), near the J-band (**Figure 4.3b**), to lower than the J-band (**Figure 4.3c**), with the Rabi splitting indicative of strong coupling observed in all the cases and following the trend of the decreasing plasmon energy.

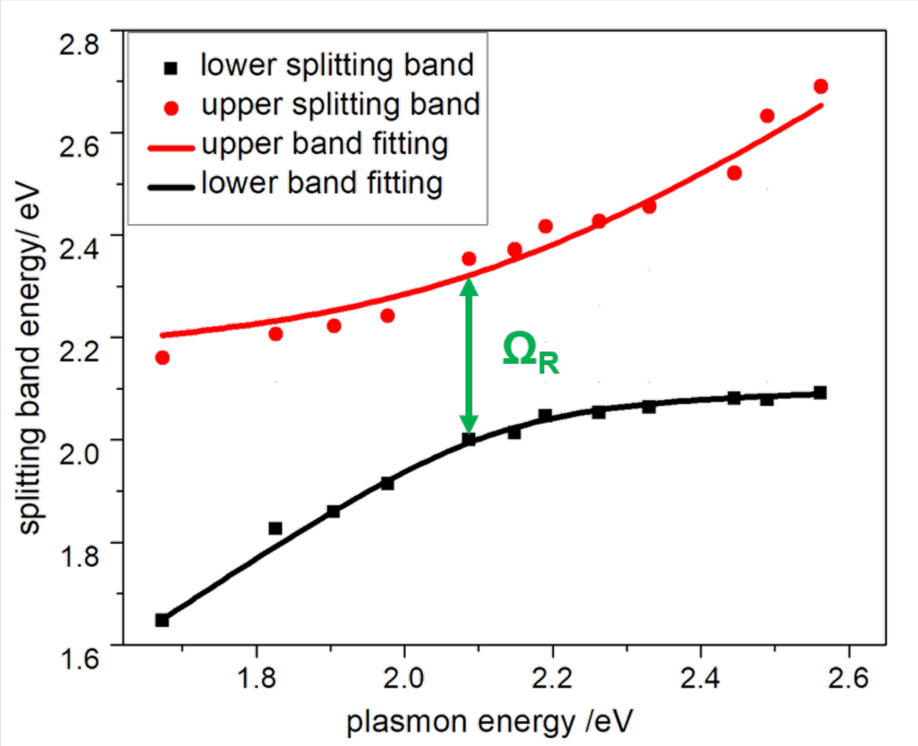

Figure 4.4. The anti-crossing behavior of the two hybrid bands formed in silver nanoprism/TDBC J-aggregates strongly coupled system with different-size silver nanoprisms. The red and black dots are the splitting band energy extracted from the extinction spectra. The red and black curves are the fitting curve with eqn. 4.3.

To analyze the trend of the Rabi splitting more quantitatively, a series of extinction spectra were taken on the strong coupling samples tuning the LSPRs of the Ag nanoprisms. Then the energy of the two hybrid bands were plotted against the original plasmon energy (**Figure 4.4**). The upper and lower hybrid bands show a clear anti-crossing behavior. Based on the coupled harmonic oscillator model, this anti-crossing behavior can be expressed by the following equation:

$$E^{UB,LB}(\hbar\omega_p) = \frac{\hbar\omega_p + \hbar\omega_0}{2} \pm \frac{1}{2}\sqrt{(\hbar\Omega_R)^2 + (\hbar\omega_p - \hbar\omega_0)^2} \qquad (4.3)$$

Here $\hbar\omega_p$ and $\hbar\omega_0$ are the uncoupled plasmon and molecular excitation energies, respectively. $\hbar\Omega_R$ is the coupling energy, which is also known as Rabi splitting energy. The data were fitted with the eqn 4.3 above, and the fitting curves are also shown in the **Figure 4.4**. The fitting matches the observed experimental trend, with the coupling energy of about 310 meV, which is also in good agreement with literature reports on similar plasmon-molecule strongly coupled system.[42]

4.3.4 SERS Spectra of TDBC J-aggregates

To get the wavelength-scanned Raman excitation profile of the strongly coupled system, it is required that the surface-enhanced Raman spectra of TDBC J-aggregates have strong Raman peaks so that the intensity information can be extracted to plot the Raman excitation profile.

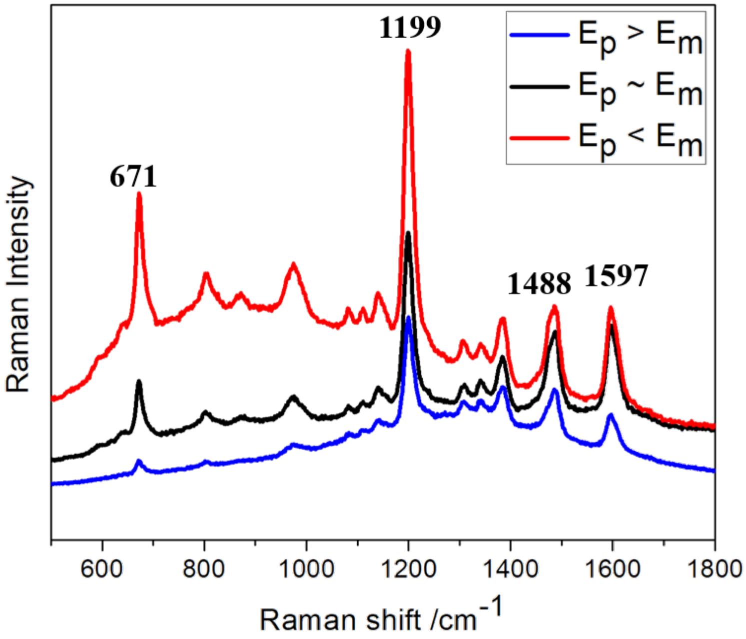

Figure 4.5. SERS spectra of TDBC J-aggregates on silver nanoprisms under three different situations (E_p>E_m; E_p~E_m; E_p<E_m) at the excitation wavelength of 558 nm. E_p is the plasmon mode energy, and E_m is the J-band energy of TDBC J-aggregates.

Figure 4.5 shows three SERS spectra of TDBC J-aggregates coupled with silver nanoprisms of different sizes in solution. Under the same excitation wavelength (556 nm), the three SERS spectra have the same Raman peak positions, but the relative peak intensities between each Raman mode are quite different. Within the spectral region, Four Raman peaks (671 cm^{-1}, 1199 cm^{-1}, 1488 cm^{-1} and 1597 cm^{-1}) are picked to monitor their Raman excitation profiles.

4.3.5 Raman Excitation Spectra of Silver Nanoprism/TDBC J-aggregates

Raman excitation spectroscopy is a wavelength scanned experiment to extract the dependence of relative Raman intensity on excitation wavelength. This technique is often limited by the tunability of the excitation laser and detection system.[34] To overcome this limitation, a continuous-wave laser system was used to conduct the wavelength scanned experiments. This laser system has two main advantages. First it has very fine spectral linewidth up to 0.0001 nm. Second it covers a broad spectral range from UV to near IR. These two advantages allow us to collect enough data points to show the fine features of Raman excitation profiles over the large wavelength range.

The basic procedure of generating Raman excitation profiles of Ag nanoprism/TDBC J-aggregates system contains three steps: 1) collect the SERS spectra under different excitation wavelengths. 2) The chosen Raman peaks were fitted with single Lorentzian peak function to extract the peak intensities at each excitation wavelength. At each wavelength, five SERS spectra were collected for averaged peak intensity and the standard deviation. 3) normalize the peak intensity with incident power, acquisition time and the Raman cross sections of TDBC J-aggregates[185] to generate relative intensity profiles as a function of incident excitation wavelength. More details can be found in the Supporting Information section 4.6.

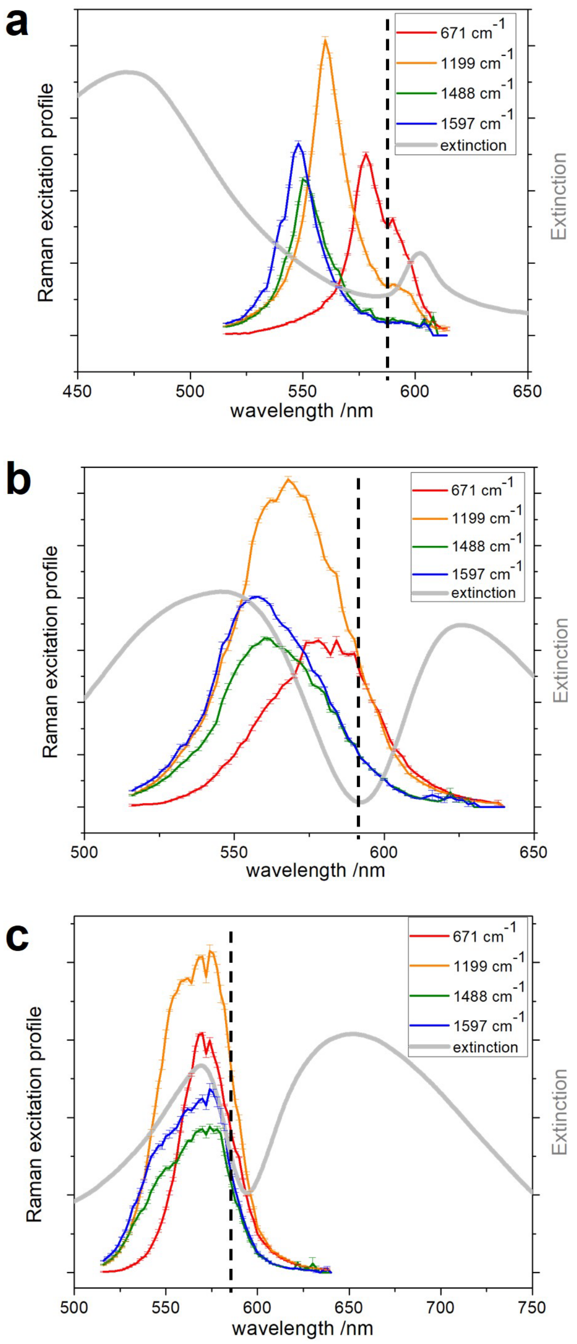

Figure 4.6. Raman excitation profiles for three situations: (**a**) $E_p > E_m$ (**b**) $E_p \sim E_m$ (**c**) $E_p < E_m$. E_p is the plasmon mode energy, and E_m is the J-band energy of TDBC J-aggregates. Black dash line is the peak position of original TDBC J-band.

The results are shown in **Figure 4.6**. **Figure 4.6a** is the situation that plasmon energy is higher than TDBC J-band energy. The grey curve is the extinction spectrum of the Ag nanoprism/TDBC J-aggregates strongly coupled system. The colored curves are Raman excitation profiles of 671 cm^{-1}, 1199 cm^{-1}, 1488 cm^{-1}, 1597 cm^{-1} these four Raman peaks. First, the standard deviation of each measurement is very small indicating the laser power is quite stable, so there was no large peak intensity fluctuation during the entire wavelength scan experiment. In **Figure 4.6a**, all the four Raman excitation profiles are blue shifted compared to the lower hybrid band position. In addition, the peak shift follows the order of Raman frequencies, which means 671 cm^{-1} is closest to the lower band and 1597 cm^{-1} is farthest away from the lower band. These features clearly indicate that the lower band has a large plasmon-like character when plasmon energy is higher than the molecular excitation energy, while the simplified energy mixing diagram predicts the lower band will be more molecular-like under this situation. On the contrary, **Figure 4.6c** is the situation that plasmon energy is lower than TDBC J-band energy. In this case all the Raman excitation profiles line up together and align with the upper band, showing a typical resonant-molecule behavior. This indicates that the upper band has mainly molecular-like content when plasmon energy is lower than the molecular excitation energy, which fits the prediction of the energy mixing diagram.

When the plasmon energy is close to molecular excitation energy (shown in **Figure 4.6b**), the results are more complicated. All the Raman excitation profiles are located right between the upper band and lower band of the strong coupling system, which is hard to explain by plasmon effect of the two hybrid states. Meanwhile, the peak positions of these profiles are not the same, which means molecular effect also fails to explain the phenomenon. Since all the Raman excitation profiles are in the middle of the two hybrid polariton states, it can be inferred that the large manifold of the dark states predicted by TC model is main contributor to the SERS signals under this situation. We also found that in all the Raman excitation spectra only one-peak structure has been observed, while theoretically both the upper band and the lower band are expected to contribute to the spectra.

The analysis above demonstrates that the simple JC model (energy level mixing diagram) can explain the character of the hybrid polariton states under some situations, but it could fail especially when the energies of the two components are close to each other.

4.4 Experimental Methods

4.4.1 Synthesis Procedure of Silver Nanoprisms

Silver nanoprisms with different sizes were synthesized following a published procedure.[184] The first step is to make silver seeds. 5 mL 2.5 mM trisodium citrate, 0.25 mL 500 mg·L^{-1} poly(sodium styrenesulphonate) (PSSS) and 0.3 mL 10 mM freshly prepared $NaBH_4$ aqueous solution were mixed in a 25 mL round-bottom flask. 5 mL 0.5 mM $AgNO_3$ solution was added to the mixture with a speed of 2mL·L^{-1}. The mixture was stirred for another 10 min after the addition of $AgNO_3$ solution.

In another 50 mL round-bottom flask, 5 mL deionized water, 75 µL 10 mM ascorbic acid and certain amount the freshly prepared Ag seed solution was mixed and stirred continuously. Meanwhile, 3 mL 0.5 mM $AgNO_3$ aqueous solution was added into the mixture at the rate of 1 mL·L^{-1}. The amount of added Ag seed solution determines the size of the synthesized silver nanoprisms. During the addition of $AgNO_3$ solution, the color of the mixture changed gradually from blue all the way to orange. After the solution addition is completed, 0.5 mL 25 mM trisodium citrate aqueous solution was injected to stabilize the silver nanoprisms.

After the synthesis, the morphologies of the silver nanoprisms were imaged by Hitachi 8100-TEM using 200 kV of thermionic emission voltage.

4.4.2 Wavelength-Scanned Raman Excitation Spectroscopy

The wavelength-scanned Raman excitation spectroscopy is done with a super continuum wavelength-tunable laser system (M squared, Glasgow). A small rotational stage (Thorlabs) was designed to hold as many as eight solution samples at the same time and can be auto controlled by the self-written LabVIEW code. The scattered Raman signals were collected into a TriplePro three-stage spectrometer (Princeton Instruments) with a ProEM CCD camera (Princeton Instruments).

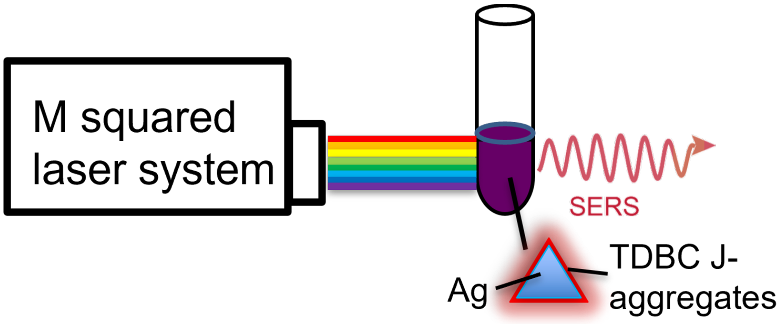

Scheme 4.3. The basic setup for wavelength-scanned Raman excitation spectroscopy experiments.

4.5 Chapter Conclusion

In this chapter, a plasmon-exciton strongly coupled system, composed of synthesized silver nanoprisms and strong emitter TDBC J-aggregates, is constructed and studied by surface-enhanced wavelength-scanned Raman excitation spectroscopy. The Raman excitation profiles of several Raman modes reveal some plasmonic or molecular character in the hybrid polariton bright states under some circumstances, which fit the description of the plasmon-exciton strong coupling from the simple Jaynes-Cumming model. In the cases that the energies of the two components are close, however, the Raman excitation profiles show more contribution from the dark states instead of the two bright polariton states in the strong coupling regime.

4.6 Supporting Information

4.6.1 The Surface Coverage of TDBC J-aggregates on Silver Nanoprisms

When mixing the aqueous solution of silver nanoprisms and TDBC J-aggregates to form strong coupling system, excess floating TDBC J-aggregates bring in extra Raman signals and strong fluorescence background, which makes it impossible to accurately extract the Raman intensity information. To prevent the affect from the free dye molecules in the solution, the mixture is

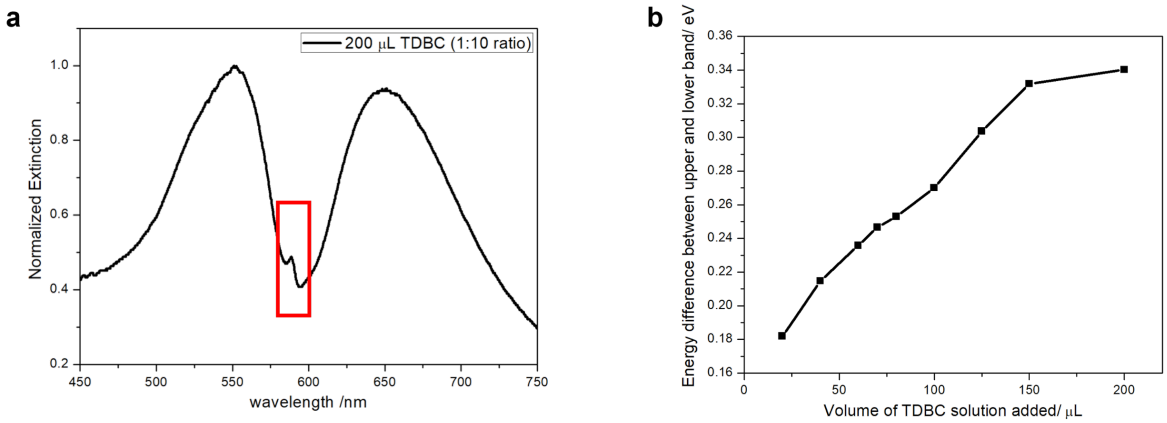

Figure 4.7. (**a**) The extinction spectrum of mixed silver nanoprism/TDBC J-aggregates with free floating TDBC J-aggregates in the solution. The red box region is the absorption of the dye. (**b**) The Rabi splitting energies of a series of silver nanoprism/TDBC J-aggregates with different added volume of TDBC J-aggregates.

centrifuged twice to remove all the excess TDBC J-aggregates. **Figure 4.7a** shows the extinction spectra of the mixture with free floating TDBC J-aggregates. On the other hand, the surface coverage of the dye molecules on the nanoprism surface is an important experimental factor which controls the Rabi splitting energy. A series of samples in which different TDBC J-aggregates solution volume mixed with 1 mL silver nanoprisms were made and the corresponding Rabi splitting energies were examined with uv-vis spectroscopy, as shown in **Figure 4.7b**. The plot shows an increase at the beginning of adding more TDBC J-aggregates and comes to a plateau at the volume of 200 μL, indicating that the surface of silver nanoprisms are mostly covered at the volume of 200 μL. When preparing the samples for the wavelength-scanned Raman excitation spectroscopy experiments, 500 μL TDBC J-aggregates aqueous solution was mixed with 1 mL silver nanoprisms, and the mixture was centrifuged twice. This procedure secures the almost full coverage of TDBC J-aggregates on the surface of silver nanoprisms, and no excess TDBC J-aggregates in the solution.

4.6.2 The Detailed Procedure to Generate Raman Excitation Profile

The Raman excitation profile is the relative Raman intensity of a certain Raman mode under different excitation wavelengths. The main difficulties are how to extract the accurate peak intensity from SERS spectra and how to normalize the intensity to compare it across different excitation wavelengths. **Figure 4.8** is a SERS spectrum of TDBC J-aggregates excited at 558 nm. If we focus on the 1199 cm^{-1} Raman mode, first the background is subtracted by extrapolating the background of the peak region with a smooth curve associated with the background signal over the whole spectral region. Then the 1199 cm^{-1} peak region is fitted with a single Lorentzian peak, shown as the red curve in Figure 4.8. At each wavelength, 5 SERS spectra are collected, and similar fitting procedures are done for all five spectra to extract the averaged peak intensity $\bar{I}_{SERS,1199\ cm^{-1}}(558\ nm)$ and the standard deviation.

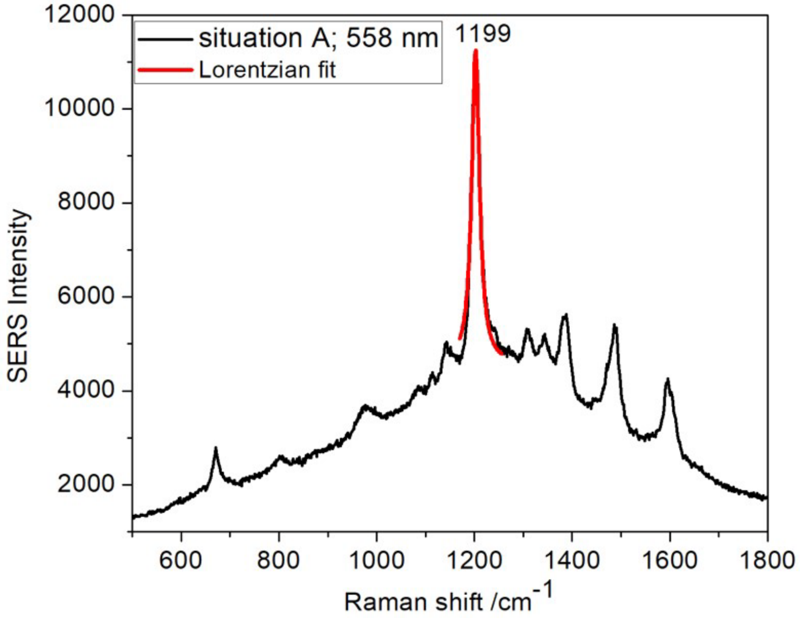

Figure 4.8. The SERS spectrum of TDBC J-aggregates at the excitation wavelength of 558 nm. The red curve is the Lorentzian fit of the peak after the background subtraction.

The next step is to compare the averaged intensities under different excitation wavelength. The laser power difference is one of the most important experimental factors that influences the Raman intensity, so the intensity needs to be normalized. Instead of measuring the laser power every time, a comparison method is used here. At each wavelength, not only 5 SERS spectra of TDBC J-aggregates but also 5 normal Raman spectra of cyclohexane are collected. So the normalized Raman intensity is expressed as:

$$I_{SERS,1199\ cm^{-1}}(558\ nm) = \frac{\bar{I}_{SERS,1199\ cm^{-1}}(558\ nm)}{\bar{I}_{Raman,chx\ 801\ cm^{-1}}(558\ nm)}$$

4.6.3 Silver Nanoprism/TDBC J-aggregates Strong Coupling System on Single Particle Level

Most of the experiments in this chapter are done in the solution phase. In this section it is demonstrated that the same system can also achieve strong coupling regime on single particle level. The diluted solution of silver nanoprism/TDBC J-aggregates was drop cast on a TEM grid and put on a inverted microscope (Nikon, Ti-U). A dark-field condenser was used to collect single-particle dark field scattering spectrum (**Figure 4.9a**). Then the collimated laser beam was sent into the microscope, and the SERS signals of the same particle was collected through a spectrometer with electrically cooled CCD camera (**Figure 4.9b**).

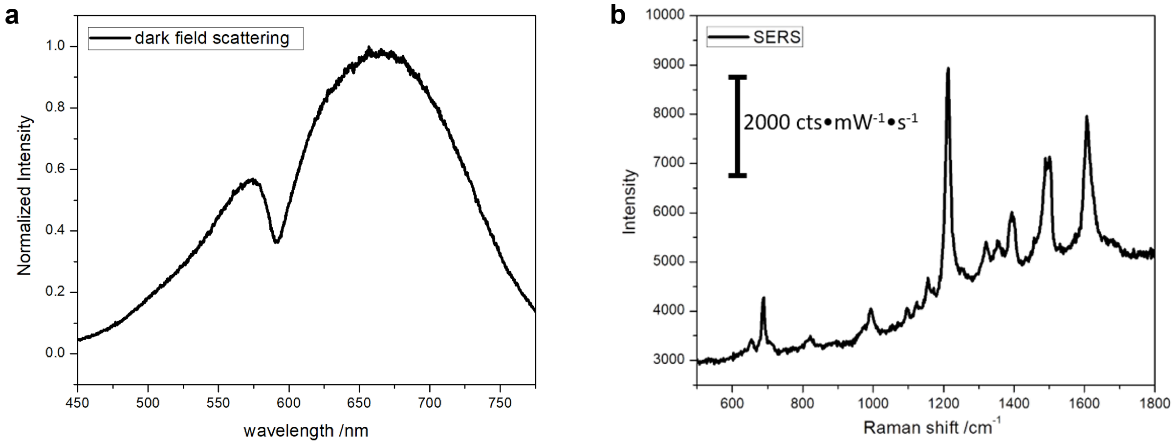

Figure 4.9. The correlated single-particle dark field scattering(**a**) and SERS(**b**) of silver nanoprism/TDBC J-aggregates.

References

(1) Willets, K. A.; Duyne, R. P. V., Localized Surface Plasmon Resonance Spectroscopy and Sensing. *Annu. Rev. Phys. Chem.* **2007,** *58* (1), 267-297.

(2) Kelly, K. L.; Coronado, E.; Zhao, L. L.; Schatz, G. C., The Optical Properties of Metal Nanoparticles: The Influence of Size, Shape, and Dielectric Environment. *The Journal of Physical Chemistry B* **2003,** *107* (3), 668-677.

(3) Hao, E.; Schatz, G. C., Electromagnetic fields around silver nanoparticles and dimers. *J. Chem. Phys.* **2004,** *120* (1), 357-366.

(4) Kinkhabwala, A.; Yu, Z. F.; Fan, S. H.; Avlasevich, Y.; Mullen, K.; Moerner, W. E., Large Single-Molecule Fluorescence Enhancements Produced by a Bowtie Nanoantenna. *Nat. Photonics* **2009,** *3* (11), 654-657.

(5) Qin, L. D.; Zou, S. L.; Xue, C.; Atkinson, A.; Schatz, G. C.; Mirkin, C. A., Designing, fabricating, and imaging Raman hot spots. *Proc. Natl. Acad. Sci. U. S. A.* **2006,** *103* (36), 13300-13303.

(6) Camden, J. P.; Dieringer, J. A.; Wang, Y.; Masiello, D. J.; Marks, L. D.; Schatz, G. C.; Van Duyne, R. P., Probing the Structure of Single-Molecule Surface-Enhanced Raman Scattering Hot Spots. *Journal of the American Chemical Society* **2008,** *130* (38), 12616-12617.

(7) Wustholz, K. L.; Henry, A. I.; McMahon, J. M.; Freeman, R. G.; Valley, N.; Piotti, M. E.; Natan, M. J.; Schatz, G. C.; Van Duyne, R. P., Structure-Activity Relationships in Gold Nanoparticle Dimers and Trimers for Surface-Enhanced Raman Spectroscopy. *Journal of the American Chemical Society* **2010,** *132* (31), 10903-10910.

(8) Guidez, E. B.; Aikens, C. M., Quantum mechanical origin of the plasmon: from molecular systems to nanoparticles. *Nanoscale* **2014,** *6* (20), 11512-11527.

(9) Aikens, C. M.; Li, S.; Schatz, G. C., From Discrete Electronic States to Plasmons: TDDFT Optical Absorption Properties of Ag_n (n = 10, 20, 35, 56, 84, 120) Tetrahedral Clusters. *The Journal of Physical Chemistry C* **2008,** *112* (30), 11272-11279.

(10) Guidez, E. B.; Aikens, C. M., Plasmon resonance analysis with configuration interaction. *Phys. Chem. Chem. Phys.* **2014,** *16* (29), 15501-15509.

(11) Gieseking, R. L.; Ratner, M. A.; Schatz, G. C., Semiempirical Modeling of Ag Nanoclusters: New Parameters for Optical Property Studies Enable Determination of Double Excitation Contributions to Plasmonic Excitation. *The Journal of Physical Chemistry A* **2016,** *120* (26), 4542-4549.

(12) Gieseking, R. L.; Ratner, M. A.; Schatz, G. C., Review of Plasmon-Induced Hot-Electron Dynamics and Related SERS Chemical Effects. In *Frontiers of Plasmon Enhanced Spectroscopy Volume 1*, American Chemical Society: 2016; Vol. 1245, pp 1-22.

(13) Jeanmaire, D. L.; Van Duyne, R. P., Surface Raman spectroelectrochemistry: Part I. Heterocyclic, aromatic, and aliphatic amines adsorbed on the anodized silver electrode. *Journal of Electroanalytical Chemistry and Interfacial Electrochemistry* **1977,** *84* (1), 1-20.

(14) Albrecht, M. G.; Creighton, J. A., Anomalously Intense Raman Spectra of Pyridine at a Silver Electrode. *Journal of the American Chemical Society* **1977,** *99* (15), 5215-5217.

(15) Moskovits, M., Surface-enhanced Spectroscopy. *Rev. Mod. Phys.* **1985,** *57* (3), 783-826.

(16) Greeneltch, N. G.; Blaber, M. G.; Henry, A.-I.; Schatz, G. C.; Van Duyne, R. P., Immobilized Nanorod Assemblies: Fabrication and Understanding of Large Area Surface-Enhanced Raman Spectroscopy Substrates. *Analytical Chemistry* **2013,** *85* (4), 2297-2303.

(17) Kleinman, S. L.; Sharma, B.; Blaber, M. G.; Henry, A.-I.; Valley, N.; Freeman, R. G.; Natan, M. J.; Schatz, G. C.; Van Duyne, R. P., Structure Enhancement Factor Relationships in Single Gold Nanoantennas by Surface-Enhanced Raman Excitation Spectroscopy. *Journal of the American Chemical Society* **2013,** *135* (1), 301-308.

(18) Zrimsek, A. B.; Wong, N. L.; Van Duyne, R. P., Single Molecule Surface-Enhanced Raman Spectroscopy: A Critical Analysis of the Bianalyte versus Isotopologue Proof. *The Journal of Physical Chemistry C* **2016,** *120* (9), 5133-5142.

(19) Gawinkowski, S.; Pszona, M.; Gorski, A.; Niedziolka-Jonsson, J.; Kaminska, I.; Nogala, W.; Waluk, J., Single Molecule Raman Spectra of Porphycene Isotopologues. *Nanoscale* **2016,** *8* (6), 3337-3349.

(20) Sonntag, M. D.; Klingsporn, J. M.; Garibay, L. K.; Roberts, J. M.; Dieringer, J. A.; Seideman, T.; Scheidt, K. A.; Jensen, L.; Schatz, G. C.; Van Duyne, R. P., Single-Molecule Tip-Enhanced Raman Spectroscopy. *The Journal of Physical Chemistry C* **2012,** *116* (1), 478-483.

(21) Lee, J.; Crampton, K. T.; Tallarida, N.; Apkarian, V. A., Visualizing Vibrational Normal Modes of a Single Molecule with Atomically Confined Light. *Nature* **2019,** *568* (7750), 78-82.

(22) Pazos-Perez, N.; Pazos, E.; Catala, C.; Mir-Simon, B.; Gomez-de Pedro, S.; Sagales, J.; Villanueva, C.; Vila, J.; Soriano, A.; de Abajo, F. J. G.; Alvarez-Puebla, R. A., Ultrasensitive Multiplex Optical Quantification of Bacteria in Large Samples of Biofluids. *Sci Rep* **2016,** *6*, 10.

(23) Vander Ende, E.; Bourgeois, M. R.; Henry, A.-I.; Chávez, J. L.; Krabacher, R.; Schatz, G. C.; Van Duyne, R. P., Physicochemical Trapping of Neurotransmitters in Polymer-Mediated Gold Nanoparticle Aggregates for Surface-Enhanced Raman Spectroscopy. *Analytical Chemistry* **2019,** *91* (15), 9554-9562.

(24) Park, J. E.; Yonet-Tanyeri, N.; Vander Ende, E.; Henry, A.-I.; Perez White, B. E.; Mrksich, M.; Van Duyne, R. P., Plasmonic Microneedle Arrays for in Situ Sensing with Surface-Enhanced Raman Spectroscopy (SERS). *Nano Letters* **2019,** *19* (10), 6862-6868.

(25) Pallaoro, A.; Hoonejani, M. R.; Braun, G. B.; Meinhart, C. D.; Moskovits, M., Rapid Identification by Surface-Enhanced Raman Spectroscopy of Cancer Cells at Low Concentrations Flowing in a Microfluidic Channel. *ACS Nano* **2015,** *9* (4), 4328-4336.

(26) Hackler, R. A.; McAnally, M. O.; Schatz, G. C.; Stair, P. C.; Van Duyne, R. P., Identification of Dimeric Methylalumina Surface Species during Atomic Layer Deposition Using Operando

Surface-Enhanced Raman Spectroscopy. *Journal of the American Chemical Society* **2017,** *139* (6), 2456-2463.

(27) Hackler, R. A.; Kang, G.; Schatz, G. C.; Stair, P. C.; Van Duyne, R. P., Analysis of TiO_2 Atomic Layer Deposition Surface Chemistry and Evidence of Propene Oligomerization Using Surface-Enhanced Raman Spectroscopy. *Journal of the American Chemical Society* **2019,** *141* (1), 414-422.

(28) Kurouski, D.; Mattei, M.; Van Duyne, R. P., Probing Redox Reactions at the Nanoscale with Electrochemical Tip-Enhanced Raman Spectroscopy. *Nano Letters* **2015,** *15* (12), 7956-7962.

(29) Nguyen, D.; Kang, G.; Chiang, N.; Chen, X.; Seideman, T.; Hersam, M. C.; Schatz, G. C.; Van Duyne, R. P., Probing Molecular-Scale Catalytic Interactions between Oxygen and Cobalt Phthalocyanine Using Tip-Enhanced Raman Spectroscopy. *Journal of the American Chemical Society* **2018,** *140* (18), 5948-5954.

(30) Frontiera, R. R.; Henry, A.-I.; Gruenke, N. L.; Van Duyne, R. P., Surface-Enhanced Femtosecond Stimulated Raman Spectroscopy. *The Journal of Physical Chemistry Letters* **2011,** *2* (10), 1199-1203.

(31) Gruenke, N. L.; McAnally, M. O.; Schatz, G. C.; Van Duyne, R. P., Balancing the Effects of Extinction and Enhancement for Optimal Signal in Surface-Enhanced Femtosecond Stimulated Raman Spectroscopy. *The Journal of Physical Chemistry C* **2016,** *120* (51), 29449-29454.

(32) Keller, E. L.; Frontiera, R. R., Ultrafast Nanoscale Raman Thermometry Proves Heating Is Not a Primary Mechanism for Plasmon-Driven Photocatalysis. *ACS Nano* **2018,** *12* (6), 5848-5855.

(33) Stiles, P. L.; Dieringer, J. A.; Shah, N. C.; Duyne, R. P. V., Surface-Enhanced Raman Spectroscopy. *Annu. Rev. Anal. Chem.* **2008,** *1* (1), 601-626.

(34) McFarland, A. D.; Young, M. A.; Dieringer, J. A.; Van Duyne, R. P., Wavelength-Scanned Surface-Enhanced Raman Excitation Spectroscopy. *The Journal of Physical Chemistry B* **2005,** *109* (22), 11279-11285.

(35) Masango, S. S.; Hackler, R. A.; Large, N.; Henry, A.-I.; McAnally, M. O.; Schatz, G. C.; Stair, P. C.; Van Duyne, R. P., High-Resolution Distance Dependence Study of Surface-Enhanced Raman Scattering Enabled by Atomic Layer Deposition. *Nano Letters* **2016,** *16* (7), 4251-4259.

(36) Jensen, L.; Aikens, C. M.; Schatz, G. C., Electronic Structure Methods for Studying Surface-enhanced Raman Scattering. *Chem. Soc. Rev.* **2008,** *37* (5), 1061-1073.

(37) Gieseking, R. L.; Ratner, M. A.; Schatz, G. C., Theoretical Modeling of Voltage Effects and the Chemical Mechanism in Surface-enhanced Raman Scattering. *Faraday Discuss.* **2017,** *205*, 149-171.

(38) Wong, N. L., Surface-Enhanced Raman Spectroscopy (SERS): Advances in Single Molecule Detection and Elucidating the Chemical Enhancement Mechanism. *Ph. D. Thesis* **2018**.

(39) Moore, J. E.; Morton, S. M.; Jensen, L., Importance of Correctly Describing Charge-Transfer Excitations for Understanding the Chemical Effect in SERS. *The Journal of Physical Chemistry Letters* **2012,** *3* (17), 2470-2475.

(40) Carnegie, C.; Griffiths, J.; de Nijs, B.; Readman, C.; Chikkaraddy, R.; Deacon, W. M.; Zhang, Y.; Szabó, I.; Rosta, E.; Aizpurua, J.; Baumberg, J. J., Room-Temperature Optical Picocavities below 1 nm3 Accessing Single-Atom Geometries. *The Journal of Physical Chemistry Letters* **2018,** *9* (24), 7146-7151.

(41) Baranov, D. G.; Wersäll, M.; Cuadra, J.; Antosiewicz, T. J.; Shegai, T., Novel Nanostructures and Materials for Strong Light–Matter Interactions. *ACS Photonics* **2018,** *5* (1), 24-42.

(42) Vasa, P.; Lienau, C., Strong Light–Matter Interaction in Quantum Emitter/Metal Hybrid Nanostructures. *ACS Photonics* **2018,** *5* (1), 2-23.

(43) Wei, H.; Yan, X. H.; Niu, Y. J.; Li, Q.; Jia, Z. L.; Xu, H. X., Plasmon-Exciton Interactions: Spontaneous Emission and Strong Coupling. *Adv. Funct. Mater.* **2021**, 47.

(44) Luo, Y.; Zhao, J., Plasmon-exciton Interaction in Colloidally Fabricated Metal Nanoparticle-quantum emitter Nanostructures. *Nano Res.* **2019,** *12* (9), 2164-2171.

(45) Jaynes, E. T.; Cummings, F. W., Comparison of Quantum and Semiclassical Radiation Theories with Application to the Beam Maser. *Proceedings of the IEEE* **1963,** *51* (1), 89-109.

(46) Andreani, L. C.; Panzarini, G.; Gerard, J. M., Strong-coupling Regime for Quantum Boxes in Pillar Microcavities: Theory. *Phys. Rev. B* **1999,** *60* (19), 13276-13279.

(47) Koenderink, A. F., On the Use of Purcell Factors for Plasmon Antennas. *Opt. Lett.* **2010,** *35* (24), 4208-4210.

(48) Ribeiro, R. F.; Martínez-Martínez, L. A.; Du, M.; Campos-Gonzalez-Angulo, J.; Yuen-Zhou, J., Polariton Chemistry: Controlling Molecular Dynamics with Optical Cavities. *Chemical Science* **2018,** *9* (30), 6325-6339.

(49) Hümmer, T.; García-Vidal, F. J.; Martín-Moreno, L.; Zueco, D., Weak and Strong Coupling Regimes in Plasmonic QED. *Phys. Rev. B* **2013,** *87* (11), 115419.

(50) Anger, P.; Bharadwaj, P.; Novotny, L., Enhancement and Quenching of Single-Molecule Fluorescence. *Physical Review Letters* **2006,** *96* (11), 113002.

(51) Chen, Y. C.; Munechika, K.; Jen-La Plante, I.; Munro, A. M.; Skrabalak, S. E.; Xia, Y. N.; Ginger, D. S., Excitation enhancement of CdSe quantum dots by single metal nanoparticles. *Appl. Phys. Lett.* **2008,** *93* (5), 3.

(52) Purcell, E. M.; Torrey, H. C.; Pound, R. V., Resonance Absorption by Nuclear Magnetic Moments in a Solid. *Physical Review* **1946,** *69* (1-2), 37-38.

(53) Schatz, G. C.; Ratner, M. A., *Quantum Mechanics in Chemistry*. Courier Corporation: **2002**, p 59-98.

(54) Lakowicz, J. R., *Principles of fluorescence spectroscopy*. Springer science & business media: **2013**.

(55) Munechika, K.; Chen, Y.; Tillack, A. F.; Kulkarni, A. P.; Plante, I. J.-L.; Munro, A. M.; Ginger, D. S., Spectral Control of Plasmonic Emission Enhancement from Quantum Dots near Single Silver Nanoprisms. *Nano Letters* **2010,** *10* (7), 2598-2603.

(56) Yuan, H. F.; Khatua, S.; Zijlstra, P.; Yorulmaz, M.; Orrit, M., Thousand-fold Enhancement of Single-Molecule Fluorescence Near a Single Gold Nanorod. *Angew. Chem.-Int. Edit.* **2013,** *52* (4), 1217-1221.

(57) Ge, D.; Marguet, S.; Issa, A.; Jradi, S.; Nguyen, T. H.; Nahra, M.; Béal, J.; Deturche, R.; Chen, H.; Blaize, S.; Plain, J.; Fiorini, C.; Douillard, L.; Soppera, O.; Dinh, X. Q.; Dang, C.; Yang, X.; Xu, T.; Wei, B.; Sun, X. W.; Couteau, C.; Bachelot, R., Hybrid Plasmonic Nano-emitters with Controlled Single Quantum Emitter Positioning on the Local Excitation Field. *Nat. Commun.* **2020,** *11* (1), 3414.

(58) Zhang, H.; Li, M.; Wang, K.; Tian, Y.; Chen, J.-S.; Fountaine, K. T.; DiMarzio, D.; Liu, M.; Cotlet, M.; Gang, O., Polarized Single-Particle Quantum Dot Emitters through Programmable Cluster Assembly. *ACS Nano* **2020,** *14* (2), 1369-1378.

(59) Hoang, T. B.; Akselrod, G. M.; Mikkelsen, M. H., Ultrafast Room-Temperature Single Photon Emission from Quantum Dots Coupled to Plasmonic Nanocavities. *Nano Letters* **2016,** *16* (1), 270-275.

(60) Werschler, F.; Lindner, B.; Hinz, C.; Conradt, F.; Gumbsheimer, P.; Behovits, Y.; Negele, C.; de Roo, T.; Tzang, O.; Mecking, S.; Leitenstorfer, A.; Seletskiy, D. V., Efficient Emission Enhancement of Single CdSe/CdS/PMMA Quantum Dots through Controlled Near-Field Coupling to Plasmonic Bullseye Resonators. *Nano Letters* **2018,** *18* (9), 5396-5400.

(61) Tang, J.; Xia, J.; Fang, M.; Bao, F.; Cao, G.; Shen, J.; Evans, J.; He, S., Selective Far-field Addressing of Coupled Quantum Dots in a Plasmonic Nanocavity. *Nat. Commun.* **2018,** *9* (1), 1705.

(62) Langguth, L.; Punj, D.; Wenger, J.; Koenderink, A. F., Plasmonic Band Structure Controls Single-Molecule Fluorescence. *ACS Nano* **2013,** *7* (10), 8840-8848.

(63) Ji, B.; Giovanelli, E.; Habert, B.; Spinicelli, P.; Nasilowski, M.; Xu, X.; Lequeux, N.; Hugonin, J.-P.; Marquier, F.; Greffet, J.-J.; Dubertret, B., Non-Blinking Quantum Dot with a Plasmonic Nanoshell Resonator. *Nature Nanotechnology* **2015,** *10* (2), 170-175.

(64) Jin, Y.; Gao, X., Plasmonic Fluorescent Quantum Dots. *Nature Nanotechnology* **2009,** *4* (9), 571-576.

(65) Zhang, X.; Marocico, C. A.; Lunz, M.; Gerard, V. A.; Gun'ko, Y. K.; Lesnyak, V.; Gaponik, N.; Susha, A. S.; Rogach, A. L.; Bradley, A. L., Experimental and Theoretical Investigation of the Distance Dependence of Localized Surface Plasmon Coupled Förster Resonance Energy Transfer. *ACS Nano* **2014,** *8* (2), 1273-1283.

(66) Anderson, N. T.; Ren, S.; Chao, J.; Dinolfo, P. H.; Wang, X., Exploiting Plasmon-Mediated Energy Transfer To Enhance End-to-End Efficiency in a DNA Origami Energy Transfer Array. *ACS Appl. Nano Mater.* **2019,** *2* (9), 5563-5572.

(67) Ding, W. D.; Hsu, L. Y.; Schatz, G. C., Plasmon-Coupled Resonance Energy Transfer: A Real-time Electrodynamics Approach. *J. Chem. Phys.* **2017,** *146* (6), 11.

(68) Hsu, L.-Y.; Ding, W.; Schatz, G. C., Plasmon-Coupled Resonance Energy Transfer. *The Journal of Physical Chemistry Letters* **2017,** *8* (10), 2357-2367.

(69) Jeong, Y.; Schatz, G. C., Enhancement and Suppression of Resonance Energy Transfer Near Metal Nanoparticles. *The Journal of Physical Chemistry C* **2020,** *124* (37), 20589-20597.

(70) Tavis, M.; Cummings, F., The Exact Solution of N Two Level Systems Interacting with a Single Mode, Quantized Radiation Field. *Physics Letters A* **1967,** *25* (10), 714-715.

(71) Hakala, T. K.; Toppari, J. J.; Kuzyk, A.; Pettersson, M.; Tikkanen, H.; Kunttu, H.; Törmä, P., Vacuum Rabi Splitting and Strong-Coupling Dynamics for Surface-Plasmon Polaritons and Rhodamine 6G Molecules. *Physical Review Letters* **2009,** *103* (5), 053602.

(72) Rodriguez, S. R. K.; Feist, J.; Verschuuren, M. A.; Garcia Vidal, F. J.; Gómez Rivas, J., Thermalization and Cooling of Plasmon-Exciton Polaritons: Towards Quantum Condensation. *Physical Review Letters* **2013,** *111* (16), 166802.

(73) Pockrand, I.; Brillante, A.; Mobius, D., Exciton Surface-Plasmon Coupling: An Experimental Investigation. *J. Chem. Phys.* **1982,** *77* (12), 6289-6295.

(74) Wersäll, M.; Cuadra, J.; Antosiewicz, T. J.; Balci, S.; Shegai, T., Observation of Mode Splitting in Photoluminescence of Individual Plasmonic Nanoparticles Strongly Coupled to Molecular Excitons. *Nano Letters* **2017,** *17* (1), 551-558.

(75) Zengin, G.; Wersäll, M.; Nilsson, S.; Antosiewicz, T. J.; Käll, M.; Shegai, T., Realizing Strong Light-Matter Interactions between Single-Nanoparticle Plasmons and Molecular Excitons at Ambient Conditions. *Physical Review Letters* **2015,** *114* (15), 157401.

(76) Leng, H.; Szychowski, B.; Daniel, M.-C.; Pelton, M., Strong Coupling and Induced Transparency at Room Temperature with Single Quantum Dots and Gap Plasmons. *Nat. Commun.* **2018,** *9* (1), 4012.

(77) Xu, X.; Jin, S., Strong Coupling of Single Quantum Dots with Low-Refractive-Index/High-Refractive-Index Materials at Room Temperature. *Science Advances* **2020,** *6* (47), eabb3095.

(78) Zheng, D.; Zhang, S.; Deng, Q.; Kang, M.; Nordlander, P.; Xu, H., Manipulating Coherent Plasmon–Exciton Interaction in a Single Silver Nanorod on Monolayer WSe_2. *Nano Letters* **2017,** *17* (6), 3809-3814.

(79) Wen, J.; Wang, H.; Wang, W.; Deng, Z.; Zhuang, C.; Zhang, Y.; Liu, F.; She, J.; Chen, J.; Chen, H.; Deng, S.; Xu, N., Room-Temperature Strong Light–Matter Interaction with Active Control in Single Plasmonic Nanorod Coupled with Two-Dimensional Atomic Crystals. *Nano Letters* **2017,** *17* (8), 4689-4697.

(80) Chikkaraddy, R.; de Nijs, B.; Benz, F.; Barrow, S. J.; Scherman, O. A.; Rosta, E.; Demetriadou, A.; Fox, P.; Hess, O.; Baumberg, J. J., Single-Molecule Strong Coupling at Room Temperature in Plasmonic Nanocavities. *Nature* **2016,** *535* (7610), 127-130.

(81) Santhosh, K.; Bitton, O.; Chuntonov, L.; Haran, G., Vacuum Rabi Splitting in a Plasmonic Cavity at the Single Quantum Emitter Limit. *Nat. Commun.* **2016,** *7* (1), ncomms11823.

(82) Schwartz, T.; Hutchison, J. A.; Genet, C.; Ebbesen, T. W., Reversible Switching of Ultrastrong Light-Molecule Coupling. *Physical Review Letters* **2011,** *106* (19), 196405.

(83) Baudrion, A.-L.; Perron, A.; Veltri, A.; Bouhelier, A.; Adam, P.-M.; Bachelot, R., Reversible Strong Coupling in Silver Nanoparticle Arrays Using Photochromic Molecules. *Nano Letters* **2013,** *13* (1), 282-286.

(84) Lin, L.; Wang, M.; Wei, X.; Peng, X.; Xie, C.; Zheng, Y., Photoswitchable Rabi Splitting in Hybrid Plasmon–Waveguide Modes. *Nano Letters* **2016,** *16* (12), 7655-7663.

(85) Kato, F.; Minamimoto, H.; Nagasawa, F.; Yamamoto, Y. S.; Itoh, T.; Murakoshi, K., Active Tuning of Strong Coupling States between Dye Excitons and Localized Surface Plasmons via Electrochemical Potential Control. *ACS Photonics* **2018,** *5* (3), 788-796.

(86) Aberra Guebrou, S.; Symonds, C.; Homeyer, E.; Plenet, J. C.; Gartstein, Y. N.; Agranovich, V. M.; Bellessa, J., Coherent Emission from a Disordered Organic Semiconductor Induced by Strong Coupling with Surface Plasmons. *Physical Review Letters* **2012,** *108* (6), 066401.

(87) Shi, L.; Hakala, T. K.; Rekola, H. T.; Martikainen, J. P.; Moerland, R. J.; Törmä, P., Spatial Coherence Properties of Organic Molecules Coupled to Plasmonic Surface Lattice Resonances in the Weak and Strong Coupling Regimes. *Physical Review Letters* **2014,** *112* (15), 153002.

(88) Ramezani, M.; Le-Van, Q.; Halpin, A.; Gómez Rivas, J., Nonlinear Emission of Molecular Ensembles Strongly Coupled to Plasmonic Lattices with Structural Imperfections. *Physical Review Letters* **2018,** *121* (24), 243904.

(89) Vasa, P.; Wang, W.; Pomraenke, R.; Lammers, M.; Maiuri, M.; Manzoni, C.; Cerullo, G.; Lienau, C., Real-time Observation of Ultrafast Rabi Oscillations between Excitons and Plasmons in Metal Nanostructures with J-aggregates. *Nat. Photonics* **2013,** *7* (2), 128-132.

(90) Dulkeith, E.; Niedereichholz, T.; Klar, T. A.; Feldmann, J.; von Plessen, G.; Gittins, D. I.; Mayya, K. S.; Caruso, F., Plasmon Emission in Photoexcited Gold Nanoparticles. *Phys. Rev. B* **2004,** *70* (20), 205424.

(91) Li, X. G.; Xiao, D.; Zhang, Z. Y., Landau damping of quantum plasmons in metal nanostructures. *New J. Phys.* **2013,** *15*, 15.

(92) Fann, W. S.; Storz, R.; Tom, H. W. K.; Bokor, J., Electron Thermalization in Gold. *Phys. Rev. B* **1992,** *46* (20), 13592-13595.

(93) Manjavacas, A.; Liu, J. G.; Kulkarni, V.; Nordlander, P., Plasmon-Induced Hot Carriers in Metallic Nanoparticles. *ACS Nano* **2014,** *8* (8), 7630-7638.

(94) Del Fatti, N.; Voisin, C.; Achermann, M.; Tzortzakis, S.; Christofilos, D.; Vallée, F., Nonequilibrium electron dynamics in noble metals. *Phys. Rev. B* **2000,** *61* (24), 16956-16966.

(95) Neukirch, A. J.; Guo, Z.; Prezhdo, O. V., Time-Domain Ab Initio Study of Phonon-Induced Relaxation of Plasmon Excitations in a Silver Quantum Dot. *The Journal of Physical Chemistry C* **2012,** *116* (28), 15034-15040.

(96) Foerster, B.; Joplin, A.; Kaefer, K.; Celiksoy, S.; Link, S.; Sönnichsen, C., Chemical Interface Damping Depends on Electrons Reaching the Surface. *ACS Nano* **2017,** *11* (3), 2886-2893.

(97) Bora, T.; Zoepfl, D.; Dutta, J., Importance of Plasmonic Heating on Visible Light Driven Photocatalysis of Gold Nanoparticle Decorated Zinc Oxide Nanorods. *Sci Rep* **2016,** *6* (1), 26913.

(98) Mukherjee, S.; Libisch, F.; Large, N.; Neumann, O.; Brown, L. V.; Cheng, J.; Lassiter, J. B.; Carter, E. A.; Nordlander, P.; Halas, N. J., Hot Electrons Do the Impossible: Plasmon-Induced Dissociation of H2 on Au. *Nano Letters* **2013,** *13* (1), 240-247.

(99) Zhou, L.; Zhang, C.; McClain, M. J.; Manjavacas, A.; Krauter, C. M.; Tian, S.; Berg, F.; Everitt, H. O.; Carter, E. A.; Nordlander, P.; Halas, N. J., Aluminum Nanocrystals as a Plasmonic Photocatalyst for Hydrogen Dissociation. *Nano Letters* **2016,** *16* (2), 1478-1484.

(100) Mukherjee, S.; Zhou, L.; Goodman, A. M.; Large, N.; Ayala-Orozco, C.; Zhang, Y.; Nordlander, P.; Halas, N. J., Hot-Electron-Induced Dissociation of H_2 on Gold Nanoparticles Supported on SiO_2. *Journal of the American Chemical Society* **2014,** *136* (1), 64-67.

(101) Zhou, L. A.; Swearer, D. F.; Zhang, C.; Robatjazi, H.; Zhao, H. Q.; Henderson, L.; Dong, L. L.; Christopher, P.; Carter, E. A.; Nordlander, P.; Halas, N. J., Quantifying Hot Carrier and Thermal Contributions in Plasmonic Photocatalysis. *Science* **2018,** *362* (6410), 69-72.

(102) Boerigter, C.; Aslam, U.; Linic, S., Mechanism of Charge Transfer from Plasmonic Nanostructures to Chemically Attached Materials. *ACS Nano* **2016,** *10* (6), 6108-6115.

(103) Cortés, E.; Xie, W.; Cambiasso, J.; Jermyn, A. S.; Sundararaman, R.; Narang, P.; Schlücker, S.; Maier, S. A., Plasmonic Hot Electron Transport Drives Nano-localized Chemistry. *Nat. Commun.* **2017,** *8* (1), 14880.

(104) Choi, H.-K.; Park, W.-H.; Park, C.-G.; Shin, H.-H.; Lee, K. S.; Kim, Z. H., Metal-Catalyzed Chemical Reaction of Single Molecules Directly Probed by Vibrational Spectroscopy. *Journal of the American Chemical Society* **2016,** *138* (13), 4673-4684.

(105) Wang, F.; Li, C.; Chen, H.; Jiang, R.; Sun, L.-D.; Li, Q.; Wang, J.; Yu, J. C.; Yan, C.-H., Plasmonic Harvesting of Light Energy for Suzuki Coupling Reactions. *Journal of the American Chemical Society* **2013,** *135* (15), 5588-5601.

(106) Willets, K. A.; Van Duyne, R. P., Localized Surface Plasmon Resonance Spectroscopy and Sensing. *Annu. Rev. Phys. Chem.* **2007,** *58*, 267-297.

(107) Stiles, P. L.; Dieringer, J. A.; Shah, N. C.; Van Duyne, R. P., Surface-Enhanced Raman Spectroscopy. *Annu. Rev. Anal. Chem.* **2008,** *1*, 601-626.

(108) Wu, K.; Chen, J.; McBride, J. R.; Lian, T., Efficient hot-electron transfer by a plasmon-induced interfacial charge-transfer transition. *Science* **2015,** *349* (6248), 632-635.

(109) Du, L.; Furube, A.; Yamamoto, K.; Hara, K.; Katoh, R.; Tachiya, M., Plasmon-Induced Charge Separation and Recombination Dynamics in Gold−TiO_2 Nanoparticle Systems: Dependence on TiO_2 Particle Size. *The Journal of Physical Chemistry C* **2009,** *113* (16), 6454-6462.

(110) Christopher, P.; Xin, H. L.; Linic, S., Visible-light-enhanced catalytic oxidation reactions on plasmonic silver nanostructures. *Nat. Chem.* **2011,** *3* (6), 467-472.

(111) Böckmann, H.; Gawinkowski, S.; Waluk, J.; Raschke, M. B.; Wolf, M.; Kumagai, T., Near-Field Enhanced Photochemistry of Single Molecules in a Scanning Tunneling Microscope Junction. *Nano Letters* **2018,** *18* (1), 152-157.

(112) Zhan, C.; Wang, Z.-Y.; Zhang, X.-G.; Chen, X.-J.; Huang, Y.-F.; Hu, S.; Li, J.-F.; Wu, D.-Y.; Moskovits, M.; Tian, Z.-Q., Interfacial Construction of Plasmonic Nanostructures for the Utilization of the Plasmon-Excited Electrons and Holes. *Journal of the American Chemical Society* **2019,** *141* (20), 8053-8057.

(113) Kumari, G.; Zhang, X.; Devasia, D.; Heo, J.; Jain, P. K., Watching Visible Light-Driven CO2 Reduction on a Plasmonic Nanoparticle Catalyst. *ACS Nano* **2018,** *12* (8), 8330-8340.

(114) Kazuma, E.; Jung, J.; Ueba, H.; Trenary, M.; Kim, Y., Real-space and real-time observation of a plasmon-induced chemical reaction of a single molecule. *Science* **2018,** *360* (6388), 521-525.

(115) Yu, Y.; Wijesekara, K. D.; Xi, X.; Willets, K. A., Quantifying Wavelength-Dependent Plasmonic Hot Carrier Energy Distributions at Metal/Semiconductor Interfaces. *ACS Nano* **2019,** *13* (3), 3629-3637.

(116) Tesema, T. E.; Kafle, B.; Habteyes, T. G., Plasmon-Driven Reaction Mechanisms: Hot Electron Transfer versus Plasmon-Pumped Adsorbate Excitation. *The Journal of Physical Chemistry C* **2019,** *123* (14), 8469-8483.

(117) Boerigter, C.; Campana, R.; Morabito, M.; Linic, S., Evidence and implications of direct charge excitation as the dominant mechanism in plasmon-mediated photocatalysis. *Nat. Commun.* **2016,** *7*, 9.

(118) Brandt, N. C.; Keller, E. L.; Frontiera, R. R., Ultrafast Surface-Enhanced Raman Probing of the Role of Hot Electrons in Plasmon-Driven Chemistry. *J. Phys. Chem. Lett.* **2016,** *7* (16), 3179-3185.

(119) Besteiro, L. V.; Govorov, A. O., Amplified Generation of Hot Electrons and Quantum Surface Effects in Nanoparticle Dimers with Plasmonic Hot Spots. *J. Phys. Chem. C* **2016,** *120* (34), 19329-19339.

(120) Kumar, P. V.; Rossi, T. P.; Marti-Dafcik, D.; Reichmuth, D.; Kuisma, M.; Erhart, P.; Puska, M. J.; Norris, D. J., Plasmon-Induced Direct Hot-Carrier Transfer at Metal–Acceptor Interfaces. *ACS Nano* **2019,** *13* (3), 3188-3195.

(121) Zhang, J.; Guan, M.; Lischner, J.; Meng, S.; Prezhdo, O. V., Coexistence of Different Charge-Transfer Mechanisms in the Hot-Carrier Dynamics of Hybrid Plasmonic Nanomaterials. *Nano Letters* **2019,** *19* (5), 3187-3193.

(122) Christopher, P.; Moskovits, M., Hot Charge Carrier Transmission from Plasmonic Nanostructures. In *Annual Review of Physical Chemistry, Vol 68*, Johnson, M. A.; Martinez, T. J., Eds. Annual Reviews: Palo Alto, **2017**; Vol. 68, pp 379-398.

(123) Evers, F.; Rakete, C.; Watanabe, K.; Menzel, D.; Freund, H. J., Two-photon photoemission from silver nanoparticles on thin alumina films: Role of plasmon excitation. *Surf. Sci.* **2005,** *593* (1-3), 43-48.

(124) Brown, A. M.; Sundararaman, R.; Narang, P.; Goddard, W. A.; Atwater, H. A., Nonradiative Plasmon Decay and Hot Carrier Dynamics: Effects of Phonons, Surfaces, and Geometry. *ACS Nano* **2016,** *10* (1), 957-966.

(125) Zhao, J.; Nguyen, S. C.; Ye, R.; Ye, B.; Weller, H.; Somorjai, G. A.; Alivisatos, A. P.; Toste, F. D., A Comparison of Photocatalytic Activities of Gold Nanoparticles Following Plasmonic and Interband Excitation and a Strategy for Harnessing Interband Hot Carriers for Solution Phase Photocatalysis. *ACS Central Science* **2017,** *3* (5), 482-488.

(126) Zhang, Y.; He, S.; Guo, W.; Hu, Y.; Huang, J.; Mulcahy, J. R.; Wei, W. D., Surface-Plasmon-Driven Hot Electron Photochemistry. *Chemical Reviews* **2018,** *118* (6), 2927-2954.

(127) Kazuma, E.; Kim, Y., Mechanistic Studies of Plasmon Chemistry on Metal Catalysts. *Angew. Chem.-Int. Edit.* **2019,** *58* (15), 4800-4808.

(128) Crampton, K. T.; Fast, A.; Potma, E. O.; Apkarian, V. A., Junction Plasmon Driven Population Inversion of Molecular Vibrations: A Picosecond Surface-Enhanced Raman Spectroscopy Study. *Nano Letters* **2018,** *18* (9), 5791-5796.

(129) Golubev, A. A.; Khlebtsov, B. N.; Rodriguez, R. D.; Chen, Y.; Zahn, D. R. T., Plasmonic Heating Plays a Dominant Role in the Plasmon-Induced Photocatalytic Reduction of 4-Nitrobenzenethiol. *The Journal of Physical Chemistry C* **2018,** *122* (10), 5657-5663.

(130) Yu, Y.; Sundaresan, V.; Willets, K. A., Hot Carriers versus Thermal Effects: Resolving the Enhancement Mechanisms for Plasmon-Mediated Photoelectrochemical Reactions. *The Journal of Physical Chemistry C* **2018,** *122* (9), 5040-5048.

(131) Sprague-Klein, E. A.; McAnally, M. O.; Zhdanov, D. V.; Zrimsek, A. B.; Apkarian, V. A.; Seideman, T.; Schatz, G. C.; Van Duyne, R. P., Observation of Single Molecule Plasmon-Driven Electron Transfer in Isotopically Edited 4,4′-Bipyridine Gold Nanosphere Oligomers. *Journal of the American Chemical Society* **2017,** *139* (42), 15212-15221.

(132) Sprague-Klein, E. A.; Negru, B.; Madison, L. R.; Coste, S. C.; Rugg, B. K.; Felts, A. M.; McAnally, M. O.; Banik, M.; Apkarian, V. A.; Wasielewski, M. R.; Ratner, M. A.; Seideman, T.; Schatz, G. C.; Van Duyne, R. P., Photoinduced Plasmon-Driven Chemistry in trans-1,2-Bis(4-pyridyl)ethylene Gold Nanosphere Oligomers. *Journal of the American Chemical Society* **2018,** *140* (33), 10583-10592.

(133) Qi, Y.; Brasiliense, V.; Ueltschi, T. W.; Park, J. E.; Wasielewski, M. R.; Schatz, G. C.; Van Duyne, R. P., Plasmon-Driven Chemistry in Ferri-/Ferrocyanide Gold Nanoparticle Oligomers: A SERS Study. *Journal of the American Chemical Society* **2020,** *142* (30), 13120-13129.

(134) Stavytska-Barba, M.; Salvador, M.; Kulkarni, A.; Ginger, D. S.; Kelley, A. M., Plasmonic Enhancement of Raman Scattering from the Organic Solar Cell Material P3HT/PCBM by Triangular Silver Nanoprisms. *The Journal of Physical Chemistry C* **2011,** *115* (42), 20788-20794.

(135) Kuzmany, H.; Pfeiffer, R.; Hulman, M.; Kramberger, C., Raman spectroscopy of fullerenes and fullerene-nanotube composites. *Philos. Trans. R. Soc. A-Math. Phys. Eng. Sci.* **2004,** *362* (1824), 2375-2406.

(136) Dresselhaus, M. S.; Dresselhaus, G.; Eklund, P. C., Raman scattering in fullerenes. *J. Raman Spectrosc.* **1996,** *27* (3-4), 351-371.

(137) McGlashen, M. L.; Blackwood, M. E.; Spiro, T. G., Resonance Raman spectroelectrochemistry of the fullerene C_{60} radical anion. *Journal of the American Chemical Society* **1993,** *115* (5), 2074-2075.

(138) Reed, C. A.; Bolskar, R. D., Discrete Fulleride Anions and Fullerenium Cations. *Chemical Reviews* **2000,** *100* (3), 1075-1120.

(139) He, Y. J.; Li, Y. F., Fullerene derivative acceptors for high performance polymer solar cells. *Phys. Chem. Chem. Phys.* **2011,** *13* (6), 1970-1983.

(140) Xie, Q.; Arias, F.; Echegoyen, L., Electrochemically-reversible, single-electron oxidation of C_{60} and C_{70}. *Journal of the American Chemical Society* **1993,** *115* (21), 9818-9819.

(141) Schoenlein, R. W.; Lin, W. Z.; Fujimoto, J. G.; Eesley, G. L., Femtosecond studies of nonequilibrium electronic processes in metals. *Physical Review Letters* **1987,** *58* (16), 1680-1683.

(142) Pozzi, E. A.; Zrimsek, A. B.; Lethiec, C. M.; Schatz, G. C.; Hersam, M. C.; Van Duyne, R. P., Evaluating Single-Molecule Stokes and Anti-Stokes SERS for Nanoscale Thermometry. *The Journal of Physical Chemistry C* **2015,** *119* (36), 21116-21124.

(143) Maher, R. C.; Etchegoin, P. G.; Le Ru, E. C.; Cohen, L. F., A Conclusive Demonstration of Vibrational Pumping under Surface Enhanced Raman Scattering Conditions. *The Journal of Physical Chemistry B* **2006,** *110* (24), 11757-11760.

(144) Negru, B.; McAnally, M. O.; Mayhew, H. E.; Ueltschi, T. W.; Peng, L.; Sprague-Klein, E. A.; Schatz, G. C.; Van Duyne, R. P., Fabrication of Gold Nanosphere Oligomers for Surface-Enhanced Femtosecond Stimulated Raman Spectroscopy. *The Journal of Physical Chemistry C* **2017,** *121* (48), 27004-27008.

(145) Soler, J. M.; Artacho, E.; Gale, J. D.; Garcia, A.; Junquera, J.; Ordejon, P.; Sanchez-Portal, D., The SIESTA method for ab initio order-N materials simulation. *J. Phys.-Condes. Matter* **2002,** *14* (11), 2745-2779.

(146) Valiev, M.; Bylaska, E. J.; Govind, N.; Kowalski, K.; Straatsma, T. P.; Van Dam, H. J. J.; Wang, D.; Nieplocha, J.; Apra, E.; Windus, T. L.; de Jong, W., NWChem: A comprehensive and scalable open-source solution for large scale molecular simulations. *Comput. Phys. Commun.* **2010,** *181* (9), 1477-1489.

(147) Te Velde, G.; Bickelhaupt, F. M.; Baerends, E. J.; Guerra, C. F.; Van Gisbergen, S. J. A.; Snijders, J. G.; Ziegler, T., Chemistry with ADF. *J. Comput. Chem.* **2001,** *22* (9), 931-967.

(148) Coe, S.; Woo, W.-K.; Bawendi, M.; Bulović, V., Electroluminescence from Single Monolayers of Nanocrystals in Molecular Organic Devices. *Nature* **2002,** *420* (6917), 800-803.

(149) Shirasaki, Y.; Supran, G. J.; Bawendi, M. G.; Bulović, V., Emergence of Colloidal Quantum-Dot Light-emitting Technologies. *Nat. Photonics* **2013,** *7* (1), 13-23.

(150) Gur, I.; Fromer, N. A.; Geier, M. L.; Alivisatos, A. P., Air-Stable All-Inorganic Nanocrystal Solar Cells Processed from Solution. *Science* **2005,** *310* (5747), 462-465.

(151) Swarnkar, A.; Marshall, A. R.; Sanehira, E. M.; Chernomordik, B. D.; Moore, D. T.; Christians, J. A.; Chakrabarti, T.; Luther, J. M., Quantum dot-Induced Phase Stabilization of α-$CsPbI_3$ Perovskite for High-efficiency Photovoltaics. *Science* **2016,** *354* (6308), 92-95.

(152) Park, Y.-S.; Roh, J.; Diroll, B. T.; Schaller, R. D.; Klimov, V. I., Colloidal Quantum Dot Lasers. *Nature Reviews Materials* **2021,** *6* (5), 382-401.

(153) Santori, C.; Fattal, D.; Vučković, J.; Solomon, G. S.; Yamamoto, Y., Indistinguishable Photons from a Single-Photon Device. *Nature* **2002,** *419* (6907), 594-597.

(154) Thyrrestrup, H.; Kiršanskė, G.; Le Jeannic, H.; Pregnolato, T.; Zhai, L.; Raahauge, L.; Midolo, L.; Rotenberg, N.; Javadi, A.; Schott, R.; Wieck, A. D.; Ludwig, A.; Löbl, M. C.; Söllner, I.; Warburton, R. J.; Lodahl, P., Quantum Optics with Near-Lifetime-Limited Quantum-Dot Transitions in a Nanophotonic Waveguide. *Nano Letters* **2018,** *18* (3), 1801-1806.

(155) Schnauber, P.; Singh, A.; Schall, J.; Park, S. I.; Song, J. D.; Rodt, S.; Srinivasan, K.; Reitzenstein, S.; Davanco, M., Indistinguishable Photons from Deterministically Integrated Single Quantum Dots in Heterogeneous GaAs/Si3N4 Quantum Photonic Circuits. *Nano Letters* **2019,** *19* (10), 7164-7172.

(156) Nirmal, M.; Dabbousi, B. O.; Bawendi, M. G.; Macklin, J. J.; Trautman, J. K.; Harris, T. D.; Brus, L. E., Fluorescence Intermittency in Single Cadmium Selenide Nanocrystals. *Nature* **1996,** *383* (6603), 802-804.

(157) Empedocles, S. A.; Bawendi, M. G., Influence of Spectral Diffusion on the Line Shapes of Single CdSe Nanocrystallite Quantum Dots. *The Journal of Physical Chemistry B* **1999,** *103* (11), 1826-1830.

(158) Gomez, D. E.; van Embden, J.; Mulvaney, P., Spectral Diffusion of Single Semiconductor Nanocrystals: The Influence of the Dielectric Environment. *Appl. Phys. Lett.* **2006,** *88* (15), 3.

(159) Empedocles, S. A.; Bawendi, M. G., Quantum-Confined Stark Effect in Single CdSe Nanocrystallite Quantum Dots. *Science* **1997,** *278* (5346), 2114-2117.

(160) Chen, Y.; Vela, J.; Htoon, H.; Casson, J. L.; Werder, D. J.; Bussian, D. A.; Klimov, V. I.; Hollingsworth, J. A., "Giant" Multishell CdSe Nanocrystal Quantum Dots with Suppressed Blinking. *Journal of the American Chemical Society* **2008,** *130* (15), 5026-5027.

(161) Hohng, S.; Ha, T., Near-Complete Suppression of Quantum Dot Blinking in Ambient Conditions. *Journal of the American Chemical Society* **2004,** *126* (5), 1324-1325.

(162) Karan, N. S.; Keller, A. M.; Sampat, S.; Roslyak, O.; Arefin, A.; Hanson, C. J.; Casson, J. L.; Desireddy, A.; Ghosh, Y.; Piryatinski, A.; Iyer, R.; Htoon, H.; Malko, A. V.; Hollingsworth, J. A., Plasmonic Giant Quantum Dots: Hybrid Nanostructures for Truly Simultaneous Optical Imaging, Photothermal Effect and Thermometry. *Chemical Science* **2015,** *6* (4), 2224-2236.

(163) Kodaimati, M. S.; Lian, S. C.; Schatz, G. C.; Weiss, E. A., Energy Transfer-Enhanced Photocatalytic Reduction of Protons within Quantum Dot Light-Harvesting-Catalyst Assemblies. *Proc. Natl. Acad. Sci. U. S. A.* **2018,** *115* (33), 8290-8295.

(164) Darbandi, M.; Thomann, R.; Nann, T., Single Quantum Dots in Silica Spheres by Microemulsion Synthesis. *Chemistry of Materials* **2005,** *17* (23), 5720-5725.

(165) Hohenester, U.; Trügler, A., MNPBEM – A Matlab Toolbox for the Simulation of Plasmonic Nanoparticles. *Comput. Phys. Commun.* **2012,** *183* (2), 370-381.

(166) Rudin, S.; Reinecke, T. L., Oscillator Model for Vacuum Rabi Splitting in Microcavities. *Phys. Rev. B* **1999,** *59* (15), 10227-10233.

(167) Vahala, K. J., Optical Microcavities. *Nature* **2003,** *424* (6950), 839-846.

(168) Akahane, Y.; Asano, T.; Song, B.-S.; Noda, S., High-Q Photonic Nanocavity in a Two-Dimensional Photonic Crystal. *Nature* **2003,** *425* (6961), 944-947.

(169) Reithmaier, J. P.; Sęk, G.; Löffler, A.; Hofmann, C.; Kuhn, S.; Reitzenstein, S.; Keldysh, L. V.; Kulakovskii, V. D.; Reinecke, T. L.; Forchel, A., Strong Coupling in a Single Quantum Dot–Semiconductor Microcavity System. *Nature* **2004,** *432* (7014), 197-200.

(170) Hennessy, K.; Badolato, A.; Winger, M.; Gerace, D.; Atatüre, M.; Gulde, S.; Fält, S.; Hu, E. L.; Imamoğlu, A., Quantum Nature of a Strongly Coupled Single Quantum Dot–Cavity System. *Nature* **2007,** *445* (7130), 896-899.

(171) Balci, S., Ultrastrong Plasmon-Exciton Coupling in Metal Nanoprisms with J-aggregates. *Opt. Lett.* **2013,** *38* (21), 4498-4501.

(172) Zengin, G.; Johansson, G.; Johansson, P.; Antosiewicz, T. J.; Käll, M.; Shegai, T., Approaching the Strong Coupling Limit in Single Plasmonic Nanorods Interacting with J-aggregates. *Sci Rep* **2013,** *3* (1), 3074.

(173) Balci, S.; Kucukoz, B.; Balci, O.; Karatay, A.; Kocabas, C.; Yaglioglu, G., Tunable Plexcitonic Nanoparticles: A Model System for Studying Plasmon–Exciton Interaction from the Weak to the Ultrastrong Coupling Regime. *ACS Photonics* **2016,** *3* (11), 2010-2016.

(174) Yan, X.; Wei, H., Strong Plasmon–Exciton Coupling between Lithographically Defined Single Metal Nanoparticles and Monolayer WSe_2. *Nanoscale* **2020,** *12* (17), 9708-9716.

(175) Pala, R. A.; Shimizu, K. T.; Melosh, N. A.; Brongersma, M. L., A Nonvolatile Plasmonic Switch Employing Photochromic Molecules. *Nano Letters* **2008,** *8* (5), 1506-1510.

(176) Nan, F.; Ding, S.-J.; Ma, L.; Cheng, Z.-Q.; Zhong, Y.-T.; Zhang, Y.-F.; Qiu, Y.-H.; Li, X.; Zhou, L.; Wang, Q.-Q., Plasmon Resonance Energy Transfer and Plexcitonic Solar Cell. *Nanoscale* **2016,** *8* (32), 15071-15078.

(177) Hutchison, J. A.; Schwartz, T.; Genet, C.; Devaux, E.; Ebbesen, T. W., Modifying Chemical Landscapes by Coupling to Vacuum Fields. *Angewandte Chemie International Edition* **2012,** *51* (7), 1592-1596.

(178) Galego, J.; Garcia-Vidal, F. J.; Feist, J., Suppressing Photochemical Reactions with Quantized Light Fields. *Nat. Commun.* **2016,** *7* (1), 13841.

(179) Tavis, M.; Cummings, F. W., Approximate Solutions for an N-Molecule-Radiation-Field Hamiltonian. *Physical Review* **1969,** *188* (2), 692-695.

(180) Myers, A. B.; Harris, R. A.; Mathies, R. A., Resonance Raman Excitation Profiles of Bacteriorhodopsin. *J. Chem. Phys.* **1983,** *79* (2), 603-613.

(181) Inagaki, F.; Tasumi, M.; Miyazawa, T., Excitation Profile of the Resonance Raman Effect of β-carotene. *Journal of Molecular Spectroscopy* **1974,** *50* (1-3), 286-303.

(182) Zhao, J.; Dieringer, J. A.; Zhang, X.; Schatz, G. C.; Van Duyne, R. P., Wavelength-Scanned Surface-Enhanced Resonance Raman Excitation Spectroscopy. *The Journal of Physical Chemistry C* **2008,** *112* (49), 19302-19310.

(183) Dieringer, J. A.; Wustholz, K. L.; Masiello, D. J.; Camden, J. P.; Kleinman, S. L.; Schatz, G. C.; Van Duyne, R. P., Surface-Enhanced Raman Excitation Spectroscopy of a Single Rhodamine 6G Molecule. *Journal of the American Chemical Society* **2009,** *131* (2), 849-854.

(184) Aherne, D.; Ledwith, D. M.; Gara, M.; Kelly, J. M., Optical Properties and Growth Aspects of Silver Nanoprisms Produced by a Highly Reproducible and Rapid Synthesis at Room Temperature. *Adv. Funct. Mater.* **2008,** *18* (14), 2005-2016.

(185) Coles, D. M.; Meijer, A. J. H. M.; Tsoi, W. C.; Charlton, M. D. B.; Kim, J.-S.; Lidzey, D. G., A Characterization of the Raman Modes in a J-Aggregate-Forming Dye: A Comparison between Theory and Experiment. *The Journal of Physical Chemistry A* **2010,** *114* (44), 11920-11927.

Appendix A: Blinking and Spectral Diffusion of single CdSe Nanoplatelets at Room Temperature

Adapted from: Irgen-Gioro, S.*; Wu, Y.*; López-Arteaga, R.; Padgaonkar, S.; Olding, J. N.; Weiss, E. A., *The Journal of Physical Chemistry C* **2021,** *125* (24), 13485-13492.

*These authors contributed equally to this work.

A.1. Chapter summary

Intermittent periods of low light emission ("blinking") and time-dependent emission spectra (spectral diffusion, SD) have proven major obstacles to the adoption of colloidal semiconductor nanocrystals as quantum emitters. This work utilizes spectral correlations to access this faster timescale and determines that, for quasi-2D CdSe nanoplatelets (NPLs) and CdSe/CdS core/shell NPLs, blinking occurs on timescales from 100 μs to seconds but is only accompanied by SD on a timescale of seconds and slower, where blinking and SD are correlated. This result implies that shorter-timescale blinking is due to an equilibrium between dark and bright states with a shared, uncharged ground state, while longer-timescale blinking is due to an equilibrium between two distinct emissive states, an exciton and a trion.

A.2. Introduction

Although the ability to support charge transfer states or perform free carrier generation is not unique to colloidal nanocrystals, the ability to relax these excess charges without oxidation or photodamage is one of primary reasons CdSe quantum dots (QDs) have been robustly observed to have high single photon emission purity, even at room temperature, for the past two decades.[1] In this sense, colloidal QD systems provide an opportunity for solution processing of quantum emitters, lowering the barrier of accessibility for demonstrations of quantum optics phenomena, and offering new chemical tools to modify the next generation of quantum technologies that leverage single photons. However, the excess charges have also been linked to intensity intermittency (“blinking”) that create instability of the number of counts per second of single photons being emitted.[2-3] Previous electrochemical studies have demonstrated applying voltages that promote electron injection increase blinking and shorten photoluminescence lifetimes, rationalized with QD's fast non-radiative Auger for charged excitons (trions) out-competing radiative recombination.[4]

When observing quantum emission at the timescale of radiative recombination (<1 us), emission is anti-bunched, meaning photons are emitted one at a time as only one cycle of excitation and subsequent relaxation to the ground state has occurred. Each excited exciton may relax through the excited state fine structure differently, exploring the multitude of pathways between a fixed set of electronic states. However, it is clear that the distribution of blinking dynamics that occur on a much longer timescale (1 μs – 100 s) cannot be explained with a simple kinetic model with probabilistic emission from the numerous radiative and non-radiative pathways available in a fixed set of states. Blinking's probability of high intensity vs low intensity has been observed to follow a power-law dependency over 9 orders of magnitude, yielding no set characteristic time.[5] Numerous methods have been put forward explaining how subsequent emission events, whether separated by 1 cycle or 10^9 cycles of emission, may be subject to differing electronic structures, but there is no consensus yet.

One piece of evidence that is still lacking is how spectral diffusion (SD) is connected to blinking since the presence of an excess charge, invoked in numerous explanations of blinking, should induce a Stark shift in the exciton energies, modifying the emission.[6-7] Intensity correlations can be observed at all timescales fairly easily, as fast single photon detectors paired with fast electronics can record the timing of every emission event with picosecond accuracy. Fluctuations of the emission spectra are harder to capture at a fast timescale since the traditional method of using a spectrograph or monochromator inherently requires binning over time of numerous photons to build up a spectrum.[8-9] One approach to overcome this limitation is to convert spectral fluctuations into intensity fluctuations. A simple version of this idea can be implemented by using two single photon detectors, each coupled to a monochromator tuned to the red or blue side of the emission spectra. Thus, changes to the emission spectrum bias the intensity to have a higher probability on one detector versus the other. Alternatively, spectral information can be introduced with an interferometer.[10] The capacity for single photons to interfere with themselves in an interferometer defies the semiclassical description of light and is related to the property of photon indistinguishability.[11] One particularly powerful technique called Photon Correlation Fourier Spectroscopy (PCFS) utilizes the cross correlation between spectrally biased detectors at the output of a dithered Michaelson interferometer to extract the average linewidth of two photons separated by a time difference τ.[12-13] Introduced over a decade ago, PCFS has been routinely applied to study how linewidths evolve as a function of τ and to observe sub-SD diffusion homogeneous linewidths, relevant for understanding the amount of exciton-phonon broadening that may limit indistinguishability.[14-16]

Our study investigates SD in relation to blinking dynamics in both unshelled and shelled nanoplatelets, which have excitons confined in just one dimension and have relatively slow non-radiative Auger rates as compared to quantum dots confined in 3D. Our study spans timescales ranging from sub-us to 10’s of s as we investigate the link between blinking and SD. We find that SD does not occur on fast timescales, but only begins to affect emission on the 1s timescale. We found that blinking still is observed at fast timescales (1 μs- 1 ms), suggesting the two processes have different origins. Since SD is a major hinderance to application of colloidal nanocrystals to quantum optics applications, the large span of timescales that have stable emission also points out that applications utilizing single photons at a timescale faster than ~1s need not worry about a rapidly shifting emission spectrum. While there may exist multiple emitting states of room temperature nanocrystal emitters, the lack of subsequent SD invites hope that future work in engineering the exciton fine structure to have lifetime-limited lifetimes will not be in vain and destroyed by rapid SD.

A.3 Results and Discussion

We synthesized 4- or 5-monolayer (4ML and 5ML) CdSe core-only NPLs, and 4ML/1ML core/shell CdSe/CdS NPLs using the colloidal atomic layer deposition method.[17] **Figure 1A** shows the ensemble absorption and emission spectra of the NPLs dispersed in hexane and a transmission electron micrograph of the core/shell NPLs. The CdS shell induces a strong bathochromic shift of the light-hole and heavy-hole transitions in the absorption spectra due to an increase in the total NPL thickness, while also broadening the emission spectrum of the 4ML NPL from 56 meV to 78 meV. The larger linewidth in core/shell NPLs has previously been attributed to coupling of the exciton to the phonon modes of the CdS shell.[18]

We conducted all of the measurements described below on single emitters. We diluted the NPLs to ~1 nM, drop-cast them onto a clean coverslip, and studied them with a homebuilt confocal microscope. Each potential target emitter is confirmed to be a single emitter with the standard Hanbury-Brown-Twiss experiment. **Figure 1B** shows an example of the antibunching behavior of the second-order correlation function $g^{(2)}$ of a single 4ML NPL. Verification of a single photon emitter requires a $g^{(2)}(\tau = 0) < 0.5$, with an ideal single photon emitter having a $g^{(2)}(0) = 0$. Here, the value of $g^{(2)}(\tau = 0) = 0.2$ suggests that the studied sample is a well-isolated single

NPL and a good candidate for further monitoring of blinking and SD. The residual is due to a high probability of bi-exciton generation in NPL.[19] **Figures 1C,D** show representative traces (additional traces in the SI) of emission intensity *vs*. time (binning the total number of counts every 10 ms for a total of 300 s) for a core-only NPL and a core/shell NPL, respectively. To the right of the time trace, the distribution of intensities is shown. Consistent with previous reports for QDs, the core-only sample spends 35% of time in the "on" state, while the core/shell NPL emits light nearly constantly (98% on) with transient moments of blinking. If blinking occurs faster than the 10 ms bin duration, the number of counts will be lowered for that time point. Thus, the reason for the

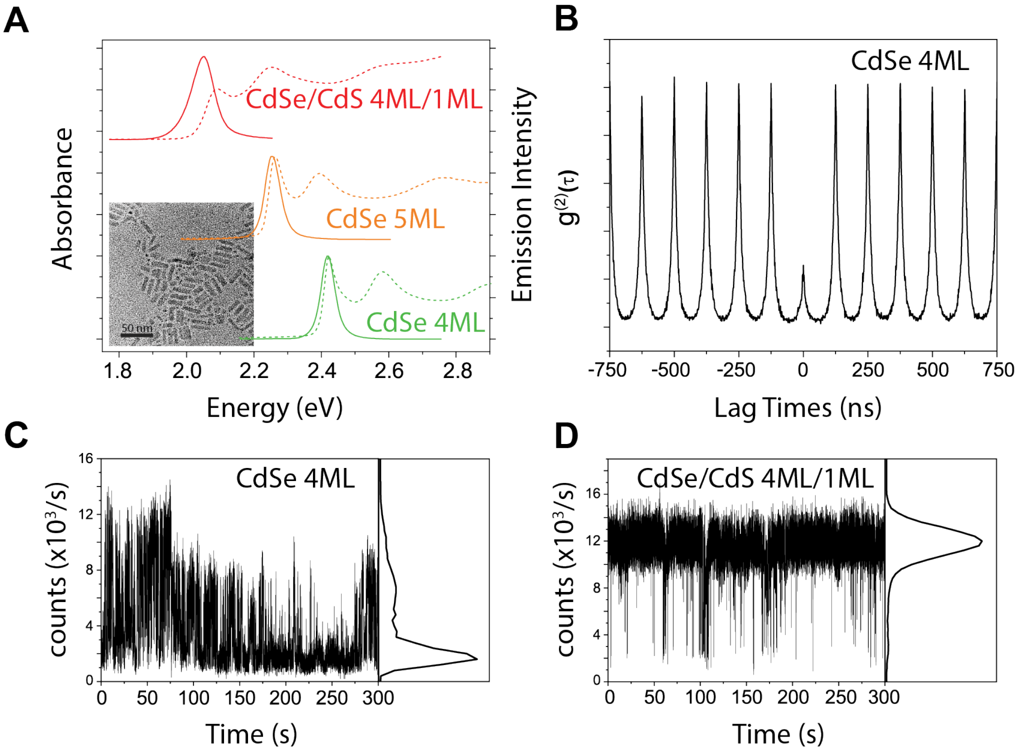

Figure 1. (**A**) Solution-phase absorption (dashed) and emission (solid) spectra of ensembles of CdSe 4ML, CdSe 5ML and CdSe/CdS 4ML/1ML NPLs in hexane, normalized to the band-edge peak. Inset: TEM of CdSe/CdS 4ML/1ML NPLs; the scalebar is 50 nm. (**B**) Second-order correlation function $g^{(2)}$ of the emission of a single core-only 4ML NPL. (**C,D**) Emission intensity time traces for a single CdSe core-only NPL (**C**) and a CdSe/CdS core/shell NPL (**D**), and accompanying intensity distributions.

distribution of intensities for **Figure 1C**, as opposed to a more step-like intensity distribution, is blinking faster than 10 ms.

We first monitor the SD of a single particle using the conventional method of directing the emission to a spectrograph paired with a sensitive sCMOS camera and recording the emission spectrum every 500 ms for 600 s, see the SI for details. **Figure 2A** shows SD for a single core/shell NPL. On this 1 s timescale, the peak energy of emission increases as the intensity of the emission increases, **Figure 2B**. The intensity and peak position are also correlated with emission linewidth:

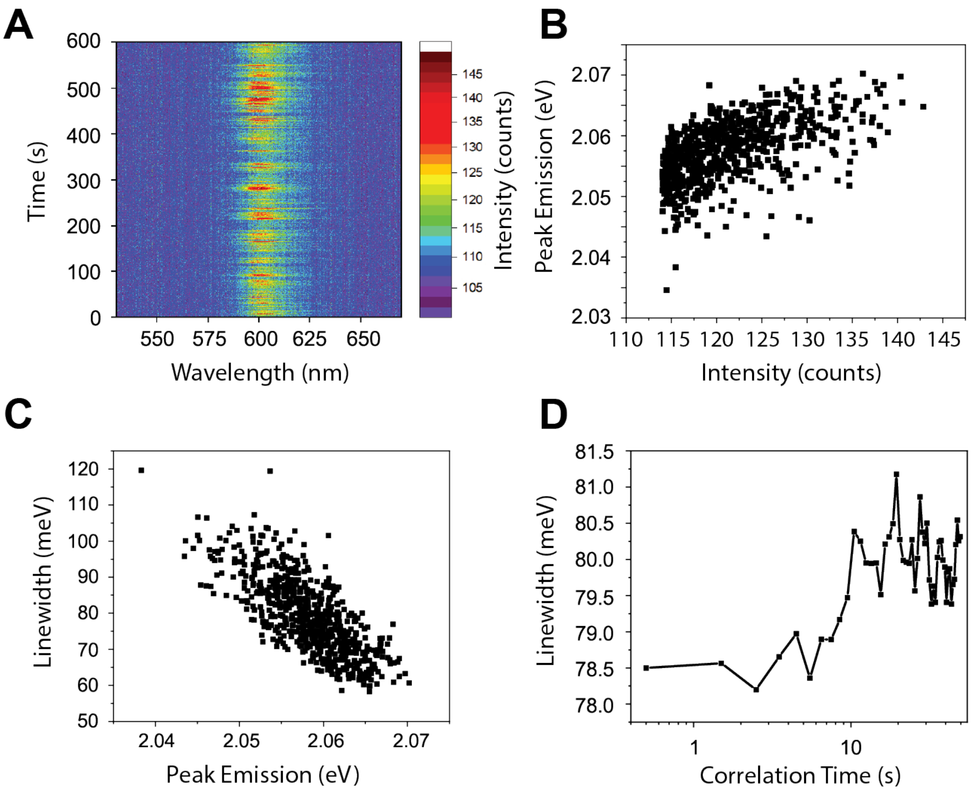

Figure 2. Slow spectral diffusion of 4ML/1ML core/shell CdSe/CdS NPLs. (**A**) Emission spectra taken every 500 ms. (**B**) Correlation between linewidth and peak emission. Intense peaks are blue-shifted relative to less intense peaks. (**C**) Correlation between Gaussian linewidth and center energy of the emission peak. (**D**) The calculated effective emission linewidth σ_{eff} at different correlation times τ giving the timescale of SD.

bathochromic shifts in the peak energy are coincident with broadening of the linewidth, and hypsochromic shifts are coincident with narrowing of the linewidth, **Figure 2C**. The correlation between emission intensity, peak position, and linewidth is the first evidence for a scenario where multiple emissive species – presumably an exciton and a trion – within a single particle are responsible for the observed blinking and SD dynamics on this timescale.

To more accurately specify the timescales on which SD is occurring, we use the data in **Figure 2A** to calculate the spectral correlation $p(\zeta, \tau) = \left\langle \int s(\omega, t) s(\omega + \zeta, t + \tau) d\omega \right\rangle$ of this emission, where $\langle \ldots \rangle$ denotes time averaging, $s(\omega, t)$ is the single-particle spectrum at time t, and ζ is the energy displacement between two spectra. The spectral correlation reveals how similar two spectra separated by the correlation lag time τ are in energy, ζ. The calculation of correlation allows us to quantify SD by averaging over all recorded events separated by a time difference τ, and thereby increase the accuracy of the calculation by collecting signal for a longer time. From the spectral correlation, we extract an effective linewidth, $\sigma_{eff}(\tau)$, which is how broad a static Gaussian function would need to be to generate the spectral correlation at a given τ (see the SI for details); a change $\sigma_{eff}(\tau)$ indicates SD. **Figure 2D** is a plot of σ_{eff} vs. lag time τ for a core/shell NPL. The effective linewidth is quite flat on the 1 s timescale but starts to rise as lag times approach 10 s. This result shows that, on average, emitted photons separated by 1 s are similar spectrally, but photons separated by 10s of seconds are likely to have different spectra. Although limited by the acquisition speed of the method, the spectral correlation plot shows that SD appears to only begin to occur on a ~1 s timescale.

To confirm that SD is not occurring on timescales faster than those plotted in **Figure 3D** (*i.e.*, the microsecond-to-second timescale), we convert spectral fluctuations into intensity fluctuations.

In this experiment, we use two single photon detectors, where, through the use of spectral filters, one detector is sensitive to the low-energy side of the NPL's emission spectrum and other is sensitive to the high-energy side, **Figure 3A**.[20] The total emission spectra of a single core/shell NPL and the spectra after spectral filtering are shown in **Figure 3B**. When there is no SD, the intensities on the detectors are correlated; the total counts on each of the two detectors increase and decrease together with the overall intensity fluctuations of the emitter, and the cross-

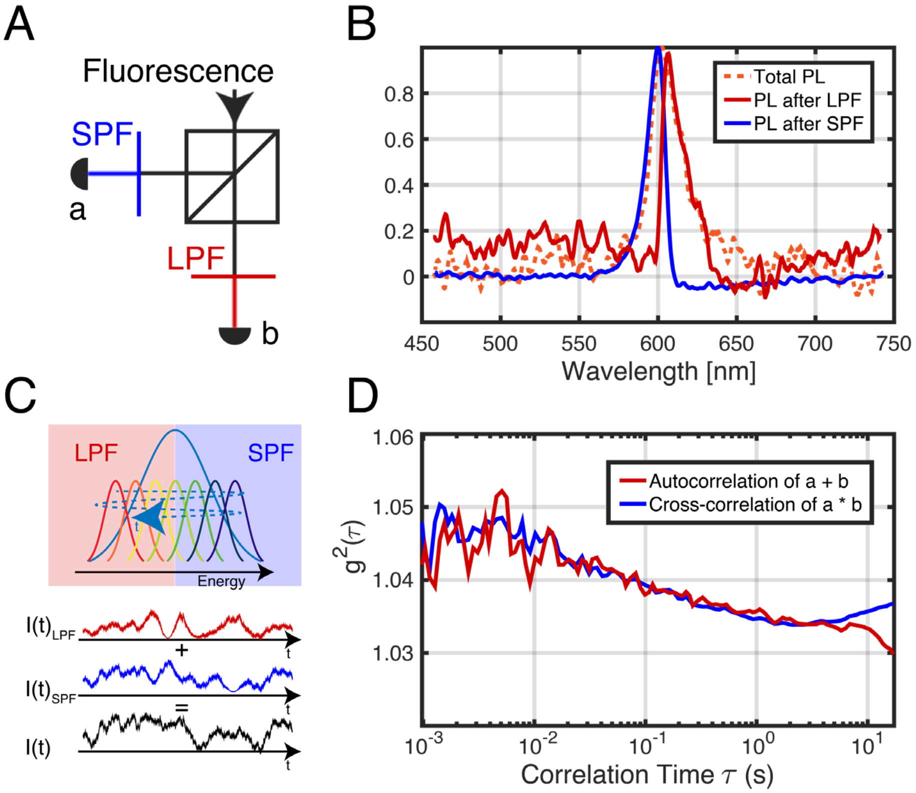

Figure 3. (**A**) Schematic for spectrally biased correlation measurements. Incoming PL is split by a 50/50 beam splitter; a long-pass filter (LPF) and a short pass filter (SPF) are placed in front of the respective detectors. (**B**) PL spectra of the core/shell NPL before and after introduction of the LPF and SPF. (**C**) Example time traces obtained using this ratiometric method in the presence of SD, which results in deviation of the signal from LPF and SPF detectors from each other and from the total intensity. (**D**) Spectrally biased correlation for a 4ML/1ML core/shell NPL. The cross-correlation (blue) and autocorrelation (red) traces overlay until ~5 s.

correlation is identical to the autocorrelation. When SD shifts the center wavelength of emission to higher and lower energies, the ratio of light hitting the two detectors changes in time, **Figure 3C**. The timescale of SD can thus be extracted from when the cross-correlation between the two detectors begins to deviate from the autocorrelation. **Figure 3D** shows that these two plots are identical until ~3 s, when the cross-correlation begins to decrease relative to the autocorrelation. The result that SD only becomes apparent on a >1 s timescale for core/shell NPLs is consistent with the spectral correlation obtained from the spectrograph (**Figure 2**), but additionally shows that SD does *not* occur between 1 ms and 3 s.

Our experiment spectrally biasing detectors, presented in **Figure 3**, shows that the core/shell NPL only experiences SD at >1 s timescale and the time resolution is limited only by the signal-to-noise ratio of the correlation traces and after-pulsing of the APDs. The technique is however restricted by the need for suitable spectral filters. An alternative, more flexible technique for measuring SD is interferometry. Specifically, we use a powerful technique called Photon Correlation Fourier Spectroscopy (PCFS), which utilizes the cross-correlation between detectors at the output of a dithered Michaelson interferometer to extract the average linewidth of two photons separated by a time difference τ. Introduced over a decade ago, PCFS has been applied to study the evolution of PL linewidths of spherical QDs as a function of τ, in order to determine both the homogeneous linewidths hidden behind SD and the timescale of SD. **Figure 4A** shows a schematic diagram of the Michelson interferometer we use in PCFS along with the form of the data extracted from this experiment. If the emitted photons are directed into the interferometer and the intensity of the output as a function of relative path length δ is recorded, a spectral interferogram is generated. The Fourier transform of that interferogram is the familiar emission spectrum. The PCFS experiment instead records the second order correlation $g^{(2)}(\tau,\delta)$ between the two detectors as a function of a very gradually changing relative pathlength, δ.

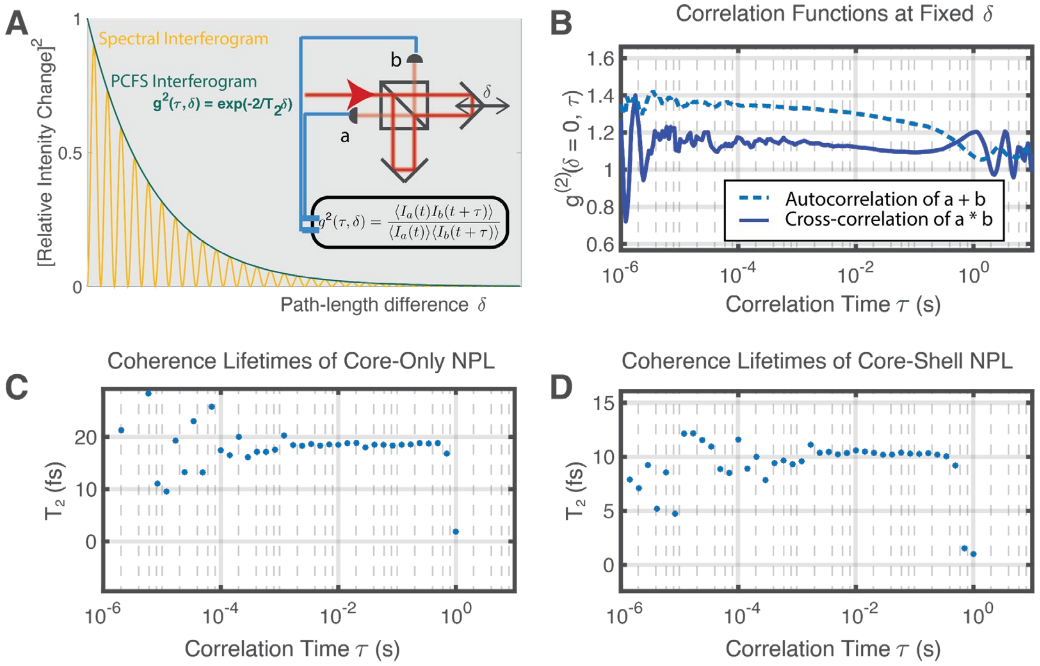

Figure 4. (**A**) Schematic diagram of PCFS. Spectral information is encoded using a Michaelson interferometer and information about fast timescales is extracted using correlations. PCFS retrieves the envelope function of spectral interferograms for photons separated by a time delay of τ. (**B**) Cross-correlation (solid line) and autocorrelation (dotted line) of detectors a and b at $\delta = 0$. The dither waveform that appears starting at roughly 10^{-1} s is an artifact. (**C,D)** The extracted coherence lifetime T_2 as a function of photon separation τ for (**C**) 5ML NPL and (**D**) 4 ML core/shell NPL. The decrease T_2 starting at 10^{-1} s is an artifact from the dithering.

Figure 4B shows the autocorrelation function for the sum of the signals at detectors a and b and the cross-correlation between the signals at detectors for one core/shell NPL at $\delta = 0$. The autocorrelation reports the intensity fluctuation due to blinking. Here, the value of $g^{(2)}$ begins to drop at ~100 μs; this loss of correlation with increasing τ indicates that blinking dynamics are occurring on that timescale.[21-22] This result, in conjunction with the spectrograph data in **Figure 2**, confirms that blinking occurs on numerous timescales, ranging from 100 μs to 10s of s.

The cross-correlation trace in **Figure 4B** reports on the degree of anti-correlation between the two detectors. At timescales of ~1 s, artifacts of the slowly moving stages can be seen, putting an upper limit on the timescale to which PCFS is sensitive. When the interferometer has $\delta \approx 0$, the output of the interferometer at the two detectors is anti-correlated due to interference resulting in a lower cross-correlation value than an autocorrelation value. For $\delta \gg 0$, a lack of interference results in each detector experiencing the same intensity fluctuations, so that the cross-correlation is identical to the autocorrelation (shown in the SI). The degree of anti-correlation of the two detectors as a function of δ yields the envelope function of the spectral interferogram, which is related to the linewidth of the emitter by the coherence time T_2. For a Lorentzian lineshape, the linewidth is given by $\Gamma = 2\hbar/T_2$. **Figures 4C,D** show the coherence time as a function of the correlation lag-time τ for core-only and core/shell NPLs. For emitters that exhibit no SD, T_2 is independent of τ because the time separating two photons does not affect the degree of interference. If instead the photons entering the interferometer at two times have different spectra, the interference decreases and T_2 decreases with τ. **Figures 4C-D** show that neither the 5ML NPLs nor the 4ML core/shell NPLs undergo SD on the 1 μs – 100 ms timescale, as indicated by a constant value of T_2 over that set of correlation times. For the 5ML NPLs, the value of T_2 consistently hovers at 19 fs, while for the 4ML/1ML core/shell NPL T_2 is 10 fs. These coherence lifetimes correspond to Lorentzian linewidths of 69.3 and 131 meV respectively, broader than measured in the spectrometer. Linewidths are inversely proportional to coherence lifetimes, so the error in the absolute value of broad linewidths is expected to be large for short coherence lifetimes. Such uncertainty in the absolute value of the linewidth does not however translate into uncertainty in the timescale of SD.

A.4 Conclusion

Using the three techniques described above, we determine that, between 1 μs and several hundred ms, blinking occurs in the absence of SD. Only at the ~1 s timescale and longer is SD observed, and it is correlated to blinking. This result indicates that two types of blinking are occurring in these NPLs. The faster-time-scale blinking that is uncorrelated with SD is likely due to non-radiative recombination of trapped excitons. Each cycle of excitation and emission has similar emissive properties, even if there are momentary lapses in emission intensity. The timescale over which this mechanism is operative implies that transient passivation of traps by, for instance, dynamic exchange of ligands on and off the NPL surface, may occur on a ~100 μs timescale. The correlation of slower blinking dynamics with SD indicates that blinking on this timescale is due to switching between different emissive states, such as excitons and trions, and that this transition occurs on the seconds timescale (and slower). Blinking due to *mechanism 2* on the ~1 s timescale indicates that certain trapped excitons can persist for long periods of time. While some of the trapped excitons quickly return to the ground state via a *mechanism 1* type non-radiative recombination, other trapped excitons can persist for seconds, leading to the formation of trions. The typical non-radiative recombination route is inaccessible for these long-lived states, and we speculate that they require unlikely detrapping events to return to a neutral exciton before returning to the ground state. This conclusion is consistent with the observation that low-temperature emission spectra of NPLs is dominated by trion emission. With a better understanding of the dynamics of trapping that cause slow SD dynamics, controlling these mechanisms may allow for better control of photon indistinguishability for NPL single photon emitters.

Reference for Appendix A

(1) Michler, P.; Imamoğlu, A.; Mason, M. D.; Carson, P. J.; Strouse, G. F.; Buratto, S. K., Quantum Correlation among Photons from a Single Quantum Dot at Room Temperature. *Nature* **2000,** *406* (6799), 968-970.

(2) Neuhauser, R. G.; Shimizu, K. T.; Woo, W. K.; Empedocles, S. A.; Bawendi, M. G., Correlation between Fluorescence Intermittency and Spectral Diffusion in Single Semiconductor Quantum Dots. *Physical Review Letters* **2000,** *85* (15), 3301-3304.

(3) Zhao, J.; Nair, G.; Fisher, B. R.; Bawendi, M. G., Challenge to the Charging Model of Semiconductor-Nanocrystal Fluorescence Intermittency from Off-State Quantum Yields and Multiexciton Blinking. *Physical Review Letters* **2010,** *104* (15), 157403.

(4) Galland, C.; Ghosh, Y.; Steinbrück, A.; Sykora, M.; Hollingsworth, J. A.; Klimov, V. I.; Htoon, H., Two Types of Luminescence Blinking Revealed by Spectroelectrochemistry of Single Quantum Dots. *Nature* **2011,** *479* (7372), 203-207.

(5) Kuno, M.; Fromm, D. P.; Hamann, H. F.; Gallagher, A.; Nesbitt, D. J., Nonexponential "blinking" Kinetics of Single CdSe Quantum Dots: A Universal Power Law Behavior. *J. Chem. Phys.* **2000,** *112* (7), 3117-3120.

(6) Ihara, T.; Kanemitsu, Y., Spectral Diffusion of Neutral and Charged Exciton Transitions in Single CdSe/ZnS Nanocrystals due to Quantum-confined Stark Effect. *Phys. Rev. B* **2014,** *90* (19), 195302.

(7) Gomez, D. E.; van Embden, J.; Mulvaney, P., Spectral Diffusion of Single Semiconductor Nanocrystals: The Influence of the Dielectric Environment. *Appl. Phys. Lett.* **2006,** *88* (15), 3.

(8) Empedocles, S. A.; Norris, D. J.; Bawendi, M. G., Photoluminescence Spectroscopy of Single CdSe Nanocrystallite Quantum Dots. *Physical Review Letters* **1996,** *77* (18), 3873-3876.

(9) Empedocles, S. A.; Bawendi, M. G., Influence of Spectral Diffusion on the Line Shapes of Single CdSe Nanocrystallite Quantum Dots. *The Journal of Physical Chemistry B* **1999,** *103* (11), 1826-1830.

(10) Wolters, J.; Sadzak, N.; Schell, A. W.; Schröder, T.; Benson, O., Measurement of the Ultrafast Spectral Diffusion of the Optical Transition of Nitrogen Vacancy Centers in Nano-Size Diamond Using Correlation Interferometry. *Physical Review Letters* **2013,** *110* (2), 027401.

(11) Santori, C.; Fattal, D.; Vučković, J.; Solomon, G. S.; Yamamoto, Y., Indistinguishable Photons from a Single-Photon Device. *Nature* **2002,** *419* (6907), 594-597.

(12) Brokmann, X.; Bawendi, M.; Coolen, L.; Hermier, J.-P., Photon-Correlation Fourier Spectroscopy. *Opt. Express* **2006,** *14* (13), 6333-6341.

(13) Coolen, L.; Brokmann, X.; Spinicelli, P.; Hermier, J. P., Emission Characterization of a Single CdSe-ZnS Nanocrystal with High Temporal and Spectral Resolution by Photon-Correlation Fourier Spectroscopy. *Physical Review Letters* **2008,** *100* (2), 027403.

(14) Beyler, A. P.; Marshall, L. F.; Cui, J.; Brokmann, X.; Bawendi, M. G., Direct Observation of Rapid Discrete Spectral Dynamics in Single Colloidal CdSe-CdS Core-Shell Quantum Dots. *Physical Review Letters* **2013,** *111* (17), 177401.

(15) Utzat, H.; Sun, W.; Kaplan, A. E. K.; Krieg, F.; Ginterseder, M.; Spokoyny, B.; Klein, N. D.; Shulenberger, K. E.; Perkinson, C. F.; Kovalenko, M. V.; Bawendi, M. G., Coherent Single-Photon Emission from Colloidal Lead Halide Perovskite Quantum Dots. *Science* **2019,** *363* (6431), 1068-1072.

(16) Spokoyny, B.; Utzat, H.; Moon, H.; Grosso, G.; Englund, D.; Bawendi, M. G., Effect of Spectral Diffusion on the Coherence Properties of a Single Quantum Emitter in Hexagonal Boron Nitride. *The Journal of Physical Chemistry Letters* **2020,** *11* (4), 1330-1335.

(17) Ithurria, S.; Talapin, D. V., Colloidal Atomic Layer Deposition (c-ALD) using Self-Limiting Reactions at Nanocrystal Surface Coupled to Phase Transfer between Polar and Nonpolar Media. *Journal of the American Chemical Society* **2012,** *134* (45), 18585-18590.

(18) Tessier, M. D.; Mahler, B.; Nadal, B.; Heuclin, H.; Pedetti, S.; Dubertret, B., Spectroscopy of Colloidal Semiconductor Core/Shell Nanoplatelets with High Quantum Yield. *Nano Letters* **2013,** *13* (7), 3321-3328.

(19) Ma, X.; Diroll, B. T.; Cho, W.; Fedin, I.; Schaller, R. D.; Talapin, D. V.; Gray, S. K.; Wiederrecht, G. P.; Gosztola, D. J., Size-Dependent Biexciton Quantum Yields and Carrier Dynamics of Quasi-Two-Dimensional Core/Shell Nanoplatelets. *ACS Nano* **2017,** *11* (9), 9119-9127.

(20) Sallen, G.; Tribu, A.; Aichele, T.; André, R.; Besombes, L.; Bougerol, C.; Richard, M.; Tatarenko, S.; Kheng, K.; Poizat, J. P., Subnanosecond Spectral Diffusion Measurement Using Photon Correlation. *Nat. Photonics* **2010,** *4* (10), 696-699.

(21) Messin, G.; Hermier, J. P.; Giacobino, E.; Desbiolles, P.; Dahan, M., Bunching and Antibunching in the Fluorescence of Semiconductor Nanocrystals. *Opt. Lett.* **2001,** *26* (23), 1891-1893.

(22) Rabouw, F. T.; Antolinez, F. V.; Brechbühler, R.; Norris, D. J., Microsecond Blinking Events in the Fluorescence of Colloidal Quantum Dots Revealed by Correlation Analysis on Preselected Photons. *The Journal of Physical Chemistry Letters* **2019,** *10* (13), 3732-3738.

Appendix B: Electronic Structure Calculations of Various Metal-Molecule Complexes

B.1 Excited state calculations for molecule-Au_{20} with different electron affinity

Plasmon-driven chemistry has attracted lots of research interest which utilizes hot carriers generated from plasmon decay process to trigger chemical reactions at the interface. Here the researchers studied the plasmon-driven anion radical formation for five polypyridyl complexes (22BPY, 44BPY, BPE, BPA, and BPEt) of varying degrees of electron affinity on gold nanoparticles by two-color SERS experiments.

Electronic structure calculations for molecules (22BPY, 44BPY, BPE, BPA, and BPEt) interacting with a Au_{20} cluster were performed with TDDFT using the exchange-correlation functional BP86 within the Amsterdam Density Functional (ADF) program.[1] The basis set TZP

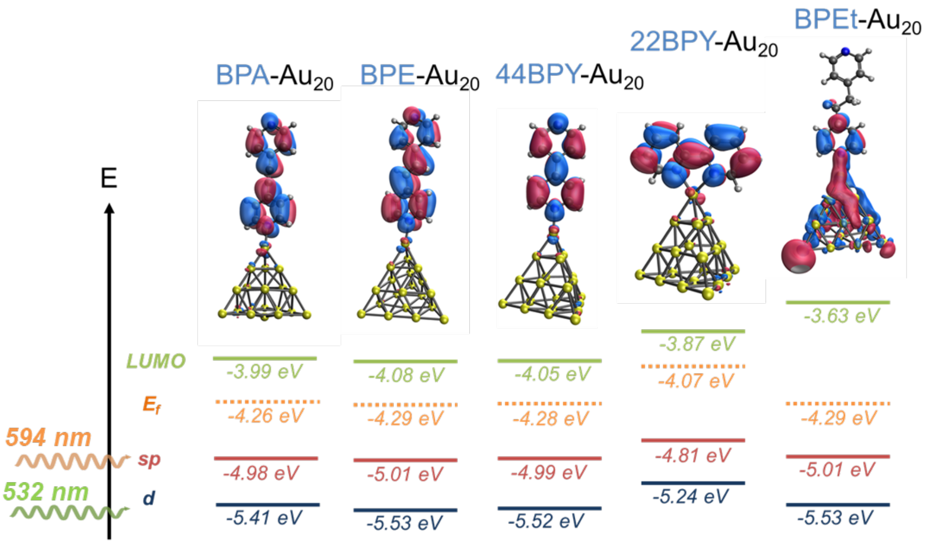

Figure 1. TDDFT calculated energy levels for the five different reporter molecules bound to an Au_{20} cluster where a 594 nm pump excites sp-band gold electrons, and a 532 nm pump excites d-band gold electrons. Energy levels are labeled as: d – highest occupied d orbitals in gold, sp – highest occupied sp orbitals in gold, E_f – Fermi level of molecule-gold cluster, LUMO – lowest unoccupied molecular orbital. The binding configuration and LUMO orbital is depicted above the energy levels. Note that in some cases, the LUMO orbital is LUMO+1 or LUMO+2, but is selected to represent the lowest unoccupied orbital of having mostly adsorbate character.

was employed for all the atoms. We used the zero-order regular approximation to include the relativistic effect for the calculations. For the ground-state geometry optimization, the energy difference tolerance is set to be 10^{-5} Hartree and nuclear gradient tolerance 10^{-4} Hartree/Å. In the excited state calculations, we calculated the lowest 20 allowed excitation transitions. We also did the similar calculations for Au_{20} structure and the molecules individually for comparison. We use the Kohn-Sham orbital energies to define HOMO and LUMO positions, with the electron affinity defined in terms of the energy of the LUMO relative to the vacuum level (Koopmans' theorem). By comparing the excited state energy level of the five polypyridyl complexes-Au_{20} systems and experimental SERS data, it demonstrates that the reactivity of plasmon-driven anion formation is related to not only the electron affinity, but also the orbital overlap, the laser excitation wavelength. This collaboration work is published in JPCC: Sprague-Klein, E. A.; Ho-Wu, R.; Nguyen, D.; Coste, S. C.; **Wu, Y.**; McMahon, J. J.; Seideman, T.; Schatz, G. C.; Van Duyne, R. P., Modulating the Electron Affinity of Small Bipyridyl Molecules on Single Gold Nanoparticles for Plasmon-Driven Electron Transfer. *The Journal of Physical Chemistry C* **2021,** *125* (40), 22142-22153.

B.2 Static Raman calculation of phenanthroline on copper surface

Experimental collaborators found that 1,10-phenantholine adsorbed on copper surface can serve as a good co-catalyst system for CO_2 reduction. In the sample characterization they found strong Raman peak intensity increase in around 1500 cm^{-1} region.

To test the assumptions: Is the Raman peak intensity increase related to 1) 1,10-phenantholine bind to copper surface? 2) 1,10-phenantholine dimerization on the copper surface? Static Raman calculations were performed with the Amsterdam Density Functional (ADF) computational chemistry package. Full geometry optimization, vibrational modes and Raman intensity calculations used Becke-Perdew (BP86) generalized gradient approximation (GGA) exchange correlation functional and a triple-ζ polarized (TZP) Slater orbital basis set with zeroth order regular approximation (ZORA).

The calculated Raman cross section is expressed as:[2]

$$\frac{d\sigma}{d\Omega} = \frac{h}{8\epsilon_0^2 c\tilde{\upsilon}_p}\left(\tilde{\upsilon}_{in} - \tilde{\upsilon}_p\right)^4\left(45\bar{\alpha}_p'^2 + 7\bar{\gamma}_p'^2\right)\frac{1}{45\left[1 - \exp\left(-hc\tilde{\upsilon}_p/k_B T\right]\right.}$$

The calculated Raman spectra are shown in **Figure 2**. It proved that the adsorption of phenanthroline monomer on the vertex atom of Cu surface, rather than the dimerization process is the main mechanism of the Raman intensity increase in 1500 cm^{-1} region.

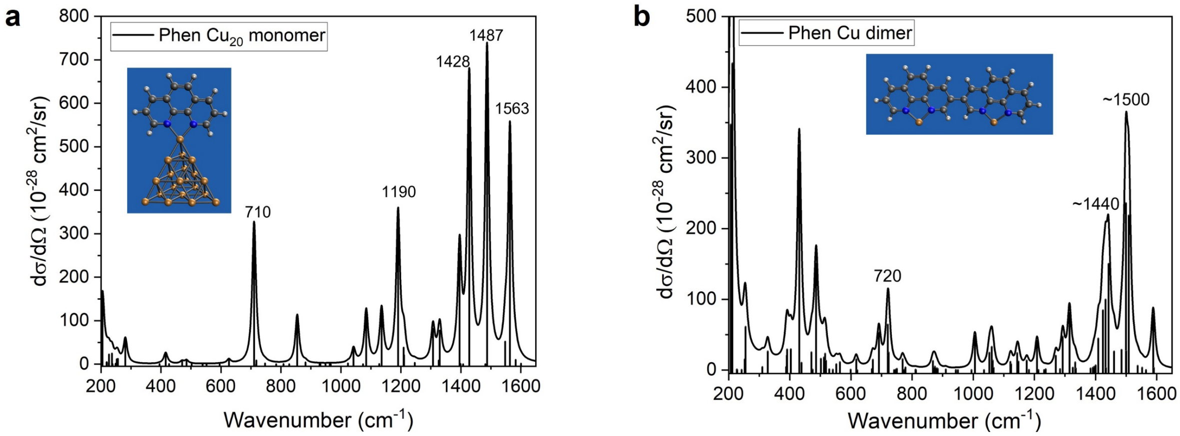

Figure 2. The simulated Raman spectra of Phenanthroline monomer on Cu$_{20}$ cluster (**a**) and Phenanthroline dimer (**b**).

Reference for Appendix B

(1) Te Velde, G.; Bickelhaupt, F. M.; Baerends, E. J.; Guerra, C. F.; Van Gisbergen, S. J. A.; Snijders, J. G.; Ziegler, T., Chemistry with ADF. *J. Comput. Chem.* **2001,** *22* (9), 931-967.

(2) Neugebauer, J.; Reiher, M.; Kind, C.; Hess, B. A., Quantum Chemical Calculation of Vibrational Spectra of Large Molecules—Raman and IR Spectra for Buckminsterfullerene. *J. Comput. Chem.* **2002,** *23* (9), 895-910.

Appendix C: Original Research Proposal

Mechanism Study of Electrochemical CO_2 Reduction with Transition Metal Complexes as Catalyst in Single-Molecule Junction

Abstract

This proposal describes the project of investigating the detailed reaction mechanisms of CO_2 electrochemical reduction catalyzed by transition metal complexes via integrating the catalyst molecule into the single-molecule junction fabricated in the nanocircuit device and monitoring the reaction by real-time electric measurements. This technique based on single-molecule junction enables us to study the reaction pathway on single molecule level and have faster response (μs) compared to the conventional ensemble cyclic voltammetry measurements. Here we choose an electrocatalyst, $Re(bpy)(CO)_3Cl$, as the model catalytical center in the single-molecule junction, and the current time traces I(t) are recorded when CO_2 reduction is triggered on the device. The statistical histograms under different bias voltage reveal different conductance states occurred in the reaction process. Combined with theoretical calculations, the corresponding transition states or reaction intermediates can be examined for specific reaction pathways. The reaction rate and pathway dependence on the catalyst molecule design and local environment (solvent, temperature, etc.) can also be studied on the same single-molecule device. This proposal focuses on applying the novel single-molecule electric detection techniques in the fundamental mechanism study in CO_2 reduction for better design of the molecular catalysts.

C.1 Introduction, Background and Significance of Research

The electrochemical reduction of CO_2 into carbon-based fuels and chemicals offers an efficient and promising approach to utilize renewable energy sources to recycle the released CO_2 from fossil fuels and thus reduce carbon footprint. However, CO_2 is chemically inert with an initial C=O bond energy of 806 $kJ \cdot mol^{-1}$, and requires high overpotential for the direct one-electron reduction of CO_2 to $CO_2^{-\bullet}$ (-1.90 V vs NHE) due to the large reorganization energy from linear molecule to bent radical anion.[1] At the same time, CO_2 can go through multiple steps of reduction, which could lead to a complicated mixture of products including carbon monoxide (CO), formic acid (HCCOH), formaldehyde (CH_2O), methanol (CH_3OH), methane (CH_4), etc.[2-3] So it is essential to design appropriate electrocatalysts to decrease the energy barrier and increase the reaction selectivity of CO_2 electrochemical reduction.

Over a series of decades, enormous research efforts have been paid to the development and optimization of different kinds of electrocatalysts for CO_2 reduction, which can be divided into two categories: heterogeneous and homogeneous electrocatalysts. The heterogeneous catalysts include transition metal surface (Cu, Au, Ag, Pd, etc.), transition metal oxides/chalcogenides (TiO_2, FeO_x, ZnS, MoS_2, etc.) and metal organic frameworks.[4-13] Compared to the heterogeneous catalysts, the homogeneous catalysts are mainly transition metal complexes, serving as a redox shuttle between the electrode and CO_2. They first reached a more highly reduced state by accepting electrons from the electrode and then donate the electrons to CO_2 in the solution.[3, 14-18] The chemical properties homogeneous electrocatalysts can be precisely controlled by changing the metal center or ligands. They also have well-defined coordination geometries and active sites, which makes them especially suitable to analyze the detailed reaction pathways of CO_2

electrochemical reduction and achieve selective products. However, most of the proposed mechanisms of CO_2 electrocatalytic reduction were examined by either theoretical calculations or conventional electrochemical measurements in ensemble.[19-20] Lots of the fundamental reaction steps for various electrocatalysts are still unclear.

Single-molecule detection is a rapidly developing research field which focus on ultrasensitive detection of the detailed dynamic process of various chemical interactions on single molecule/single event level. Some single-molecule analytical techniques have been successfully developed including fluorescence, surface-enhanced Raman spectroscopy (SERS) and scanning tunnelling microscopy (STM).[21-23] In recent years, a new strategy of single-molecule electric detection employing molecular junction nanostructures has been explored in the application of electronic nanodevices, biological detection and dynamics of chemical reactions.[24-26] Among single-molecule junction nanostructures, graphene-molecule-graphene junction is an especially promising candidate to be utilized in mechanistic investigation of chemical reactions because graphene, as a two-dimensional carbon nanomaterial, not only is naturally compatible with large majority of molecules and solvents, but also can be easily fabricated as electrodes with lithography methods. By monitoring the real-time electric signal traces inside the junction after the reaction is triggered, rich chemical information regarding short-lifetime intermediates, kinetic and thermodynamic parameters of elementary reaction steps can be revealed.

Here we propose to use graphene-molecule-graphene junction nanostructure to investigate the detailed mechanism of CO_2 electrocatalytic reduction reactions. It will be the first time that CO_2 reduction reaction with homogeneous catalyst is studied on single-catalyst level. It can not only guide the molecular design of CO_2 reduction catalyst, but also broaden the scope of the chemical reactions the single-molecule electric detection technique can investigate.

C.2 Scientific Objectives

The general scientific objective of this proposal is to examine the proposed mechanisms about the elementary reaction steps of multi-electron CO_2 electrochemical reduction with transition metal complexes as electrocatalyst.

Specific Aim 1: To observe the intermediate species in Re(bpy)$(CO)_3$Cl catalyzed CO_2-to-CO two-electron reduction and distinguish between “protonation first” and “reduction first” mechanisms

Specific Aim 2: To investigate the rate control of each elementary reaction steps in Re(bpy)$(CO)_3$Cl catalyzed CO_2-to-CO two-electron reduction through functional group engineering on Re(bpy)$(CO)_3$Cl or local environment adjustment (strength of electric field, solvent, temperature, concentration of CO_2, etc.)

C.3 Previous Work

Electric-Field Catalyzed Diels-Alder Reaction Dynamics.

Researchers utilized the graphene-molecule-graphene single-molecule junction (GMG-SMJ) structure to study the real-time dynamics of Diels-Alder reaction on an in-situ label-free electrical detection platform.[27]

Figure 1A shows the schematic illustration of the structure of single-molecule junction. The graphene nanosheet was patterned on silica wafer to be fabricated as electrodes for the device. By organic synthesis, maleimide, one of the reactants in Diels-Alder reactions, was functionalized on a molecular bridge and connected to the edge of the two patterned graphene electrodes. **Figure 1C** shows a typical measurement on one single-molecule junction, including real-time current and fluorescence data.

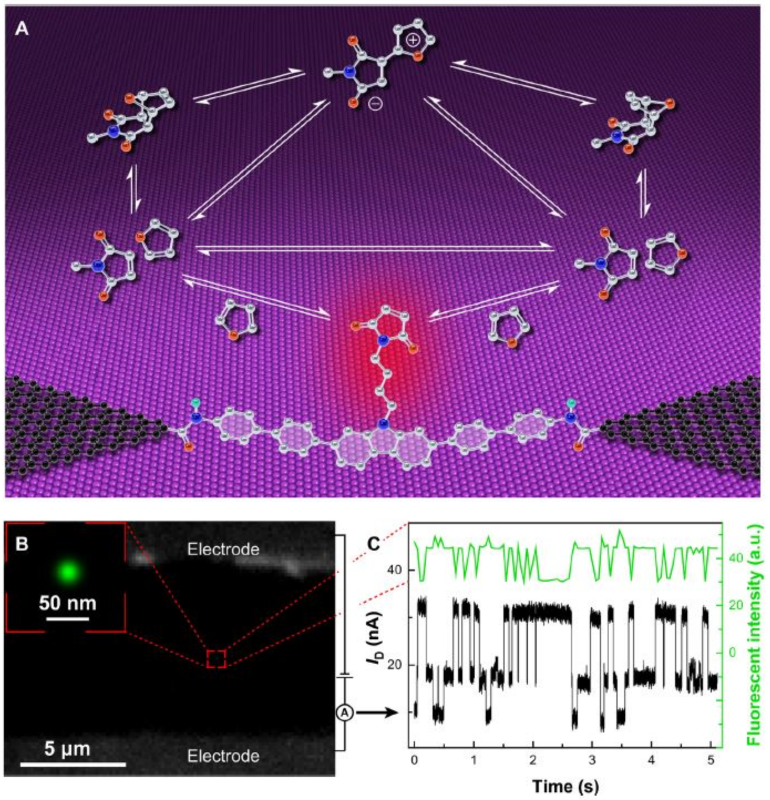

Figure 1. (**A**) The scheme of single-molecule electric monitoring platform with maleimide functional center in the middle of the single-molecule junction. (**B**) Demonstration of single molecule connection. During the interaction of maleimide functional center in the device with fluorescein-substituted furan, 5000 photos were taken by a super-resolution fluorescence microscopy with 50-ms exposure time. (**C**) Synchronized monitoring of current and fluorescence signals in 5-s total acquisition time for the single-molecule junction device. Adapted from Ref (27).

Since the conductance of maleimide in the junction is strongly correlated with the molecular structure during its reaction with furan, the recorded current time trace *I*(t) monitors the structure change of maleimide during the reaction process in real time. In this case, the device was placed in a closed chamber with precise temperature control and nitrogen flow, and the reaction was triggered by furan in the gas phase.

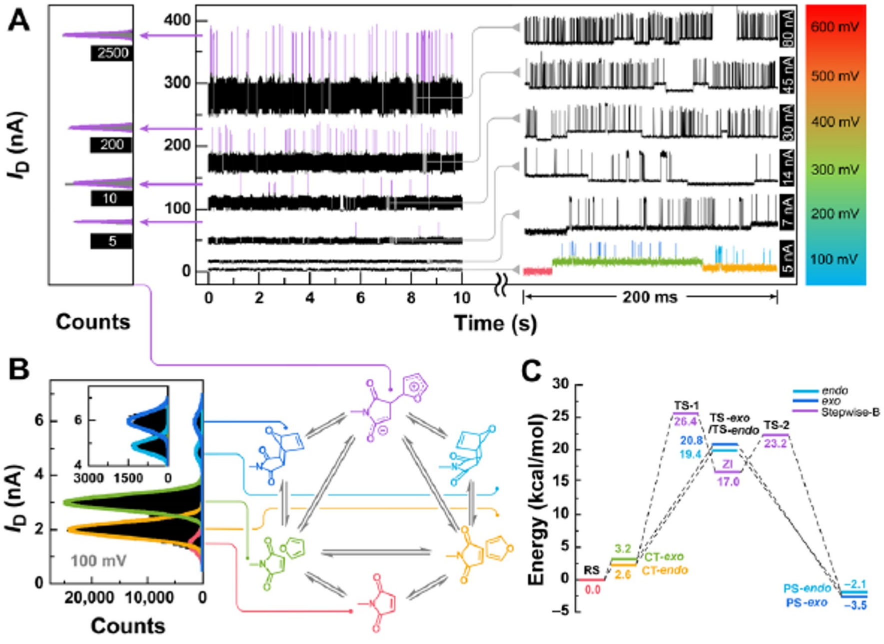

Figure 2. (**A**) Bias voltage dependent current time traces from 100 mV to 600 mV at room temperature. On the left side is the occurrence histogram of the highest conductivity state under 300 – 600 mV (the state is represented by the violet species in (**B**). (**B**) The occurrence histogram and the corresponding reaction mechanism under 100 mV containing six conductance states. (**C**) Gibbs free energies for the concerted and stepwise pathways at -2.57 V/nm. Adapted from Ref (27).

Different current time traces *I*(t) were recorded when applying various constant bias voltages. The current time traces reveal six conductance states (**Figure 2B**) corresponding to six different structures during the Diels-Alder reaction. The highest conductance state is attributed to zwitterionic intermediate (ZI) due to its strong dependence on bias voltage. Combined with theoretical calculations, two reaction pathways were observed and analyzed for the Diels-Alder reaction: the concerted pathway through the charge transfer complexes and the stepwise pathway via a zwitterionic intermediate. They also found the two reaction pathways can be tuned by the strength of applied electric field. Besides the control on external electric field, other local environment factors, like solvent polarities and temperature, can be adjusted and examine their effect on reaction mechanisms and get kinetic or thermodynamic parameters.

Researchers have also applied similar GMG-SMJ structures to study other chemical interactions, like the reaction path of Suzuki-Miyaura cross coupling reaction[28], benzoin reaction[29], nucleophilic substitution[30], etc.

C.4 Proposed Research

C.4.1 Fabrication of Single-Molecule Junction with Re(bpy)(CO)$_3$Cl Functional Center

The first step is to fabricate the electric nanodevice of graphene-molecule-graphene single-molecule junction. The electrocatalyst for CO_2 reduction we propose to study is Re(bpy)(CO)$_3$Cl, a classical homogeneous catalyst converting CO_2 to CO (**Figure 3**).[31-32] The CVD-grown graphene nanosheet was first transferred on silica wafer with PMMA. By electron beam lithography and

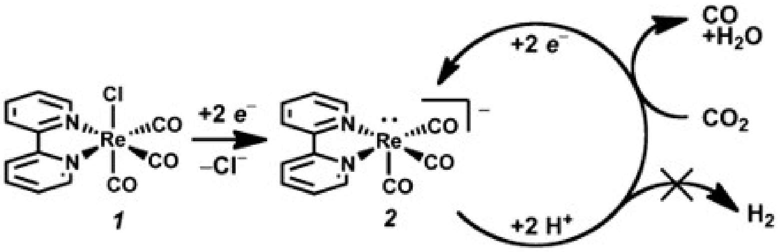

Figure 3. The total reaction of two-electron CO_2 reduction with Re(bpy)(CO)$_3$Cl as the electrocatalyst.

thermal evaporation of gold, arrays of graphene field-effect transistors were fabricated as the electric measurement platform.

To covalently connect Re(bpy)$(CO)_3$Cl with the graphene electrodes, a molecular bridge containing Re(bpy)$(CO)_3$Cl as the functional center with azido-functionalized side arms is synthesized with organic synthesis method. Figure 4A shows the typical synthesis route (using NHC-Pd in Ref (28) as an example) containing three steps. It needs to be noted that the bridge

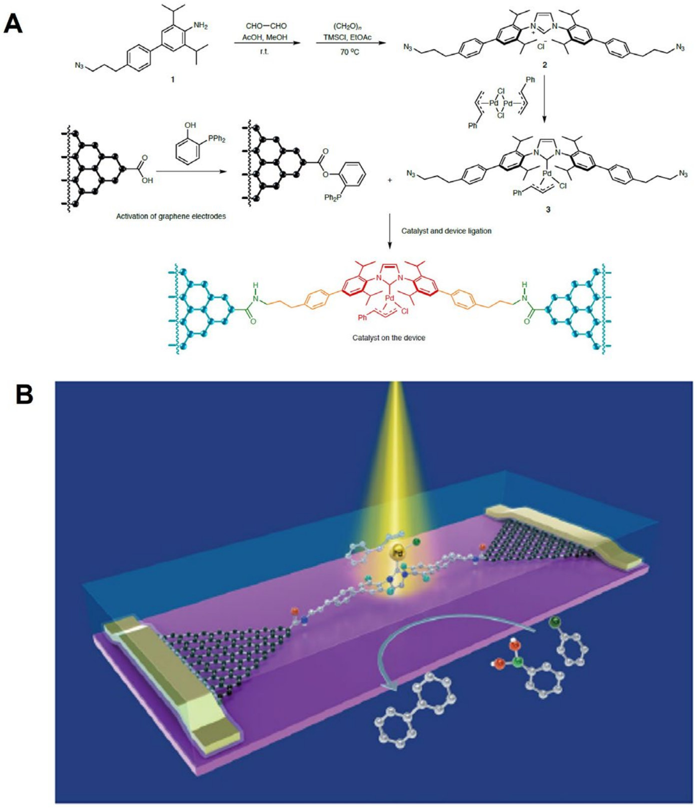

Figure 4. (**A**) The synthesis route of molecular bridge (compound 2) and the connection to oxidized graphene sheet. (**B**) The scheme of the nanocircuit with single-molecule junction for electric measurements. Adapted from Ref (28).

molecule (compound 2) was connected to the target molecule through Pd-ligand bond. However, for Re(bpy)$(CO)_3$Cl the coordination number of center metal Re is already six, so the synthesis strategy might need to be changed that the bridge molecules are connected to the bipyridine ligand instead.

To test whether the Re(bpy)(CO)$_3$Cl-based bridge molecules is successfully attached to the oxidized end of graphene nano-electrode, comparison of current-voltage curves before (no response) and after (some response) needs to be monitored on each nanocircuit device for the following real-time electric measurements.

C.4.2 Specific Aim 1: Direct Observation of Intermediates to Determine the Mechanism

CO$_2$ electrochemical reduction is a multi-electron reaction with different kinds of catalysts involved in the reaction pathways. People have proposed various mechanisms for each reaction step and the classical cyclic voltammetry experiments couldn't determine the actual mechanism in

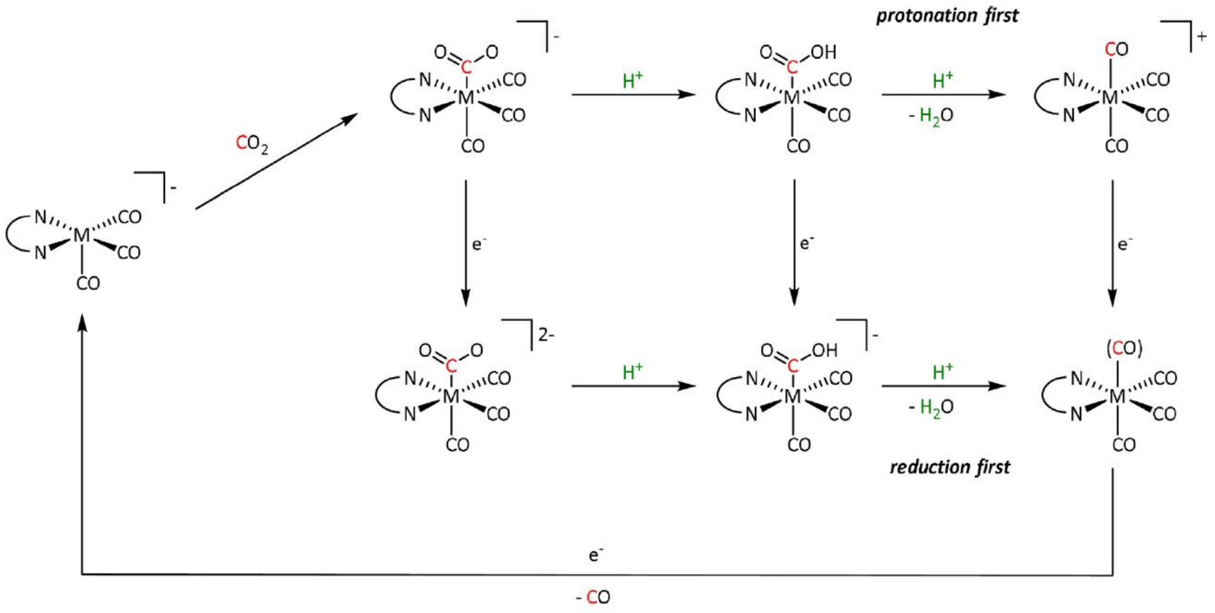

Figure 5. The proposed two mechanisms of Re(bpy)(CO)$_3$Cl catalyzed CO$_2$-to-CO reduction: "protonation first" and "reduction first" mechanisms.

different situations. For example, with Re(bpy)(CO)$_3$Cl as the electrocatalyst, people already understood that it first goes through a two-electron reduction itself to form [Re(bpy)(CO)$_3$]$^-$ anion and have CO_2 attached to the vacant coordination position. But then whether the intermediate first gets protonated or reduced first is still under debate, shown as the "protonation first" and "reduction first" mechanisms in **Figure 5**.

After the single-molecule device is fabricated, the device is connected to a microflow system of electrolyte and CO_2. The real-time current time traces *I*(t) under various bias voltages are recorded. Statistical histograms for each plateau in the *I*(t) reveal the different conductance states appearing during the reaction. Comparing the conductance states and the reaction intermediates proposed in **Figure 5**, we can determine which mechanism is dominant for Re(bpy)(CO)$_3$Cl catalyzed CO_2 electrochemical reduction. Theoretical calculations including time-dependent density functional theory (TDDFT) calculations of the energy diagrams of possible reaction pathways and intermediates can also help to explain the mechanism.

C4.3 Specific Aim 2: Reaction Pathway and Rate Control by Molecular Design or Local Environment Engineering

Besides the bias voltage, the single-molecule device can be used to study lots of other factors controlling the reaction rates and mechanisms, like the molecular design of the catalyst, solvent polarity, temperature, etc. For example, researchers have proposed that the reaction step of releasing CO from the transition metal complex can be favored via a push-pull mechanism. As shown in **Figure 6**, two equivalents of Brønsted acid (HA) can interact with the negatively charged oxygen atom and eventually results in the faster release of H_2O and CO from the transition metal

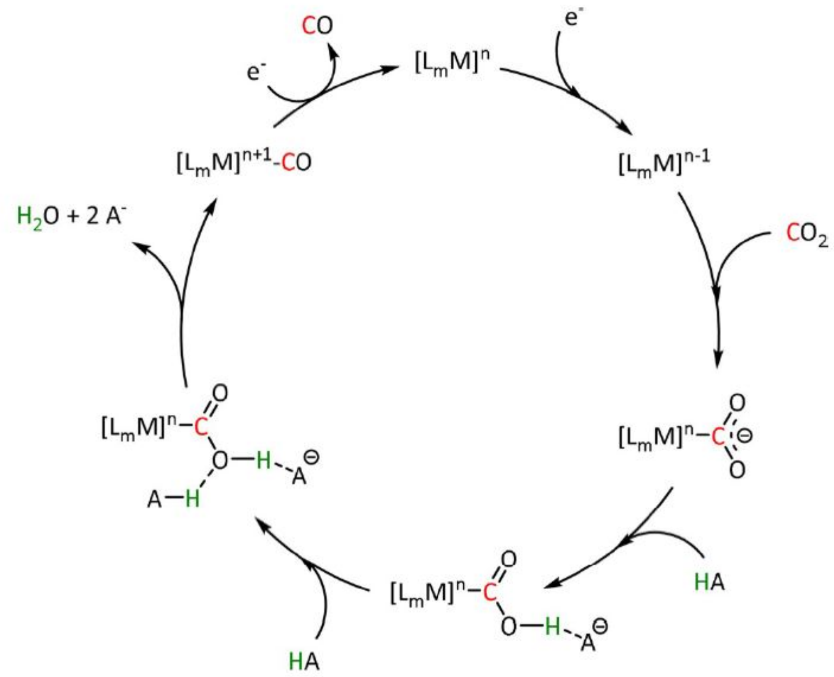

Figure 6. The general push-pull mechanism of the Brønsted acid (HA) assisted reduction of CO_2 to CO.

complex. Different Brønsted acid functional groups can be decorated on the bipyridine ligand and integrated into the single-molecule junction with similar device structure. By recording a series of the current time traces for various Brønsted acid functionalized Re complex, we can not only examine whether the push-pull mechanism works for Re complex catalyst, but also get a quantitative estimation of the enhanced reaction rate. Furthermore, if $Re(bpy)(CO)_3Cl$ works well in the single-molecule junction, other transition metal complexes with different metal center like Fe, Mo, Rh, etc., can also be applied with similar measurement. We can then not only have a better understanding of how to design better homogeneous catalyst for CO_2 electrochemical reduction, but also prove that single-molecule electric detection can be a general strategy to study the reaction mechanisms of similar organometallic reactions under electrochemical conditions.

Temperature control of the single-molecule electric detection can also help to quantitatively get some kinetic and thermodynamic parameters like Gibbs free energies for different steps of reaction.

C4.4 Experimental Challenges and Contingency Plans

Most of the experimental challenges probably are related to the device fabrication. First challenge could be the chemical bonding between the bridge molecule, the Re(bpy)$(CO)_3Cl$ catalysis center. For the example in **Figure 4**, the bridge molecule is directly connected to Pd metal center, while in our case Re(bpy)$(CO)_3Cl$ is already fully coordinated, so the direct connection as a ligand might not be the best choice. Instead, we could apply other organic synthesis strategies to chemically bond the bridge molecule to the bipyridine ligand.

The second challenge is the structural configuration of the Re(bpy)$(CO)_3Cl$ on the surface of the device. In some cases, the Re(bpy)$(CO)_3Cl$ might tend to be close to the silicon wafer surface instead of nearly free in the microfluid of electrolyte and CO_2. To avoid this, a couple of more nano-fabrication steps of patterning nanopillar structures at the position of graphene electrodes can be applied before fabricating the graphene electrodes. With this additional step, the whole device would be hundreds of nm or a few μm above the silica wafer surface and the Re(bpy)$(CO)_3Cl$ reaction center can be freely suspended in the microfluid.

The stability and reproducibility of the single-molecule devices is always an engineering challenge in general. The most practical solution is to fabricate as many nanocircuit devices as possible for one batch and collect all the data in the same batch. Also, the electric probing system can be placed in a chemically inert environment (like a glove box in the clean room) to avoid fluctuations affecting the current signals from the environment.

Summary and Conclusions

To summarize, this proposal outlines the research project of using single-molecule electric detection method to study the CO_2 electrochemical reduction catalyzed by transition metal complexes. This ultrasensitive analytical method enables us to monitor the reaction steps and intermediates in real time, thus gain a deeper understanding of the mechanisms of each step during homogeneously catalyzed CO_2 electrochemical reduction. The systematic study of bias voltage dependence and temperature dependence of the current time traces, combined with theoretical calculations, reveals some key kinetic and thermodynamic parameters like Gibbs free energies for each reaction step. The research projects in this proposal focus on the fundamental mechanism study of chemical reactions and can lead to the better design of the electrocatalyst for CO_2 reduction and other organometallic reactions.

Reference

(1) Benson, E. E.; Kubiak, C. P.; Sathrum, A. J.; Smieja, J. M., Electrocatalytic and Homogeneous Approaches to Conversion of CO_2 to Liquid Fuels. *Chem. Soc. Rev.* **2009,** *38* (1), 89-99.

(2) Zhang, S.; Fan, Q.; Xia, R.; Meyer, T. J., CO_2 Reduction: From Homogeneous to Heterogeneous Electrocatalysis. *Accounts of Chemical Research* **2020,** *53* (1), 255-264.

(3) Kinzel, N. W.; Werlé, C.; Leitner, W., Transition Metal Complexes as Catalysts for the Electroconversion of CO_2: An Organometallic Perspective. *Angewandte Chemie International Edition* **2021,** *60* (21), 11628-11686.

(4) Zhu, D. D.; Liu, J. L.; Qiao, S. Z., Recent Advances in Inorganic Heterogeneous Electrocatalysts for Reduction of Carbon Dioxide. *Advanced Materials* **2016,** *28* (18), 3423-3452.

(5) Hori, Y.; Wakebe, H.; Tsukamoto, T.; Koga, O., Electrocatalytic Process of CO Selectivity in Electrochemical Reduction of CO_2 at Metal Electrodes in Aqueous Media. *Electrochimica Acta* **1994,** *39* (11), 1833-1839.

(6) Hori, Y.; Takahashi, I.; Koga, O.; Hoshi, N., Selective Formation of C2 Compounds from Electrochemical Reduction of CO_2 at a Series of Copper Single Crystal Electrodes. *The Journal of Physical Chemistry B* **2002,** *106* (1), 15-17.

(7) Kim, D.; Resasco, J.; Yu, Y.; Asiri, A. M.; Yang, P., Synergistic Geometric and Electronic Effects for Electrochemical Reduction of Carbon Dioxide Using Gold–Copper Bimetallic Nanoparticles. *Nat. Commun.* **2014,** *5* (1), 4948.

(8) Tayyebi, E.; Hussain, J.; Abghoui, Y.; Skúlason, E., Trends of Electrochemical CO_2 Reduction Reaction on Transition Metal Oxide Catalysts. *The Journal of Physical Chemistry C* **2018,** *122* (18), 10078-10087.

(9) Jiang, K.; Wang, H.; Cai, W.-B.; Wang, H., Li Electrochemical Tuning of Metal Oxide for Highly Selective CO_2 Reduction. *ACS Nano* **2017,** *11* (6), 6451-6458.

(10) Ji, Y.; Nørskov, J. K.; Chan, K., Scaling Relations on Basal Plane Vacancies of Transition Metal Dichalcogenides for CO_2 Reduction. *The Journal of Physical Chemistry C* **2019,** *123* (7), 4256-4261.

(11) Gao, F.-Y.; Wu, Z.-Z.; Gao, M.-R., Electrochemical CO_2 Reduction on Transition-Metal Chalcogenide Catalysts: Recent Advances and Future Perspectives. *Energy & Fuels* **2021,** *35* (16), 12869-12883.

(12) Hod, I.; Sampson, M. D.; Deria, P.; Kubiak, C. P.; Farha, O. K.; Hupp, J. T., Fe-Porphyrin-Based Metal–Organic Framework Films as High-Surface Concentration, Heterogeneous Catalysts for Electrochemical Reduction of CO_2. *ACS Catalysis* **2015,** *5* (11), 6302-6309.

(13) Hinogami, R.; Yotsuhashi, S.; Deguchi, M.; Zenitani, Y.; Hashiba, H.; Yamada, Y., Electrochemical Reduction of Carbon Dioxide Using a Copper Rubeanate Metal Organic Framework. *ECS Electrochemistry Letters* **2012,** *1* (4), H17-H19.

(14) Kang, P.; Cheng, C.; Chen, Z.; Schauer, C. K.; Meyer, T. J.; Brookhart, M., Selective Electrocatalytic Reduction of CO_2 to Formate by Water-Stable Iridium Dihydride Pincer Complexes. *Journal of the American Chemical Society* **2012,** *134* (12), 5500-5503.

(15) Bolinger, C. M.; Story, N.; Sullivan, B. P.; Meyer, T. J., Electrocatalytic Reduction of Carbon Dioxide by 2,2'-bipyridine Complexes of Rhodium and Iridium. *Inorganic Chemistry* **1988,** *27* (25), 4582-4587.

(16) Chen, Z.; Chen, C.; Weinberg, D. R.; Kang, P.; Concepcion, J. J.; Harrison, D. P.; Brookhart, M. S.; Meyer, T. J., Electrocatalytic Reduction of CO_2 to CO by Polypyridyl Ruthenium Complexes. *Chemical Communications* **2011,** *47* (47), 12607-12609.

(17) Oberem, E.; Roesel, A. F.; Rosas-Hernández, A.; Kull, T.; Fischer, S.; Spannenberg, A.; Junge, H.; Beller, M.; Ludwig, R.; Roemelt, M.; Francke, R., Mechanistic Insights into the Electrochemical Reduction of CO_2 Catalyzed by Iron Cyclopentadienone Complexes. *Organometallics* **2019,** *38* (6), 1236-1247.

(18) Collin, J. P.; Jouaiti, A.; Sauvage, J. P., Electrocatalytic Properties of Ni(cyclam)$^{2+}$ and Ni_2(biscyclam)$^{4+}$ with respect to Carbon Dioxide and Water Reduction. *Inorganic Chemistry* **1988,** *27* (11), 1986-1990.

(19) Lu, Q.; Jiao, F., Electrochemical CO_2 Reduction: Electrocatalyst, Reaction Mechanism, and Process Engineering. *Nano Energy* **2016,** *29*, 439-456.

(20) Tian, Z.; Priest, C.; Chen, L., Recent Progress in the Theoretical Investigation of Electrocatalytic Reduction of CO_2. *Advanced Theory and Simulations* **2018,** *1* (5), 1800004.

(21) Kulzer, F.; Orrit, M., Single-Molecule Optics. *Annu. Rev. Phys. Chem.* **2004,** *55* (1), 585-611.

(22) Le Ru, E. C.; Etchegoin, P. G., Single-Molecule Surface-Enhanced Raman Spectroscopy. *Annu. Rev. Phys. Chem.* **2012,** *63*, 65-87.

(23) Ho, W., Single-Molecule Chemistry. *The Journal of chemical physics* **2002,** *117* (24), 11033-11061.

(24) Jia, C.; Migliore, A.; Xin, N.; Huang, S.; Wang, J.; Yang, Q.; Wang, S.; Chen, H.; Wang, D.; Feng, B.; Liu, Z.; Zhang, G.; Qu, D.-H.; Tian, H.; Ratner, M. A.; Xu, H. Q.; Nitzan, A.; Guo, X., Covalently Bonded Single-Molecule Junctions with Stable and Reversible Photoswitched Conductivity. *Science* **2016,** *352* (6292), 1443-1445.

(25) Akkilic, N.; Geschwindner, S.; Höök, F., Single-Molecule Biosensors: Recent Advances and Applications. *Biosensors and Bioelectronics* **2020,** *151*, 111944.

(26) Li, Y.; Yang, C.; Guo, X., Single-Molecule Electrical Detection: A Promising Route toward the Fundamental Limits of Chemistry and Life Science. *Accounts of Chemical Research* **2020,** *53* (1), 159-169.

(27) Yang, C.; Liu, Z.; Li, Y.; Zhou, S.; Lu, C.; Guo, Y.; Ramirez, M.; Zhang, Q.; Li, Y.; Liu, Z.; Houk, K. N.; Zhang, D.; Guo, X., Electric Field-Catalyzed Single-Molecule Diels-Alder Reaction Dynamics. *Science Advances* **2021,** *7* (4), eabf0689.

(28) Yang, C.; Zhang, L.; Lu, C.; Zhou, S.; Li, X.; Li, Y.; Yang, Y.; Li, Y.; Liu, Z.; Yang, J.; Houk, K. N.; Mo, F.; Guo, X., Unveiling the Full Reaction Path of the Suzuki–Miyaura Cross-Coupling in a Single-Molecule Junction. *Nature Nanotechnology* **2021**.

(29) Yang, C.; Zhang, L.; Li, H.; Guo, Y.; Jia, C.; Zhu, W.; Mo, F.; Guo, X., Single-Molecule Electrical Spectroscopy of Organocatalysis. *Matter* **2021,** *4* (9), 2874-2885.

(30) Gu, C.; Hu, C.; Wei, Y.; Lin, D.; Jia, C.; Li, M.; Su, D.; Guan, J.; Xia, A.; Xie, L.; Nitzan, A.; Guo, H.; Guo, X., Label-Free Dynamic Detection of Single-Molecule Nucleophilic-Substitution Reactions. *Nano Letters* **2018,** *18* (7), 4156-4162.

(31) Keith, J. A.; Grice, K. A.; Kubiak, C. P.; Carter, E. A., Elucidation of the Selectivity of Proton-Dependent Electrocatalytic CO_2 Reduction by fac-Re(bpy)$(CO)_3$Cl. *Journal of the American Chemical Society* **2013,** *135* (42), 15823-15829.

(32) Sullivan, B. P.; Bolinger, C. M.; Conrad, D.; Vining, W. J.; Meyer, T. J., One- and Two-Electron Pathways in the Electrocatalytic Reduction of CO_2 by fac-Re(bpy)$(CO)_3$Cl (bpy = 2,2′-bipyridine). *Journal of the Chemical Society, Chemical Communications* **1985,** (20), 1414-1416.